10th DELTA User Meeting

&

Annual Report 2014

Dortmund
26. November 2014

Preface

Dear reader, dear colleague,

this year we were able to prepare the 10th DELTA annual report. It is exciting to see how dynamic the scientific community at DELTA has grown, in terms of actively participating user groups and involved scientists as well as in the diversity of the conducted research projects. The total number of contributions to the annual report has increased from about 20 in the first years to almost 50 in 2014. Consequently, a growing number of peer-reviewed publications and contributions to conferences strongly enhanced the visibility of the DELTA synchrotron source in the national and international scientific community. This success was only possible due to the continuous development of the DELTA machine with new beamlines and improved instrumentation, the engagement and support of external user groups, and the DELTA staff members that took care for the delivery of intense and stable beams.

Education at DELTA is another highlight – today we are able to realize that many former students have found their places both in industry and the scientific community worldwide, based on the knowledge and the skills they picked-up during their time in Dortmund. Their success should be stimulus for our current bachelor, master and PhD students, and we should continue and strengthen these activities to foster the spirit of DELTA.

All the conducted projects would be impossible without the financial support of the diverse funding agencies, the local government, the TU Dortmund and the involved universities – we gratefully acknowledge all these different contributions and encourage our users to participate. We are looking forward to the upcoming beamtime periods, hoping that they will be as productive and successful as during the past year!

Christian Sternemann, Ralph Wagner & Dirk Lützenkirchen-Hecht

Contents:

Hard X-ray spectroscopy

Instrumentation

Status of the DELTA Short-Pulse Facility

H. Rast*, S. Cramm†, S. Döring†, M. Gehlmann†, S. Hilbrich*, M. Höner*, H. Huck*, M. Huck*,
S. Khan*, C. Mai*, A. Meyer auf der Heide*, R. Molo*, L. Plucinski†, C.M. Schneider†, P. Ungelenk*

*Center for Synchrotron Radiation (DELTA), TU Dortmund University, Dortmund
†Forschungszentrum Jülich (FZJ) PGI6, Jülich

The DELTA short-pulse facility [1] is based on the Coherent Harmonic Generation (CHG) principle. Pulses from a femtosecond Ti:sapphire laser system or a harmonic thereof interact with an electron bunch in an undulator (modulator) and imprint an energy modulation on the bunch, which is translated to a density modulation (microbunching) by a following magnetic chicane, see Fig. 1. These microbunches radiate coherently in the next undulator (radiator), tuned to a harmonic of the laser wavelength, and create an ultrashort pulse in the VUV regime. Additionally, ultrashort and coherent THz pulses are generated in the subsequent dipole magnets and are transfered to the beamline 5a [2]. In the following, the steps to characterize, optimize and prepare the short-pulse facility for pump-probe experiments are described.
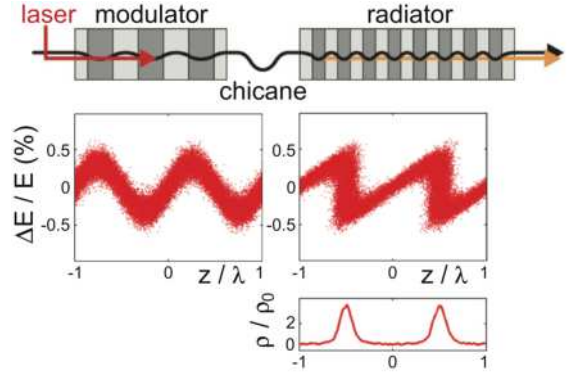
Fig. 1. Setup for the CHG scheme, that translates the energy modulation $\Delta E/E$ imprinted on a bunch to a density modulation ρ/ρ_0 with a magnetic chicane, that has a energy dependent path length.

I. COHERENCE OF THE CHG PULSES

As part of the characterization of the short-pulse facility, studies of the coherence properties of 400-nm and 200-nm CHG pulses were conducted [3] employing interference experiments. The transverse coherence was studied in a double-slit experiment with a variable slit separation in which the coherence degree is described by the visibility of interference fringes. An exemplary measurement with a slit width of 50 μm and a slit separation of 200 μm is shown in Fig. 2 (left), while Fig. 2 (mid) shows the dependence of the visibility on the slit separation. The fringe patterns were detected with a fast-gated iCCD camera[1]. From the results, a coherence length of about 1.5 mm (0.8 mm) for 400-nm (200-nm) radiation could be calculated. The temporal coherence was studied by introducing two fused silica
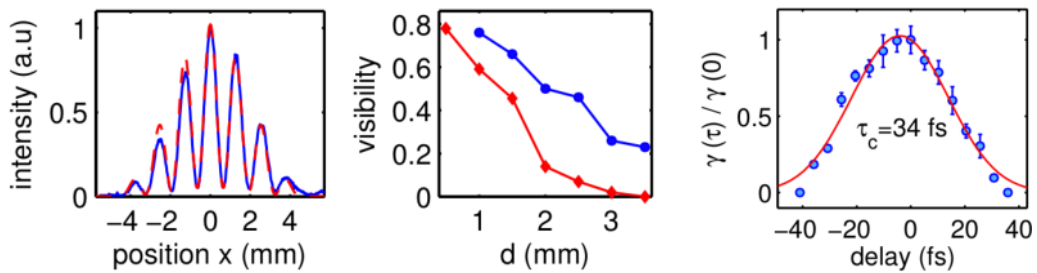
Fig. 2. (left) Measured interference pattern of 200-nm CHG radiation (blue) and a fit (red dashed line). (mid) The transverse coherence (visibility) as function of slit separation d measured with 400-nm (blue) and 200-nm (red) CHG radiation. (right) Measured longitudinal coherence function and a Gaussian fit.

wedges in front of each slit. By moving one wedge, the optical path length of one beam could be varied. From the resulting fringe pattern, the coherence time could be determined to be $\tau_c \sim 34$ fs, which is in good accordance with the results from a Michelson interferometer experiment. Another approach was the analysis of speckle patterns generated by single CHG pulses scattered from a thin organic film [4] in an ongoing collaboration with the workgroup of Prof. C. Gutt of the University of Siegen.

---

[1]Courtesy: B. Schmidt, S. Wunderlich, DESY/Hamburg.

II. CHG Operation with RF-Phase Modulation

Since 2009, an RF-phase-modulation system is in operation at DELTA in order to suppress coupled-bunch-oscillations and improve the beam life time [5]. This is achieved by a harmonic phase-modulation of the accelerating RF field of the DELTA cavity with a frequency close to twice the synchrotron oscillation frequency, with is approx. 15.2 kHz. Two effects occur: (i) The synchrotron spread increases, which leads to increased Landau damping, and by this suppresses coupled-bunch-modes. (ii) Due to the disturbed RF-potential, the mean bunch length increases, resulting in a reduced electron density and an increase of the beam life time of approx. 2 hours. For CHG operation a high electron density is required. Thus the bunch elongation by the RF-phase modulation has a deteriorating effect on the CHG and THz signals. By synchronizing the RF-phase modulation to the laser repetition rate, detailed studies of its influence on the CHG and THz signals were possible [6]. On streak camera images different modulation regimes could be observed, where the bunch shows a breathing behavior or the formation of two oscillating islands, see Fig. 3. Common to all regimes is the change of bunch length over time. Setting the synchrotron tune to an integer multiple
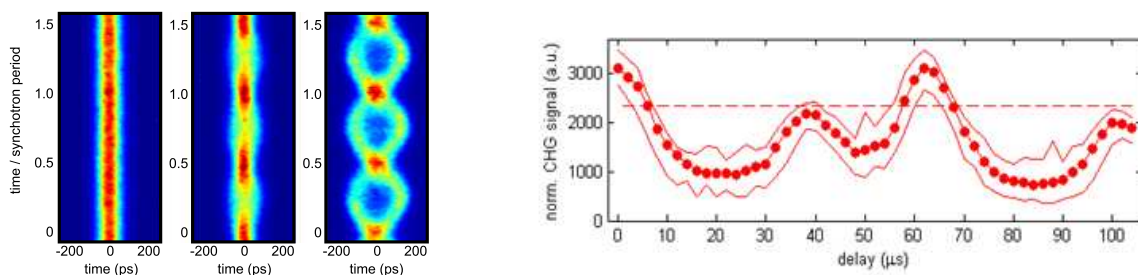
Fig. 3. (left) Evolution of the longitudinal bunch profile (abscissa) over 1.5 synchrotron oscillation periods (ordinate) observed with a streak camera with different parameter sets of RF-phase modulation. (right) CHG signal under the influence of RF-phase modulation after synchronization with varying delay. The dashed line indicates the signal level without RF-phase modulation

of the laser repetition rate of approx. 1 kHz with a variable phase delay allowed triggering the laser at different phases of the synchrotron oscillation, resulting in an up to 30% stronger CHG signal. This indicates a reduced bunch length with a higher electron density at at certain phases of the oscillation. Reconcilement of CHG with RF-phase modulation for increased beam life time and undisturbed CHG is an important step towards CHG operation under standard user conditions and a topic of further studies.

III. Towards Pump-Probe Experiments at Beamline 5 / Beamline 5a

To enable pump-probe experiments, a fraction of each laser-pulse is guided to the beamline 5 experimental station in an evacuated laser beamline. The beam path length in the 53 m long beamline can be slightly adjusted by a variable delay stage with an accuracy of approximately 15 μm. Spatial overlap of both pulses on the sample is established using the corresponding mirrors and observing the sample with a CCD camera. Temporal overlap is established by using two-photon absorption by recording the signal of a SiC-diode, which is blind to visible light, with a Keithley ampéremeter and varying the delay between both pulses. CHG radiation at the 3rd harmonic (9.3 eV) of the 400-nm seed was routinely detected at BL 5 using photoelectron spectroscopy with an intensity 30 times higher than the spontaneous radiation. As preparations are nearly completed, first pump-probe experiments on a Co/Cu magnetic system using the linear magnetic dichroism effect in order to study the demagnetization dynamics in this thin-film system will be performed soon.

As mentioned before, ultrashort and coherent THz pulses can be observed at the beamline 5a, which, too, offers the possibility of pump-probe experiments. The experiments at beamline 5a are covered by the report of J. Raasch.

References

[1] S. Khan et al., Sync. Rad. News 26, 25 (2013)

[2] P. Ungelenk et al., Proc. of Int. Part. Acc. Conf., 1936 (2014).

[3] M. Huck et al., Proc. of Int. Part. Acc. Conf., 1849 (2014).

[4] C. Gutt et al., Phys. Rev. Lett. 108, 024801 (2012).

[5] J. Fürsch, PhD thesis, TU Dortmund (2014).

[6] S. Khan et al., Proc. of Int. Beam Instr. Conf. (2014).

Tunable narrowband THz radiation for the investigation of the frequency-dependent picosecond response of YBCO detectors

J. Raasch[1*], M. Arndt[1], K. Ilin[1], A. Kuzmin[1], M. Siegel[1], S. Hilbrich[2], M. Höner[2], H. Huck[2], M. Huck[2], S. Khan[2], C. Mai[2], A. Meyer auf der Heide[2], R. Molo[2], H. Rast[2], P. Ungelenk[2†], S. Bielawski[3], C. Evain[3], M. Le Parquier[3], E. Roussel[3], C. Szwaj[3]

[1]Institute of Micro- and Nanoelectronic Systems, Karlsruhe Institute of Technology, Germany
[2]Center for Synchrotron Radiation (DELTA), TU Dortmund University, Germany
[3]PhLAM/CERLA, Université Lille 1, France

Intense, coherent, focused and pulsed THz sources as well as ultrafast, sensitive, low-noise and easy-to-handle THz detectors have become of increasing interest for scientists and companies in the fields of biology, medicine, plasma physics, nondestructive testing and security. Here, we report on the generation of narrowband THz radiation at DELTA, TU Dortmund, in cooperation with PhLAM/CERLA, Université Lille 1, and its application to characterize $YBa_2Cu_3O_{7-x}$-based (YBCO) THz detectors developed at the Institute of Micro- and Nanoelectronic Systems (IMS) at KIT, Karlsruhe.

At the DELTA short-pulse facility for VUV and THz radiation [1], ultrashort laser pulses interact with a short slice (usually 50-100 fs) of the electron bunches (100 ps FWHM) in an electromagnetic undulator (Fig. 1, left). Due to the energy-dependent path length in the subsequent magnets, the resulting modulation of the electron energy is converted into a sub-ps dip in the longitudinal electron density, which gives rise to coherent, broadband radiation pulses in the THz regime [2,3].
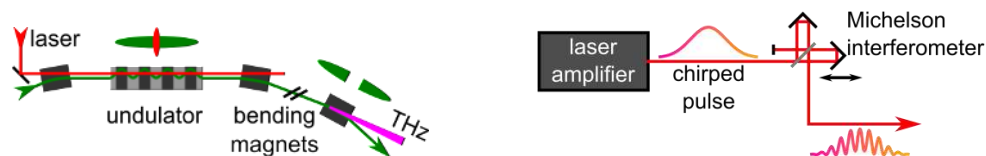
Figure 1: Setup of the short-pulse facility at DELTA (left) and chirped-pulse beating technique (right). See text for details.

Using the so-called chirped-pulse beating (CPB) technique [4], at which chirped laser pulses are sent through a Michelson interferometer leading to a periodic intensity modulation with variable frequency (Fig. 1, right), narrowband radiation pulses in the sub-THz range have successfully been generated at the UVSOR storage ring in Okazaki, Japan, for several years [4,5]. Recently, a CPB setup was installed at the DELTA short-pulse facility [7], which allowed reducing the bandwidth of the emitted THz pulses down to 0.3 THz and shifting the central frequency between 0.7 and 5.5 THz (Fig. 2).
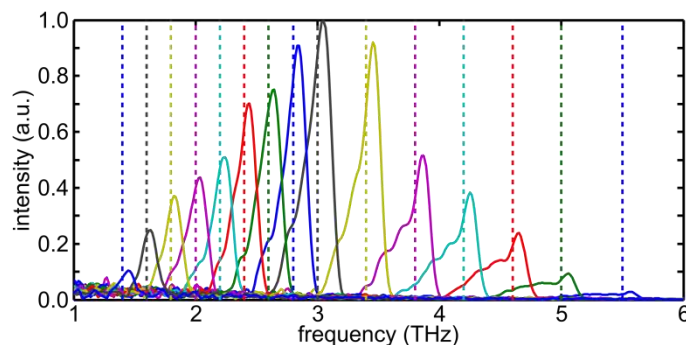
Figure 2: Narrowband THz spectra measured with an FT-IR spectrometer. Pulses with central frequencies down to 0.7 THz were generated. However, the spectra are limited to central frequencies above 1.3 THz due to a cutoff of the employed beam splitter. Dashed lines indicate the modulation frequency of the laser pulses as measured with an optical autocorrelator.

At the IMS in Karlsruhe, ultrafast direct THz detectors based on the high-temperature superconductor YBCO are developed and fabricated. Combining intrinsic relaxation times of less than 2 ps [8] with broadband readout, a temporal resolution of 16 ps (FWHM) has been demonstrated [9]. Figure 3(a) shows a scanning electron microscope picture of the detector. The YBCO thin-film has a thickness of 30 nm and the lateral dimensions of the detecting element amount to 1.0 µm in width and 0.2 µm in length. The YBCO detector is embedded in a broadband THz antenna and a coplanar readout line, both patterned into a 150 nm thick gold film [10]. The bandwidth of the log-spiral THz antenna ranges from 150 GHz up to more than 2.5 THz [11].

The response of a YBCO detector to optical and infrared wavelengths can be explained in the framework of the two-temperature model in which the detector acts as a hot-electron bolometer [12]. A photon with higher energy than the superconducting energy gap of YBCO ($2\Delta(0K) \approx 20$ meV [13]) is directly absorbed by the electron system of the detector which leads to a breaking of Cooper pairs. Contrarily to that, at low THz frequencies the photon energy is not sufficient to exceed the gap energy (1 THz ≜ 4.1 meV). Investigations with broadband synchrotron THz radiation have shown that the YBCO detector reacts to the electrical field of the radiation rather than to the intensity [11, 14]. Along with the possible operation of the detector without any applied bias current, this rules out a conventional bolometric behavior. In fact, the observed phenomena can be explained by the generation of magnetic flux quanta (vortices) moving through the YBCO detector generating a voltage pulse [15]. In the framework of this model the polarity of the detector response depends on the direction of motion of the vortices and thus on the phase of the electrical field of the THz pulse. The use of tunable narrowband THz radiation pulses now enables investigations of the frequency-dependent behavior of the YBCO detector. A transition from the vortex-based detection to the hot-electron effect is expected to be observed at a few THz, corresponding to the superconducting energy gap of YBCO.
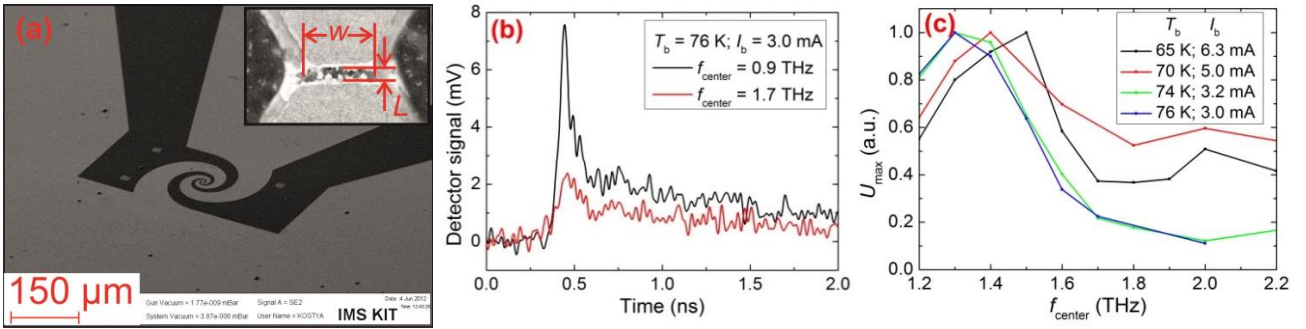
Figure 3: (a) Broadband THz antenna and coplanar readout line with a YBCO detector in the center of the antenna. Gold is depicted in light grey, the sapphire substrate appears in dark grey. (b) Detector signal for given bath temperature and bias current for two central frequencies. (c) Averaged detector signal depending on operation regime and central frequency.

The bias current for a given bath temperature was adjusted above the critical current of the detector. This way, at frequencies below the superconducting energy gap a nanosecond-scaled bolometric component is seen in the detector response in addition to the picosecond-scaled response due to the motion of vortices. The fast component disappears at higher frequencies, when the photon energy exceeds the superconducting energy gap. Two exemplary signal traces are shown in Fig. 3(b): For a central frequency below the superconducting energy gap (0.9 THz) and for $f_{center} = 1.7$ THz, where the fast component has already disappeared. In Fig 3(c), the time-averaged signal height depending on the central frequency is plotted for different bath temperatures and bias currents. Far below the critical temperature ($T_c = 81.5$ K), the drop in signal appears around $f_{center} = 1.6$ THz (≜ 6.6 meV) and is shifted to $f_{center} = 1.4$ THz (≜ 5.7 meV) for temperatures closer to T_c. The measured photon energy at which the picosecond detector response disappears is significantly smaller than the literature value for the superconducting energy gap ($2\Delta(70K) = 11.9$ meV). Moreover, the observed temperature dependence does not correspond to the relatively strong decrease of the energy gap near T_c. Therefore, the exact excitation frequency at which the vortex motion sets on along with its temperature dependence need further investigation.

We have demonstrated the generation of tunable narrowband THz radiation in the range of 0.7 THz to 5.5 THz. The investigation of the frequency-dependent YBCO detector response revealed the expected reduction of the signal at a given photon energy. Hence, a detailed quantitative study of the transition between vortex motion and the hot-electron effect in superconducting YBCO detectors is feasible within the scope of the presented experimental method.

References

[1] S. Khan et al., Sync. Rad. News 26, 25 (2013).
[2] P. Ungelenk et al., Proc. of IPAC, 768 (2012).
[3] P. Ungelenk et al., Proc. of IPAC, 94 (2013).
[4] A. S. Weling and D. H. Auston, J. Opt. Soc. Am. B 13, 2783 (1996).
[5] S. Bielawski et al., Nature Physics 4, 390 (2008).
[6] C. Evain et al., Phys. Rev. ST Accel. Beams 13, 090703 (2010).
[7] P. Ungelenk et al., Proc. of IPAC, 1936 (2014).
[8] M. Lindgren et al., Appl. Phys. Lett. 74, 853 (1999).
[9] P. Thoma et al., Appl. Phys. Lett. 101, 142601 (2012).

[10] P. Thoma et al. IEEE Trans. Appl. Supercond. 23, 2400206 (2013).
[11] P. Probst et al., Phys. Rev. B 85, 174511 (2012).
[12] A. D. Semenov et al., Supercond. Sci. Tech. 15, R1 (2002).
[13] G. Deutscher et al., Rev. Mod. Phys. 77, 109 (2005).
[14] J. Raasch et al., accepted for IEEE Trans. Appl. Supercond., Oct. 2014.
[15] D. Y. Vodolazov and F. M. Peeters, Phys. Rev. B. 76, 014521 (2007).

Ruby-fluorescence pressure calibration for x-ray diffraction studies using diamond anvil cell

C. Weis, C. Sternemann, J. Nyrow, M. Tolan

Fakultät Physik/DELTA, Technische Universität Dortmund, 44221 Dortmund, Germany

Since the invention of the diamond anvil cell (DAC) in 1959 [1] parts of the Earth's crust and Earth's lower mantle can be studied in-situ under extreme conditions. With increasing depth, high pressure (up to 360 GPa) and temperature (up to 6000 K) cause structural and/or electronic phase transitions which may have a strong influence on material's properties in the inner Earth [2]. Hence, high pressure DAC experiments evolved to a key tool in understanding the structure and dynamics of the Earth's crust, mantle, and core.

A ruby-fluorescence spectrometer was developed to enable online pressure calibration for x-ray diffraction (XRD) studies using a diamond anvil cell at BL9 of DELTA (see figure 1, left). The pressure is determined by measuring the position of the R1-line in the ruby-fluorescence spectrum (figure 1, right) employing the pressure-dependent wavelength shift via calibration of Mao et al. [3]. The spectrometer allows to monitor the sample in the DAC optically for alignment. The ruby-fluorescence is excited using a 450 nm laser and detected by a USB4000 spectrometer from Ocean Optics optimized for a wavelength range of 320-800 nm.
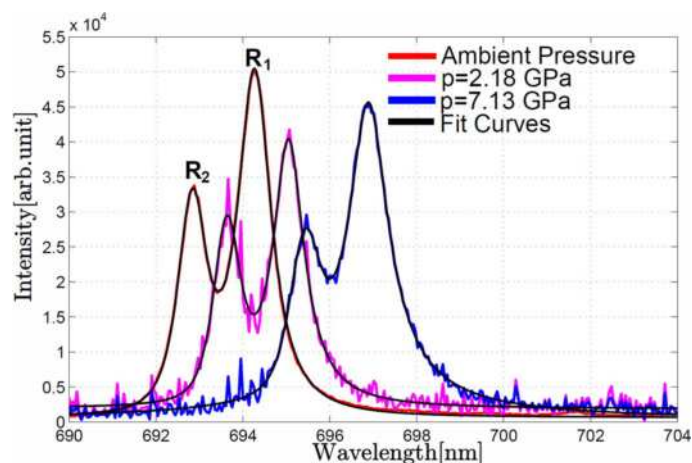
Figure 1: Left: Ruby-fluorescence spectrometer to measure the pressure in a diamond anvil cell. Right: Measured ruby-fluorescence spectra during a high pressure x-ray diffraction experiment at BL9.

First high-pressure XRD measurements using a preliminary setup were performed on reference materials such as magnetite (Fe_3O_4), wustite (FeO), and siderite ($FeCO_3$) loaded in Böhler-Almax diamond anvil cells. The experiments were performed at the beamline BL 9 of DELTA using a MAR 345 image plate detector to acquire two dimensional diffraction images (figure 2, left). The samples were loaded with alcohol as a pressure medium into a rhenium gasket which is fixed between the diamond culets. For pressure determination, a ruby was placed in the sample volume. XRD measurements were performed for different pressures up to 7.5 GPa. The one dimensional diffraction patterns were obtained by

azimuthal integration of the detector images using the software package Fit2D [4]. In figure 2 (right) the results for magnetite at pressures of 2.18 and 7.13 GPa are shown. As can be seen, the signal of the sample is accompanied by rhenium reflections from the gasket material indicating that the beamsize reduction at the sample position has to be optimized. The crystal structure of Fe_3O_4 at these pressures is given by Fe^{3+} occupying tetrahedral sites and Fe^{2+} together with the remaining Fe^{3+} ions occupying the octahedral sites in the spinel structure (space group Fd3m [5]). The corresponding diffraction patterns were calculated with the software Poudrix [6] and the lattice constant was refined according to pressure to fit the measurements. Good overall agreement was obtained showing only a small pressure gradient in the sample, which confirms the ability of carrying out high-pressure x-ray diffraction studies at BL9 of DELTA.
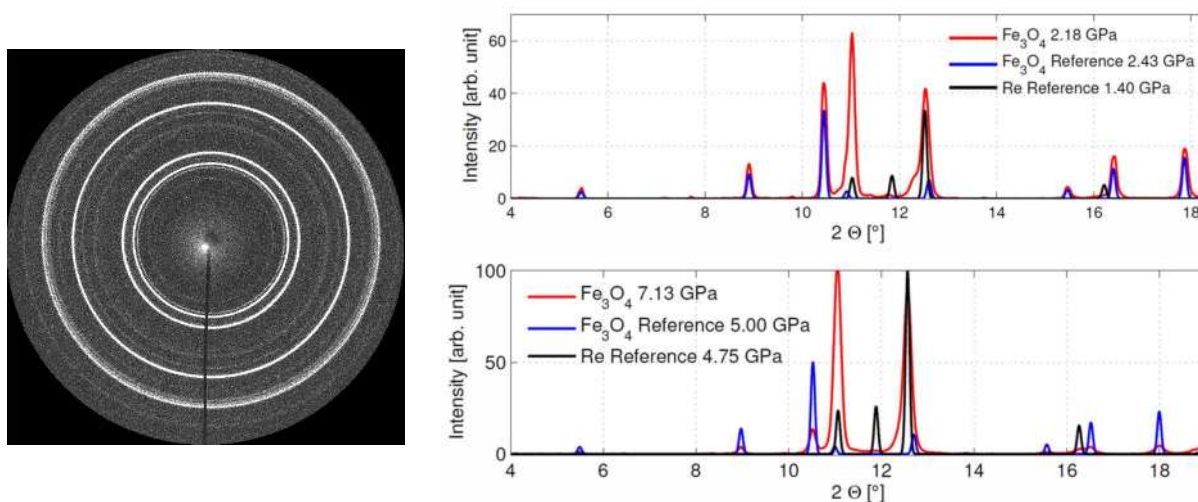
Figure 1: Left: Two-dimensional detector image of a magnetite sample. Magnetite and rhenium reflections of the gasket material can be observed. Right: Integrated diffraction patterns of magnetite at different pressure. For comparison diffraction patterns were modeled to fit the experimental data. This way the pressure was estimated from calculated diffraction patterns. Bragg reflections of the rhenium gasket material are indicated.

[1] C.E. Weir, E.R. Lippincott, A. Van Valkenburg and E.N. Bunting, Journal of Research NBS, 63A:55-62, 1959 [2] T.S. Duffy, Nature, 451:269-270, 2008 [3] H.K. Mao, J. Xu and P.M. Bell, J. Geophys. Res., 91:4673-4676, 1986. [4] A.P. Hammersley, S.O. Svensson, M. Hanfland, A.N. Fitch and D. Häusermann, High Pressure Research, 14:235-248, 1996. [5] M.E. Fleet, Acta Crystallographica, B37:917-920, 1981 [6] Poudrix, Program for the calculation of diffractograms, http://www.ccp14.ac.uk/tutorial/lmgp/poudrix.htm

Rocking curve measurements of a new weak-link channel-cut crystal design

Oliver von Polheim, Oliver Müller, Ralph Wagner, Dirk Lützenkirchen-Hecht, Ronald Frahm

Fachbereich C - Physik, Bergische Universität Wuppertal, Gaußstr. 20, 42097 Wuppertal, Germany.

According to Braggs law, a monochromator crystal does not simply reflect a single specific X-ray wavelength, but its higher harmonics as well, i.e. the wavelengths with a multiple of the fundamental one. These harmonics may distort the experiment, especially in the case of X-ray absorption spectroscopy (EXAFS / XANES), and thus they have to be filtered by an often complex and expensive X-ray mirror or by detuning of the monochromator crystals. While this can easily be done in a conventional double-crystal monochromator, such a detuning is difficult for a monolithic channel-cut crystal. Here we present a new design for a channel-cut crystal with the advantage of a detuning capability. A piezo-actor is used to bend the upper part of the crystal in a way that the reflecting surfaces are no longer parallel to each other but tilted by a few µrad. To optimize the properties of such a bendable crystal, various finite element simulations using "Comsol Multiphysics" [1] have been performed [2]. The optimized crystal geometry is shown in Fig. 1. In addition to the thick and stiff back plane, which also allows it to be used in a QEXAFS-monochromator, there is a rectangular cutout in the upper part where required mechanics and the piezo-actor are installed [2].
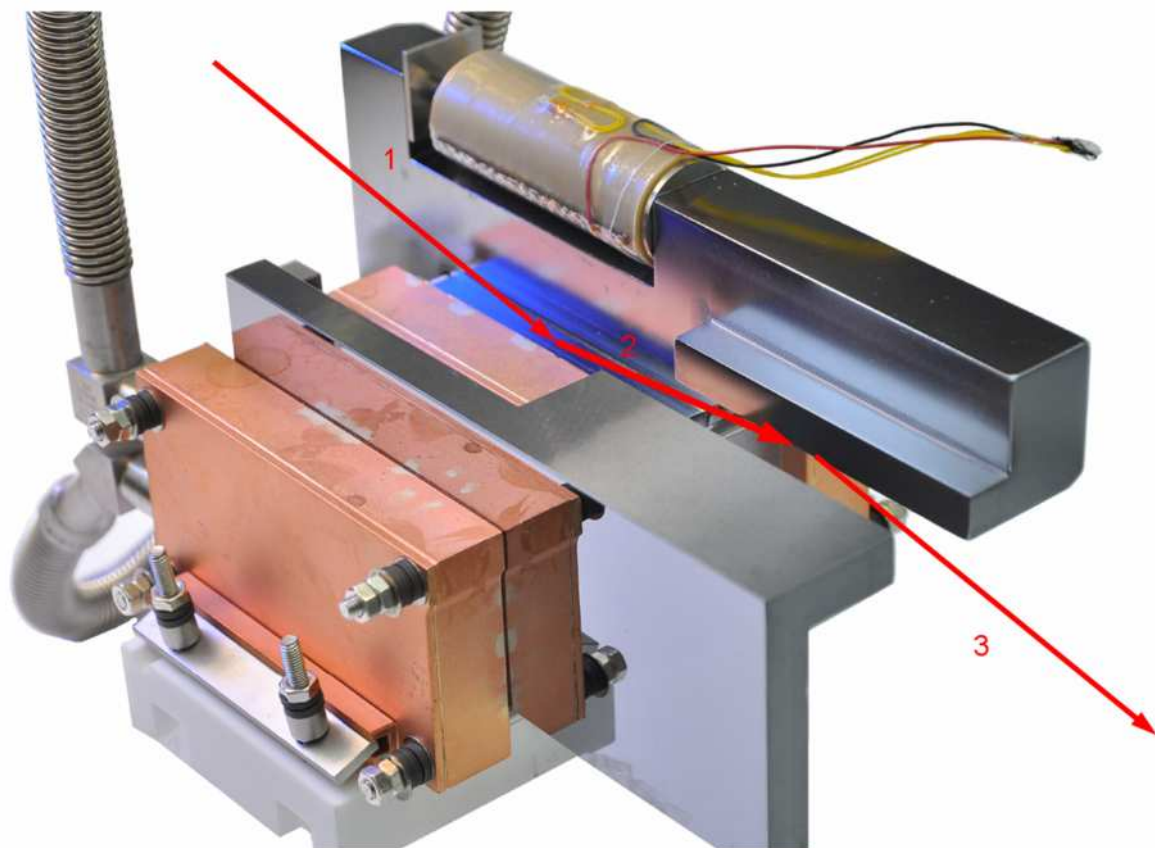
Fig. 1: Photo of the weak-link channel-cut crystal with the piezo actuator mounted next to a generic channel-cut crystal. The X-ray beam hits the first surface and is reflected upwards to the second surface. The parallism between the two surfaces can be adjusted by means of a piezo-actuator.

In Fig. 2 the setup of the rocking-curve experiment at DELTA beamline 10 [3] is shown. The measurements were performed with a fixed angle Θ_S of the channel-cut, while the angle of the Si(111) monochromator Θ_M was scanned. In Fig. 3 the measured rocking-curves are shown for different piezo voltages. The decreasing intensity, depending on the piezo-voltage is clearly visible and is caused by a tilt of the reflecting planes. These results indicate that it is possible to suppress the content of higher harmonics by a proper detuning of the crystal using the piezo actuator. Therefore the quality of spectroscopic X-ray measurement can be improved easily without using X-ray mirrors.
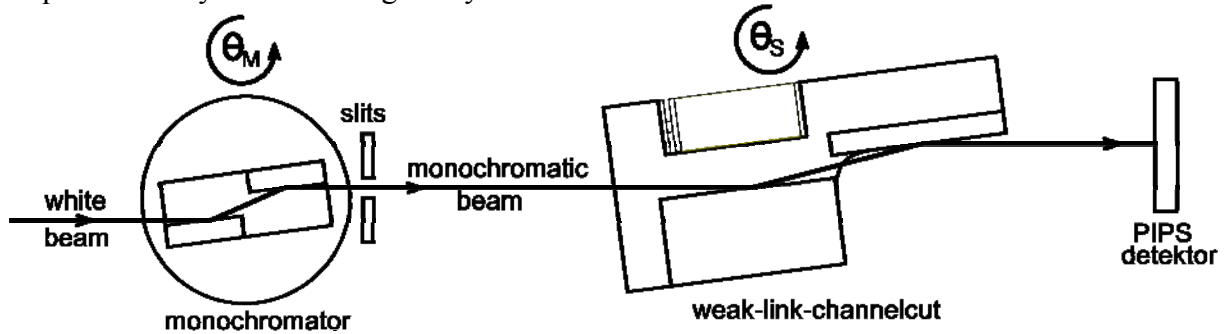
Fig. 2: Set-up for the rocking-curve measurements at beamline 10. A monochromatic beam with an energy depending on the actual Bragg angle Θ_M is provided by the beamline monochromator. The weak-link channel-cut crystal is mounted on the diffractometer stage with angle Θ_S. Depending on the detuning by the piezo, the rocking curve of the crystal may be followed.
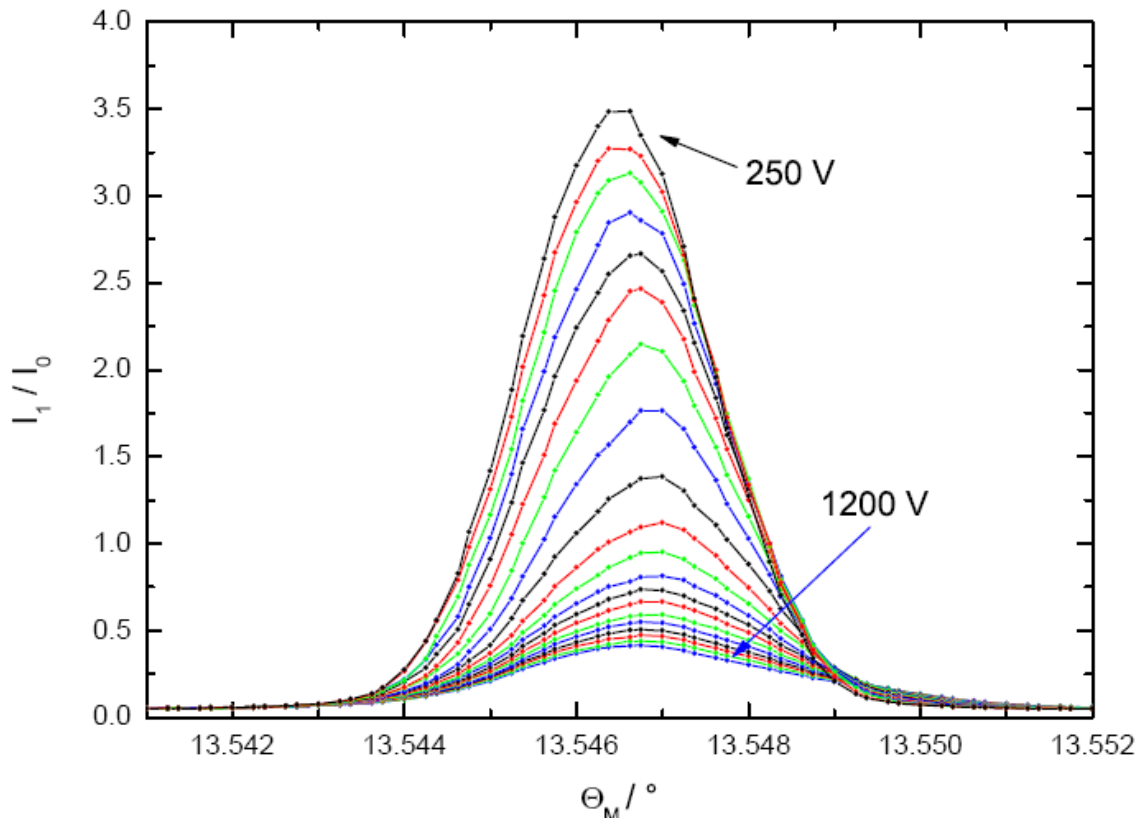
Fig. 3: Rocking-curves measured for different Bragg-angles of the beamline monochromator (Θ_M) and voltages at the tuning piezo of the weak-link channelcut crystal (in steps of 50 V).

References
[1] Comsol Multiphysics, Göttingen, Germany
[2] O. von Polheim, Masters thesis, Universität Wuppertal (2014)

Soft X-ray Spectroscopy

Beamline 5: Momentum and spin resolved investigation of the electronic band structure using angle resolved photoemission spectroscopy

Mathias Gehlmann[1], Sven Döring[1], Stefan Cramm[1], Lukasz Plucinski[1] and Claus M. Schneider[1]

[1]Peter Grünberg Institut, PGI-6, Forschungszentrum Jülich GmbH, D-52425 Jülich, Germany

At beamline 5 we investigate the electronic band structure of spintronic materials using angle resolved photoemission spectroscopy (ARPES). Using the combination of a hemispherical analyzer with a two dimensional delay line detector (DLD) we are able to measure the kinetic energy of outgoing photoelectrons as a function of their emission angle. This information can be translated into the electronic band dispersion of the material. In addition a spin-polarized low-energy electron diffraction (SPLEED) detector allows simultaneous measurement of in-plane and out-of-plane components of the photoelectron spin.
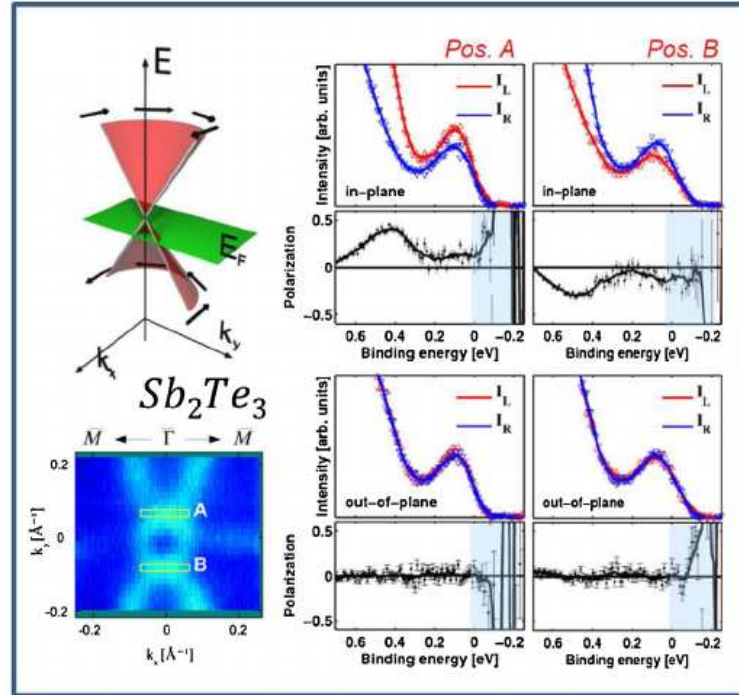
Figure 1: Spin-polarized data taken near the Fermi level for a Sb_2Te_3 thin film at $h\nu = 24$ eV and selected k-space locations along the $\overline{\Gamma K}$ direction. The top row indicates the in-plane spin-vector component intensities, whereas the out-of-plane intensities are plotted in the lower row. The computed spin-asymmetries P_x and P_z are plotted below the corresponding intensity plots with standard deviations given by vertical error bars, whereas the solid line represents smoothed data.

One of our recent projects was a momentum and spin resolved study of the 3D topological insulator Sb_2Te_3 grown on Si(111) substrate [1][2]. Due to the spin texture of the topologically protected surface state, which is characteristic for this class of material, Sb_2Te_3 might allow a highly efficient spin injection for spintronic devices. For application, however, this fascinating physical property must withstand the typical device processing conditions. Therefore we studied samples that were exposed to atmospheric air and subsequently annealed, resulting in a relatively rough surface covered by impurities and surface defects.

With our photoemission experiments which are shown in Figure 1 we could confirm the robustness of the topologically protected surface state. There one can clearly observe the Dirac cone in the momentum resolved cut through the Brillouin zone close to the Fermi level. Furthermore the spin resolved spectra prove the helical character of the surface state with a spin polarization of up to 40% in-plane and no out-of-plane spin polarization.

13

Another major project at beamline 5 is the investigation of the band structure of molybdenum disulfide (MoS_2). This material has a remarkable chemical and mechanical stability and fascinating electronic properties that might lead to novel applications in optoelectronics and spintronics [3]. Our major interest in this material is focused on its complex spin texture. We plan to investigate band structure of single crystals and two dimensional films of MoS_2 in the future.

In order to enable such experiments a new ultra high vacuum manipulator has been constructed and installed at our beamline. The major advantage of the new setup is the possibility to cool the sample with liquid nitrogen and to rotate it orthogonally to the direction that is resolved by the spectrometer. The additional degree of freedom allows us to efficiently map large areas in two dimensional momentum space. Figure 2 shows one of the first results that were obtained with the new setup. This experiment was performed on a Cu(111) single crystal using a photon energy of $h\nu = 47$ eV. In this figure the x- and y-axes are the two momentum components of the photoelectrons parallel to the sample surface and the z-axis shows its kinetic energy. The surface state can be observed at the center of both the first (upper left) and second surface Brillouin zone (upper right). The top-side of the slab represents the blend of the certain cut through the 3-dimensional Fermi surface of fcc-Cu with the 2-dimensional Fermi surface of Cu(111).
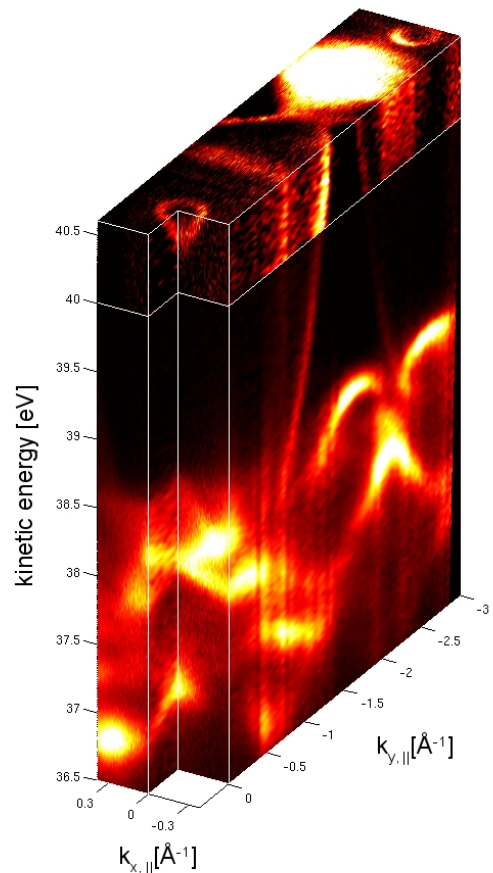
Figure 2: Band structure mapping of Cu(111) using ARPES with a photon energy of $h\nu = 47$eV. The contrast above $E_{kin} = 40$ eV has been enhanced.

References

[1] L. Plucinski and C.M. Schneider. The electronic structure of spintronic materials as seen by spin-polarized angle-resolved photoemission. *J. Electron. Spectrosc. Relat. Phenom.*, 189:137, (2013).

[2] L. Plucinski, A. Herdt, S. Fahrendorf, G. Bihlmayer, G. Mussler, S. Döring, J. Kampmeier, F. Matthes, D. E. Bürgler, D. Grützmacher, S. Blügel, and C. M. Schneider. Electronic structure, surface morphology, and topologically protected surface states of Sb_2Te_3 thin films grown on Si(111). *J. Appl. Phys.*, 113(5), (2013).

[3] K. F. Mak, C. Lee, J. Hone, J. Shan, and T. F. Heinz. Atomically thin Mos_2: A new direct-gap semiconductor. *Phys. Rev. Lett.*, 105:136805, (2010).

Beamline 5: Angle-resolved magnetic linear dichroism in resonant photoemission of 3d metal thin films

Torsten Veltum[1*], Tobias Löffler[1], Sven Döring[2], Mathias Gehlmann[2], L. Plucinski[2] and Mathias Getzlaff[1]

[1] Institut für Angewandte Physik, Heinrich-Heine-Universität Düsseldorf, 40225 Düsseldorf
[2] Peter Grünberg Institut PGI-6, Forschungszentrum Jülich, 52428 Jülich
* torsten.veltum@uni-duesseldorf.de

Magnetic linear dichroism in the angular distribution of photoelectrons (MLDAD) is a technique that allows the study of both the electronic band structure and the magnetic properties of thin films and single crystals. In this study we use linearly polarized synchrotron radiation in the VUV regime.

The first two studied systems are a thin hcp(0001) Co film and a thin bcc(110) Fe film, both epitaxially grown on a W(110) single crystal. Preliminary characterization of the thin film is carried out by LEED. The easy magnetization axis for thin Co films lies in-plane and along the $[1\bar{1}00]$-direction, which corresponds to the $W[1\bar{1}0]$-direction. The easy magnetization direction for thin iron films lies also along the $W[1\bar{1}0]$-direction for a thickness below 65 Å [1]. The magnetic linear dichroism requires a specific geometry as displayed in Fig. 1, where the linearly polarized light scatters in the xz-plane and the sample is magnetized in the y-direction. We magnetize the sample before every measurement with a retractable permanent magnet.

The results of the photoemission spectra in normal emission between 21 and 37 eV excitation energy are shown in Fig. 2. On the left side the results for a 8 ML thick Co film are shown, where you can see a clear dichroism signal with asymmetries of up to 7 %. On the right side the results for a 15 ML thick Fe film are shown, displaying asymmetries of up to 12 %. For both materials the dichroism effect vanishes for excitation energies above 30 eV.

The effect of MLD is nearly zero for all energies above 30 eV, with the exception of around 54 eV for iron and 60 eV for cobalt. At these energies we observe resonant photoemission as well as a dichroism effect, as shown in Fig. 3. The resonance at these energies is between the 3p and the valence band. The 3p core-level has a binding energy of 54 and 60 eV for iron and cobalt, respectively. For cobalt, the asymmetry reaches values of about 8 %, which is comparable to the values observed at lower energies. Iron on the other hand doesn't show a great effect, which can be explained by looking at the magnetic linear dichroism in the angular distribution. The angle-resolved spectra show a high angle-dependence with often opposite effects at opposite angles. The angular spectra will not be shown here, because it would go beyond the constraints of this article.
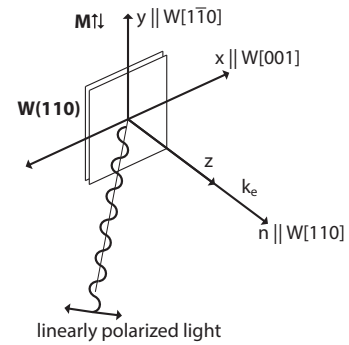
Figure 1: Geometric arrangement of sample and incoming photon beam with linear polarized radiation. The photoelectrons are detected in normal emission.

[1] M. Getzlaff et al., Z. Phys. B 104, (1997), 11-20
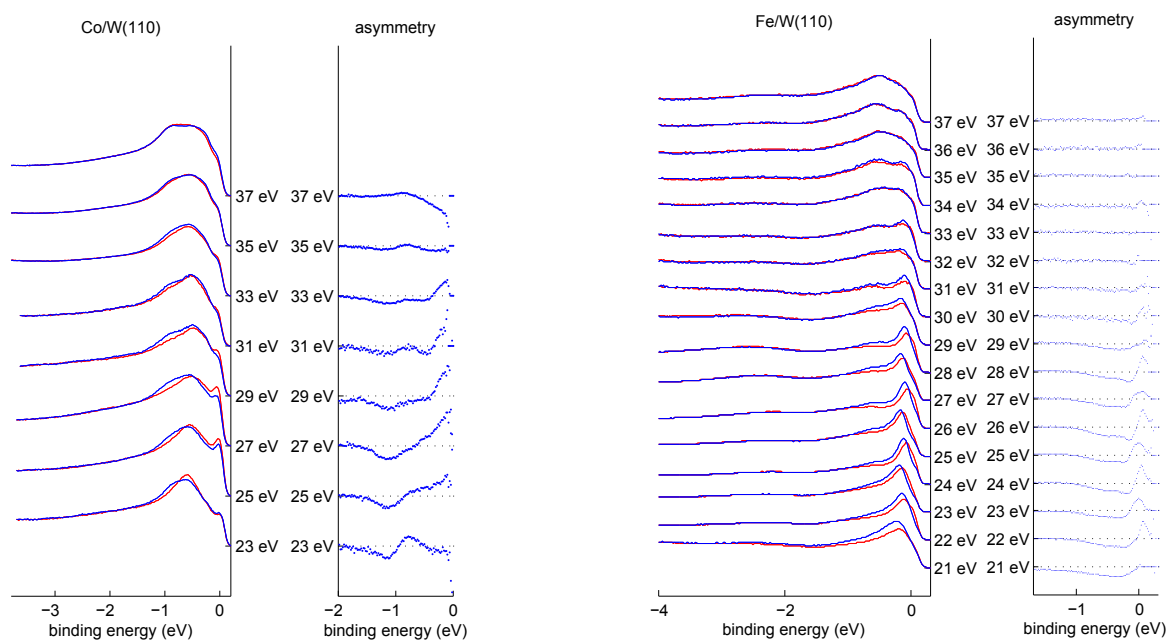
Figure 2: Valence band photoelectron spectra from a) 8 ML thick hcp(0001) Co film and b) 15 ML bcc(110) Fe film on tungsten with linearly polarized light at energies between 21 and 37 eV for opposite magnetization directions.
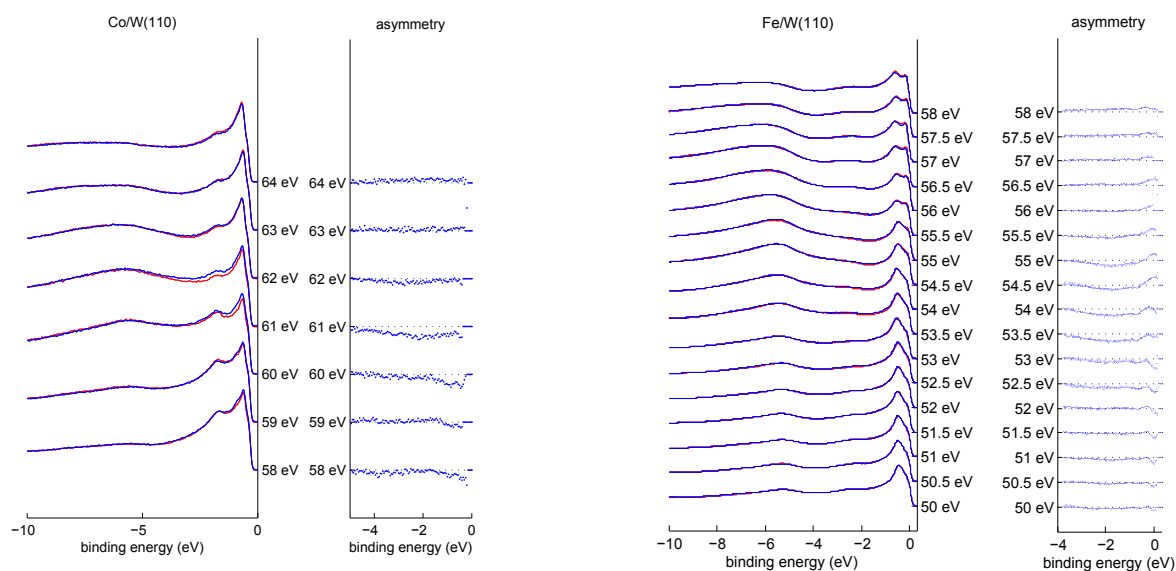
Figure 3: Valence band photoelectron spectra from a) 8 ML thick hcp(0001) Co film and b) 15 ML bcc(110) Fe film on tungsten with linearly polarized light at excitation energies around the 3p core-levels for opposite magnetization directions.

Reflection Spectroscopy across the C 1s edges of Graphene/SiC

C. Jansing[1], H. Wahab[2], M. C. Gilbert[1], D. Handschak[3], E. Diemke[3],
C. Keutner[3], U. Berges[3], C. Westphal[3], H. Timmers[2], H.-Ch. Mertins[1]

[1]: *Münster University of Applied Sciences, Stegerwaldstr. 39, D-48565 Steinfurt*
[2]: *University of New South Wales Canberra,, PO Box 7916, Canberra BC ACT 2610, Australia*
[3]: *Technische Universität Dortmund, August-Schmidt-Straße 4, 44227 Dortmund*

Abstract:

Soft x-ray reflection spectra for graphene grown on SiC have been measured with p-polarized synchrotron radiation at the DELTA synchrotron. The results demonstrate that reflection spectroscopy enables a clear separation of the excitation of carbon 1s states located in graphene from those located in the SiC substrate.

Graphene is a very promising material for future electronic devices such as nano-ribbon transistors [1, 2]. In order to understand the electronic properties of this novel material, it is indispensable to establish the electronic band structure of graphene [3]. While photoelectron spectroscopy techniques are suited to determine the valance band and core levels, reflection spectroscopy with synchrotron radiation is suited to probe conduction band states. Furthermore the use of linear polarized light and the appropriate orientation of the linear polarization plane allows for the selective excitation of perpendicular to the plane oriented π-states and excitation of in-plane oriented σ-states. Reflection spectroscopy is element-selective, since the relevant absorption edges occur at different energies.

We measured Graphene/SiC samples and the pure SiC substrate prepared in Dortmund by flash annealing in ultrahigh vacuum [4]. The reflection spectra were performed with our UHV-chamber "XMAPS" [5] at room temperature in May and June 2014 at the undulator beamline 11 at the DELTA synchrotron facility. We used p-polarized light with an energy resolution of E/ΔE= 2500. Figure 1 illustrates schematically the experimental geometry. For different angles Θ measured to the samples surface the reflectivity was detected as the function of photon energy across the carbon 1s edge. A normalization of the spectra is possible due to quasi-simultaneous detection of reflected and the I_0-signal. The detected reflectance results from two contributions: reflectance of the incoming intensity I_0 at the Graphene surface giving $I_0 R_G$ and the intensity $I_0 R_{SiC} T^2_G$ reflected at the SiC substrate after transmission of the Graphene layer. The relative amount of both contributions depends on the reflectance R_G of Graphene, its transmission coefficient T_G and the reflectance of the substrate R_{SiC} which acts like a mirror.
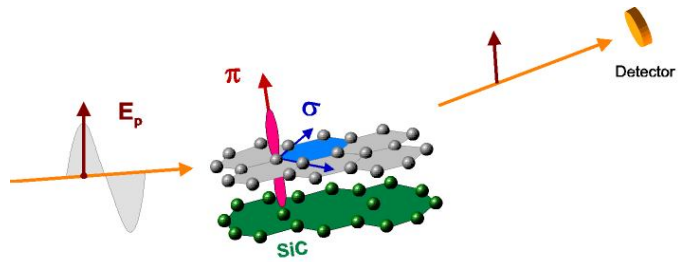
Fig. 1: Experimental geometry. The p-polarized light is reflected by the Graphene/SiC sample and detected by a diode. The π- and σ-bondings are indicated.

Figure 2 shows reflection spectra for linearly polarized light (p-polarization) across the carbon 1s - edge for different angles of incidence Θ. With increasing incidence angle Θ two trends are observed: Firstly, the reflectance decreases according to the Fresnel-equations and to the influence of diffuse scattering at the rough substrate SiC. Secondly, a local maximum of the reflectance can be identified at 286 eV which is the π-resonance energy. This resonance peak is caused by the incident p-polarized light predominantly exciting states that correspond to the

1

π-bonds that are parallel aligned to the electric field vector of the light. This peak becomes more dominant with increasing angle of incidence because the ratio of reflectance from the graphene top layer to that from the SiC substrate changes. The SiC-substrate's roughness leads to more diffuse scattering of the component $I_0 R_{SiC} T^2_G$ which enhances the contribution of $I_0 R_G$, reflected at the Graphene surface, in the measured signal.

In contrast, the σ-resonance of carbon bonds, which is approximately 6eV above the π-resonance in graphene, results in a decrease of the reflectance with angle of incidence. For Θ > 10° a local minimum of the reflectance near 293 eV can be seen. This minimum could be caused by exciting the σ-states followed by a decreased transmission coefficient T_G of the Graphene layer which leads to a reduced overall reflectance component $I_0 R_{SiC} T^2_G$. Excitation of σ-states are possible even with p-polarized light due to the component $\sin(\Theta)$ of the electric field which is parallel to the σ-bonds.
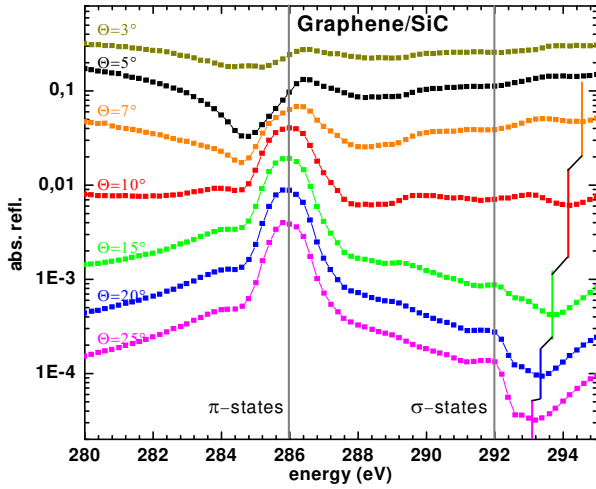
Fig. 2: *Reflection spectra of Graphene/SiC for different angles of incidence.*
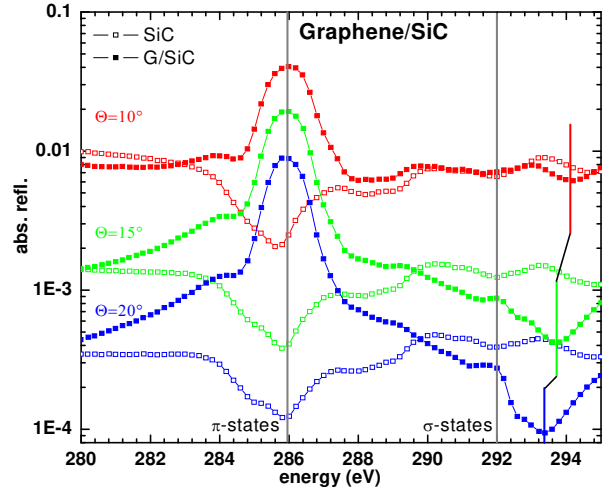
Fig. 3: *Comparison of reflectance for the SiC substrate and Graphene/SiC.*

However, this process and the observed energy shift of the σ-resonance, which does not occur for the π-resonance, and is indicated in Fig. 2, is not completely understood and needs more investigation with s-polarized light in order to enhance the response of the σ-states.

The comparison with a reference SiC sample of the substrate material (open symbols in Fig. 3) enables the separation of the contribution of Graphene (filled symbols in Fig. 3) to the measured reflection signal. In contrast to the graphene sample the substrate SiC shows a minimum in the reflectance at 286 eV. At the σ-resonance near 293 eV the inverse behavior is observed. Importantly, this comparison clearly indicates that the energy shift of the σ-resonance only occurs for Graphene/SiC but not for the substrate, indicating that it originates from carbon in Graphene.

In conclusion we have shown that the separation of signals from carbon in the graphene layer and from carbon in a SiC substrate is possible. Furthermore, the angle-dependence of reflection spectroscopy allows for an enhancement of the graphene contribution with respect to that of the substrate.

[1] A. H. C. Neto, F. Guinea, N. M. R. Peres, K. S. Novoselov, and A. K. Geim, Mod. Phys. **81**, 109 (2009)
[2]: Zhihong Chen, Yu-Ming Lin, Michael J. Rooks, Phaedon Avouris Physica E **40** (2007)
[3]: E. Kogan ,V. U. Nazarov, Phys. Rev. B **85**, 115418 (2012)
[4]: Qingyan Wang, Wenhao Zhang, Lili Wang, Ke He, Xucun Ma, Qikun Xue J. Phys.: Condens. Matter **25** (2013)
[5]: M. F. Tesch, M. C. Gilbert, H.-Ch. Mertins, D. E. Bürgler, U. Berges, and C. M. Schneider, Appl. Opt. **52** (2013)

Graphene Oxide Characterisation with Reflection Spectroscopy

Hud Wahab[1], Guangyuan Xu[2], Christine Jansing[3], Markus Gilbert[3], Marc Tesch[3],
Jianyong Jin[2], Hans-Christoph Mertins[3], Christoph Keutner[4], Ulf Berges[4], Heiko Timmers[1]

[1] School of Physical, Environmental and Mathematical Sciences, UNSW Canberra, ACT 2600, Australia
[2] School of Chemical Sciences, University of Auckland, Auckland 1142, New Zealand
[3] University of Applied Sciences Münster, Stegerwaldstrasse 39, 48565 Steinfurt
[4] Technische Universität Dortmund, August-Schmidt-Straße 4, 44227 Dortmund

Abstract

Synchrotron radiation reflection spectroscopy across the K-edge of carbon has been performed on graphene oxide samples fabricated with two different methods. Preliminary results suggest that the two methods can be distinguished and that the presence of specific molecular groups, such as the carbonyl group π^*(C=O) and the hydroxyl group π^*(C-OH), may be confirmed.

Introduction

Graphene oxide (GO) is studied as a possible precursor in the commercial fabrication of graphene [1]. Among a variety of synthesis techniques for GO, *Hummers' method* [2] and a method developed by *Tour* [3] are well documented and are frequently applied [4]. Knowledge of the structure of GO materials is important to the explanation of electronic properties observed for the graphene obtained.

While Near Edge X-ray Absorption Spectroscopy (NEXAFS) studies of GO have been reported [5], no such information has been published for reflection spectroscopy. Using synchrotron radiation the latter technique may provide complementary information, as the excited carbon 1s electrons populate different states than in NEXAFS. Furthermore, unlike NEXAFS, samples are probed to greater depths. Such depth sensitivity may be controlled by varying the angle of incidence.

Experiment

Soft x-ray reflection spectroscopy was performed at *Beamline 11* using the *U55 undulator* [6]. Figure 1 illustrates the experimental setup. The GO samples were placed at the centre of the reflectometry chamber, which has been designed to also enable magneto-optical experiments [7]. Each GO sample was positioned, so that its surface normal is horizontal. Beam direction and surface normal thus define the optical scattering plane.

The incident beam intensity I_{in} was measured prior to each reflection measurement $R_{2\theta}$ in order to account for the gradual loss with time, and any variation, of beam intensity. The sample was positioned at a desired angle of incidence, θ, that was taken, as indicated in Fig. 1, as the angle between the incident beam and the sample surface. The angular positioning of the sample stage has an accuracy of at least 0.1°. Reflection measurements were performed over the angular range θ = 2 - 4°. Beyond θ = 4° the intensity of light reflected from the GO samples was observed to be too low to permit accurate quantification.
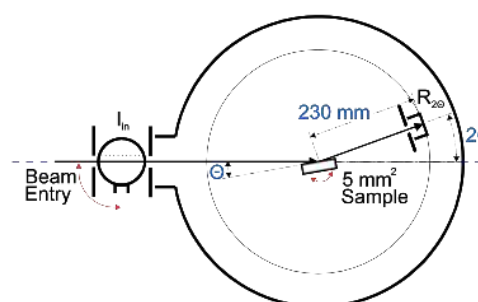
Fig. 1 *Schematic overview of the reflection spectroscopy setup (not to scale).*

Results

Figure 2 displays the measured reflection spectra for graphene oxide using the *Hummers-* and *Tour-methods*, respectively. Results are shown for θ = 2°, 3°, and 4°.

Two main local minima can be identified in the spectra that are present for both methods and seen at all three angles. These may be interpreted as the lowest energy π* resonance (285 eV) and the highest energy σ* resonance (291 eV) and attributed to the C-C 1s to π* and the 1s to σ* transitions, respectively.

For GO from the *Tour-method*, a further resonance minimum is observed at 289 eV that may be assigned to the carbonyl group π*(C=O) in –COOH. For such material a fourth resonance may be present at 287 eV that has been tentatively assigned to the basal-attached hydroxyl group π*(C-OH). The presence of the two additional resonances in material from the *Tour-method* may be seen more readily in Fig. 3, which displays for each angle the difference between the spectra shown in Fig. 2.
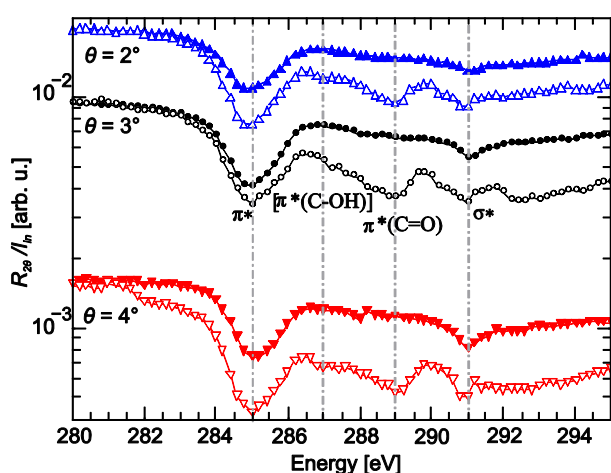
Fig. 2 *Reflection spectroscopy at θ = 2°, 3° and 4° of graphene oxide fabricated with the methods by Hummers (closed symbols) and Tour (open symbols).*
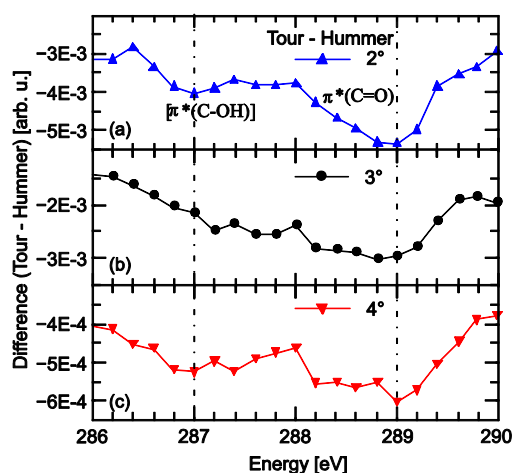
Fig. 3 *Differences between the spectra shown in Fig. 2 for (a) θ = 2°, (b) θ = 3° and (c) θ = 4°, identifying additional resonances that may be present in material from the method by Tour.*

Conclusions

Explorative reflection spectroscopy of graphene oxide samples has shown that two important fabrication techniques may be differentiated. In particular, results may suggest that there are more oxidized groups present in material fabricated with the method by *Tour*, when compared with material from *Hummers' method*, which is in agreement with other reports [3]. A detailed account of these measurements will be submitted to *X-ray Spectrometry*.

References

[1] S. Stankovich, D.A. Dikin, G.H.B. Dommett, K.M. Kohlhaas, E.J. Zimney, E.A. Stach, R.D. Piner, S.T. Nguyen, R.S. Ruoff, Nature, 442 (2006) 282-286.

[2] W.S. Hummers, R.E. Offeman, J. Am. Chem. Soc., 80 (1958) 1339-1339.

[3] D.C. Marcano, D.V. Kosynkin, J.M. Berlin, A. Sinitskii, Z. Sun, A. Slesarev, L.B. Alemany, W. Lu, J.M. Tour, ACS Nano, 4 (2010) 4806-4814.

[4] M. Khenfouch, U. Buttner, M. Baitoul, M. Maaza, Graphene, (2014) 7-13.

[5] C.H. Chuang, Y.F. Wang, Y.C. Shao, Y.C. Yeh, D.Y. Wang, C.W. Chen, J.W. Chiou, S.C. Ray, W.F. Pong, L. Zhang, J.F. Zhu, J.H. Guo, Sci. Rep., 4 (2014) 1-7.

[6] U. Berges, M. Krause, M. Schürmann, S. Dreiner, R. Follath, F. Schäfers, C. Westphal, AIP Conf. Proc., 705 (2004) 424.

[7] M.F. Tesch, M.C. Gilbert, H.C. Mertins, D.E. Bürgler, U. Berges, C.M. Schneider, Appl. Opt., 52 (2013) 4294-4310.

PEEM and XPS experiments on B-doped diamonds

C. Keutner[1,2,*], **U. Berges**[1,2], **D. Handschak**[1,2], **F. Schönbohm**[1,2], **P. Espeter**[1,2], **N. Wöhrl**[3,4], **R. Berendakova**[3,4], **V. Buck**[3,4], **C. Westphal**[1,2]

[1] Experimentelle Physik I - Technische Universität Dortmund, Otto-Hahn-Str. 4, D-44221 Dortmund
[2] DELTA - Technische Universität Dortmund, Maria-Goeppert-Mayer-Str. 2, D-44221 Dortmund
[3] Thin Film Technology - Universität Duisburg-Essen, Lotharstr. 1, D-47057 Duisburg
[4] CENIDE - Universität Duisburg-Essen, Carl-Benz-Str. 199, D-47057 Duisburg
* corresponding author: christoph.keutner@tu-dortmund.de

Ultra-Nanocrystalline diamond (UNCD) films are of wide interdisciplinary interest. Applications reach from surface acoustic wave devices to usage of their tribological properties in applied sciences and industry [1]. By adding boron as dopant during the microwave plasma enhanced chemical vapor deposition on Si, the electrical properties of the UNCD can be varied in a way, that the insulating diamond becomes conductive and even superconductive at low temperatures ($T < 1.66\,K$) [2].

Previous high resolution electron microscope (HREM) studies on cross-sectional specimen reveal different results concerning the existence of an SiC interface [3,4,5]. However, such an interface could effect the optoelectric properties of the film [6] and is therefore of particular interest. A useful method to access the interface structure directly, without any further manipulations like sectioning, is x-ray photoelectron diffraction (XPD). The objectives of this study are to reveal the sample's physical and chemical homogeneity and the accessibility of the interface by means of x-ray photoelectron spectroscopy (XPS) and XPD.

In a first step UNCD samples of different growth times were studied ex-situ by photoemission electron microscopy (PEEM). The PEEM images in threshold mode reveal the inhomogeneous size distribution of the diamonds. Different sized crystals can be seen at different locations on the sample surface (Figure 1). By comparing PEEM images of different samples with different growth times, an increasing inhomogeneity by decreasing growth time can be found. Further on, the god conductive properties of B-doped diamonds can be nicely seen by the absence of image defects due to charging. This also proves the successful doping of the diamonds, which can not be shown by XPS due to the low dopant concentration within the carbon matrix.
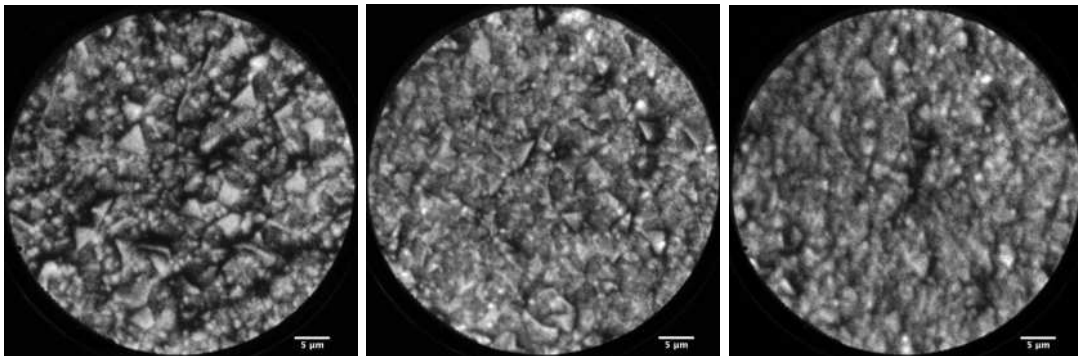
Figure 1: PEEM images of different sample positions revealing the samples inhomogeneity with different sized crystals.

Judging on the PEEM images, the most homogeneous samples were chosen for further XPS studies. These reveal regions with significant more B content than expected for doped diamonds. By analyzing a high resolution B 1s spectrum (Figure 2) it becomes clear, that this signal is dominated by boron and boron oxides, rather than boron carbide. These components are associated with remains of the CVD process, rather than dopant atoms. Further, a faint Si signal reveal an over all too thick top layer, which prevent an access to the interface for this set of samples.
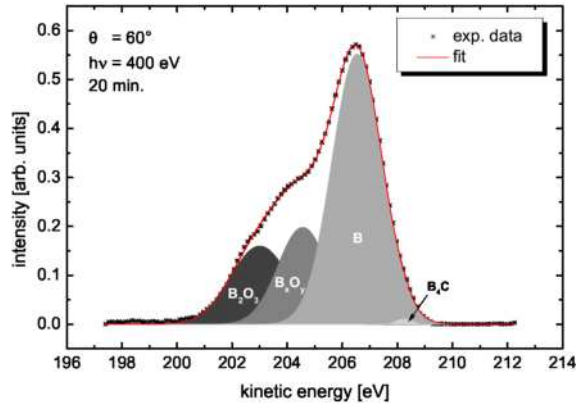
Figure 2: Result of the least-squares fit of a B 1s spectrum. The spectrum is dominated by boron and boron oxides. A boron carbide signal is also given, while of no significance to the least-squares fit.

In order to determine the distribution of different carbon species within the grown layer, XPS spectra at different polar angles (θ) were recorded. Hereby, spectra under grazing emission angles ($\theta = 60°$) are more surface sensitive than spectra taken at normal emission angles ($\theta = 0°$).

Carbon 1s spectra of two different sample positions are shown in Figure 3. For each position a spectrum at $\theta = 0°$ as well as $\theta = 60°$ was taken. The least-squares fits reveal three components. The C sp^2-hybridization state corresponds to graphitic carbon, which is formed in early stages of the diamond growth and partly remains as impurity in the diamond film [7]. Diamond itself is given by the C sp^3-hybridization state, bound $\sim 1\,eV$ tighter than C sp^2. The third component corresponds to an oxide, also forming during the growth phase.

The composition of the carbon species vary drastically for both positions. The first sample position shows a slightly, depth dependent change in the C sp^2/ C sp^3-relation, whereas the composition of the second position stays nearly unchanged. However, C sp^3 clearly dominates the signal of the second position, whereas C sp^2 and C sp^3 are nearly equal in height for the first position.

Here, we could demonstrate that the combination of PEEM and XPS is suitable for the investigation of B-doped diamond films. In order to access the silicon-diamond-interface by XPS and XPD, further efforts are needed to develop a preparation method yielding thinner and more homogeneous films.
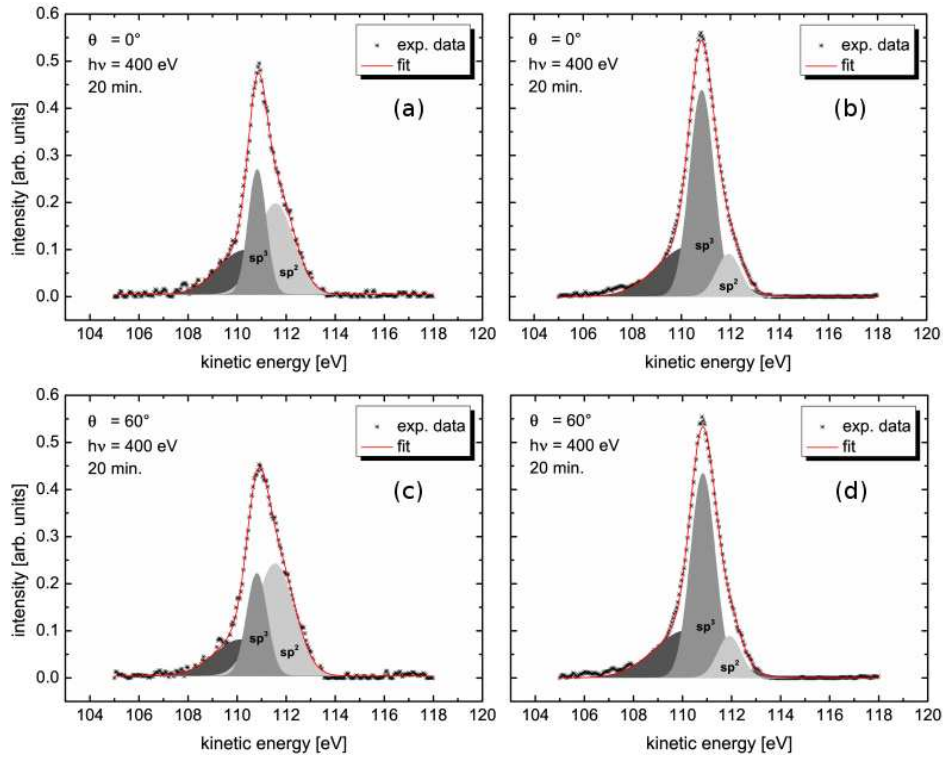
Figure 3: Least-squares fit of C 1s spectra of two different sample positions (a,c) and (b,d). The spectra are recorded at $\theta = 0°$ (a,b) and $\theta = 60°$ (c,d) in order to enhance the bulk and surface sensitivity, respectively.

Acknowledgement

References

[1] C. A. Charitidis, E. P. Koumoulos, and D. A. Dragatogiannis, *Lubricants* **1**, 22-47 (2013.)

[2] M. Nesládek, D. Tromson, C. Mer, P. Bergonzo, P. Hubik, and J. J. Mares, *Appl. Phys. Lett.* **88**, 232111 (2006).

[3] B. E. Williams and J. T. Glass, *J. Mater. Res.* **4**, 373 (1989).

[4] R. Meilunas, M. S. Wong, K. C. Sheng, R. P. H. Chang, and R. P. Van Dyne, *Appl. Phys. Lett.* **54**, 2204 (1989).

[5] X. Jiang and C. L. Jia, *Appl. Phys. Lett.* **67**, 1197 (1995).

[6] M. M. Waite and S. I. Shah, *Appl. Phys. Lett.* **60**, 2344 (1992).

[7] S. I. Shah and M. M. Waite, *Appl. Phys. Lett.* **61**, 3113 (1992).

Characterization of the interfacial regime of Fe/GaAs(001) - Is a surface reconstruction really necessary for an epitaxial Fe growth?

D. Handschak, F. Schönbohm, T. Lühr, C. Keutner, U. Berges, and C. Westphal

Experimentelle Physik 1 and DELTA - Technische Universität Dortmund, Otto-Hahn-Str. 4, D-44221 Dortmund, Germany

Multilayer consisting of the ferromagnet Fe and the semiconductor GaAs are in the focus of the research in spintronics [1, 2] based on the Giant-Magneto-Resistance Effect (GMR). It arises at the interface, where electrons are scattered differently depending on their spin and mutual orientation of the magnetization within the ferromagnet. Therefore, the knowledge of the chemical composition and structure of the interface are important in order to improve the efficiency of the effect [3]. The x-ray photoelectron spectroscopy (XPS) and diffraction (XPD) are a very suitable tool for the investigation of this multilayer, because it is not only chemical and structural sensitive but also very sensitive to surface and interface regions [4]. The profiling depth can be adjusted by different excitation energies, which are provided by the U55 beamline 11 at DELTA. Two sample systems were compared, Fe/GaAs(clean) and Fe/GaAs(4×2). Firstly, Iron is prepared on an only cleaned and unreconstructed sample and secondly on the Ga-rich (4×2) surface reconstruction.

(a) Arsenic   (b) Gallium   (c) Iron
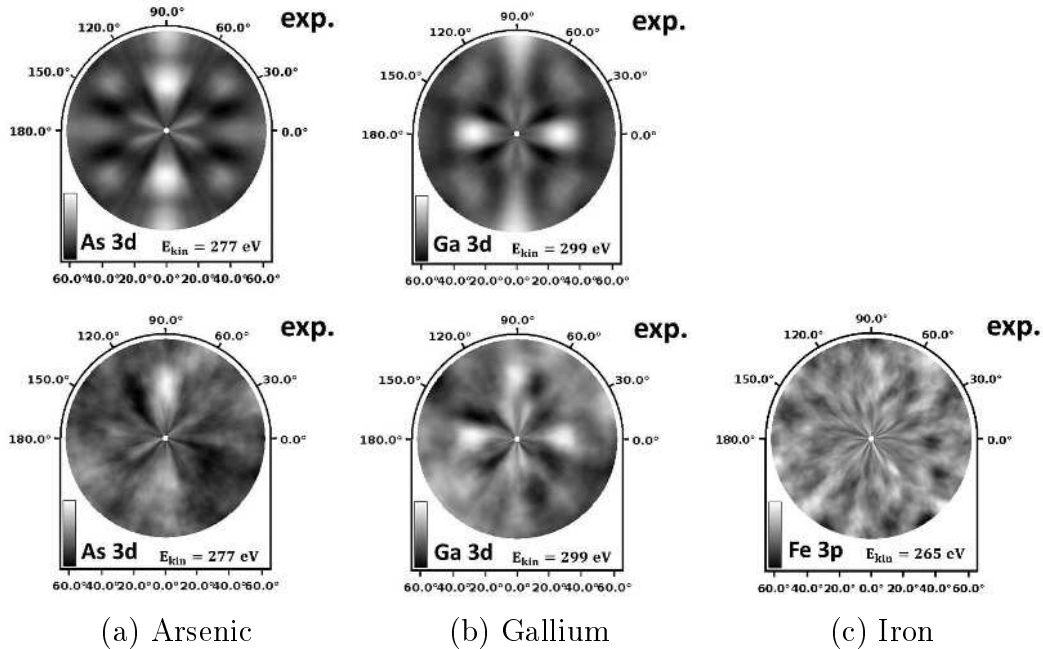
Figure 1: XPD patterns of the Fe/GaAs(clean) sample system before (top) and after (button) the Fe-deposition.

The XPD patterns of the Fe/GaAs(clean)-sample are shown in Fig. 1(a) in comparison to the patterns of the same signals with an additional 18 Å-thick Fe-film in Fig. 1(b). The reflexes and the twofold rotational symmetry can be directly associated to the zinc blende structure of the GaAs crystal. Theses reflexes almost vanish completely after the Fe-deposition, as can be clearly seen in Fig. 1. This can be explained by a strong inter-diffusion between the GaAs-substrate and the Fe-film. Furthermore, the very noisy Fe pattern shown in Fig. 1(c) impressively demonstrates the Fe-film being completely amorphous.

| (a) Arsenic | (b) Gallium | (c) Iron-surface | (d) Iron.interface |
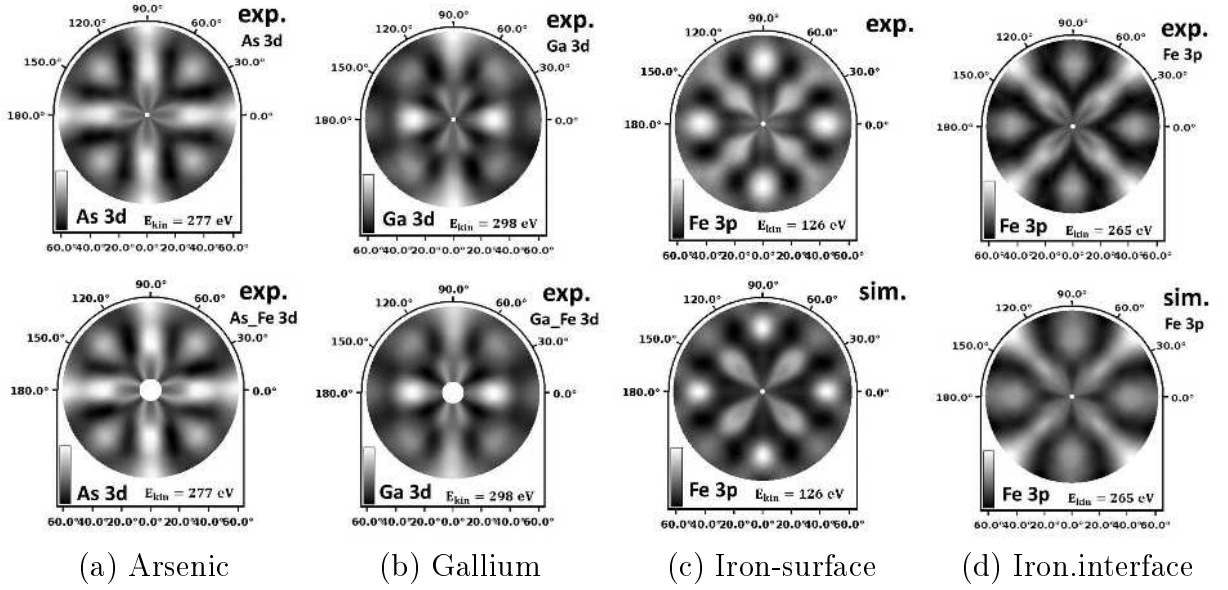
Figure 2: XPD patterns of the Fe/GaAs(4×2) sample system. In comparison, the experimental patterns of GaAs before and after the deposition (a-b) and the experimental and best simulated patterns of the Fe-film (c-d).

Accordingly, the XPD pattern of the Fe/GaAs(4×2)-system are shown in Fig. 2. The fourfold rotational symmetry of the Arsenic can be associated to the structure of the (4×2)-reconstruction having a lack of As-atoms. Again the twofold symmetry of Gallium is caused by the crystalline bulk. The patterns of the GaAs(4×2) after the Fe-deposition shown in Fig. 2(a) and (b) shown in the lower part of this figure reveal no changes. In other words, neither the substrate structure changes nor amorphous layers due to an inter-diffusion are detectable. Furthermore, the analysis of the patterns of the Fe-film detected with a surface and interface sensitive experimental geometry, see Fig. 2(c) and (d), resulted in a perfect crystalline Fe-film and interface structure. The fourfold rotational symmetry is due to the bcc structure and the analysis of the patterns reveal a pyramid-like structured Fe-film due to a simultaneous layer and island growth.

In summary, it can be impressively demonstrated that a surface reconstruction prevent an inter-diffusion between the GaAs(001) substrate and the Fe-adsorbate. The Fe-film was epitaxial prepared and shows excellent crystalline properties.

2

References

[1] G. Autès *et al.*, Theory of tunneling magnetoresistance of Fe/GaAs/Fe(001) junctions, Phys. Rev. B **82** (2010)

[2] B. Kardasz *et al.*, Spin dynamics and magnetic anisotropies at the Fe/GaAs(001) interface, J. Appl. Phys. **109**, (2011)

[3] Y. Xu *et al.*, Evolution of the ferromagnetic phase of ultrathin Fe films grown on GaAs(100)-4 × 6, Phys. Rev. B **58**, (1998)

[4] C. Westphal *et al.*, The study of local atomic structure by means of x-ray photoelectron diffraction, Surf. Sci. Rep. **50** (2003)

[5] D. Handschak *et al.*, Structural investigation of the three-layer system MgO/Fe/GaAs(001) by means of photoelectron spectroscopy and diffraction, Phys. Rev. B **88** (2013)

[5] D. Handschak *et al.*, Structure and magnetic characterization of the interfacial regimes of MgO/Fe/GaAs(001), submitted (2014)

3

Preparation of thin tetraphenylporphyrin layers in UHV and their characterization with XPS

L. Madalaye[1,2,*], L. Brosda[1,*], C. Keutner[1,2], D. Handschak[1,2], U. Berges[1,2], C. Westphal[1,2]

[1] Experimentelle Physik I - Technische Universität Dortmund, Otto-Hahn-Str. 4, D-44221 Dortmund
[2] DELTA - Technische Universität Dortmund, Maria-Goeppert-Mayer-Str. 2, D-44221 Dortmund
* corresponding author: linda.madalaye@tu-dortmund.de

Porphyrins are molecules found everywhere in nature, for example in blood as heme or in chlorophyll of some algae. They possess strong absorption bands which make them useful as photosensitizers in dye-sensitized solar cells[2]. They can form molecular complexes with many different metal atoms, e.g., heme is an iron porphyrin and chlorophyll c2 is a magnesium porphyrin. The reaction of thin porphyrin layers with metal atoms named metalation has been studied with many different metals such as Fe[1], Co[4], Ni[3], and Zn[5].
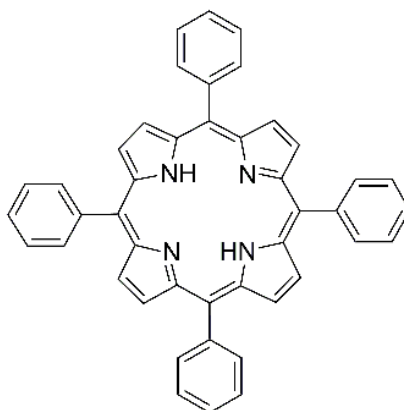
Figure 1: Structure of the tetraphenylporphyrin (2HTPP) molecule.

In this work, thin meso-tetraphenylporphyrin (2HTPP) films are prepared in situ using vapor deposition. The tetraphenylporphyrin films were deposited on a naturally oxidized Si(100) surface using a modified electron beam evaporator to sublimate 2HTPP powder (98% purity) at approximately 400°C. The 2HTPP molecule depicted in figure 1 possesses nitrogen atoms in two different binding states - the imminic (=N-) and pyrrolic (-NH-) nitrogen bonds. The chemical shift of the nitrogen's binding energy due to the two binding states is observed by means of XPS.

A high resolution XPS spectrum of nitrogen is pictured in figure 2. To increase surface sensitivity a polar angle of 60° was chosen. The XPS spectrum of N1s is deconvoluted (see figure 2). In the spectrum the pyrrolic and imminic nitrogen bonds are at 96.3 eV and 98.2 eV kinetic energy, respectively. A chemical shift of 2 eV between the bonds is calculated in agreement with Min Chen et al.[3]. The observation of the chemical shift in the nitrogen peak is confirmation for the successful deposition of the 2HTPP molecule without thermal decomposition. The reaction of the 2HTPP molecule with metal atoms can be easily observed in the nitrogen signal, as metalation leads to the loss of dihydrogen[1] and hence to four nitrogen atoms in identical bonds. This can be observed as one single nitrogen peak in the XPS spectrum. Measurements of the reaction of 2HTPP with different metal atoms will be performed in following beam times.
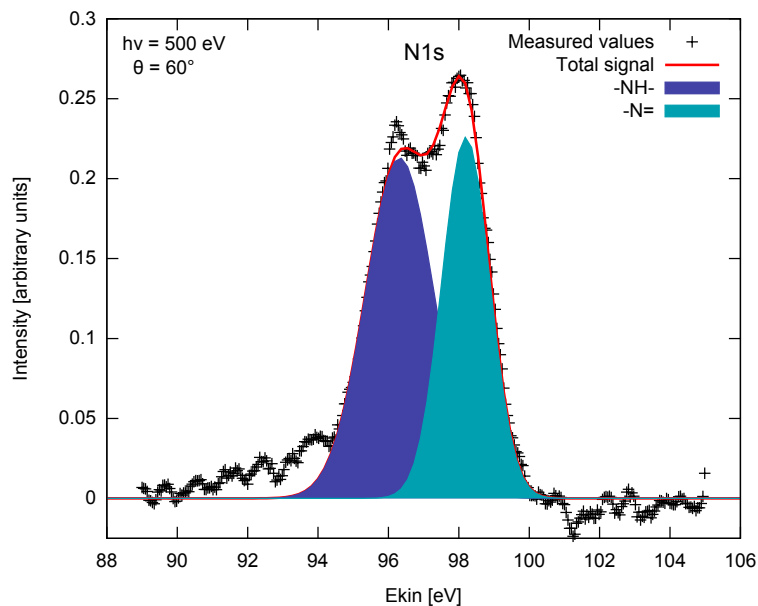
Figure 2: XPS spectrum of the N1s peak of the tetraphenylporphyrin molecule using a photon energy of 500 eV and with a polar angel of 60°. The left peak corresponds to the pyrrolic binding state at 96.3 eV and the right peak to the imminic binding state at 98.2 eV. The signal noise was reduced with 5 point adjacent averaging.

References

[1] Florian Buchner, Ken Flechtner, Yun Bai, Elisabeth Zillner, Ina Kellner, Hans-Peter Steinrück, Hubertus Marbach, and J. Michael Gottfried, *Coordination of iron atoms by tetraphenylporphyrin monolayers and multilayers on Ag(111) and formation of iron-tetraphenylporphyrin*, The Journal of Physical Chemistry C **112** (2008), no. 39, 15458–15465.

[2] Wayne M. Campbell, Anthony K. Burrell, David L. Officer, and Kenneth W. Jolley, *Porphyrins as light harvesters in the dye-sensitised TiO2 solar cell*, Coordination Chemistry Reviews **248** (2004), no. 13–14, 1363 – 1379, Michael Graetzel Festschrift, a tribute for his 60th Birthday, Dye Sensitized Solar Cells.

[3] Min Chen, Xuefei Feng, Liang Zhang, Huanxin Ju, Qian Xu, Junfa Zhu, J. Michael Gottfried, Kurash Ibrahim, Haijie Qian, and Jiaou Wang, *Direct synthesis of nickel(II) tetraphenylporphyrin and its interaction with a Au(111) surface: A comprehensive study*, The Journal of Physical Chemistry C **114** (2010), no. 21, 9908–9916.

[4] J. Michael Gottfried, Ken Flechtner, Andreas Kretschmann, Thomas Lukasczyk, and Hans-Peter Steinrück, *Direct synthesis of a metalloporphyrin complex on a surface*, Journal of the American Chemical Society **128** (2006), no. 17, 5644–5645, PMID: 16637625.

[5] Andreas Kretschmann, Marie-Madeleine Walz, Ken Flechtner, Hans-Peter Steinrück, and J. Michael Gottfried, *Tetraphenylporphyrin picks up zinc atoms from a silver surface*, Chem. Commun. (2007), 568–570.

XPS-study of mechanical exfoliated molybdenum disulphide

P. Espeter[1,2,*], C. Keutner[1,2], D. Handschak[1,2], U. Berges[1,2], C. Westphal[1,2]

[1] Experimentelle Physik I - Technische Universität Dortmund, Otto-Hahn-Str. 4, D-44221 Dortmund
[2] DELTA - Technische Universität Dortmund, Maria-Goeppert-Mayer-Str. 2, D-44221 Dortmund
* corresponding author: philipp.espeter@tu-dortmund.de

The transition metal dichalcogenide molybdenum disulphide (MoS_2) belongs to the layered materials with a strong in-plane and weak out-of-plane bonding. Thinning bulk MoS_2 down to monolayer thickness influences its electronic proporties. More precisely, the bandgap increases and changes from indirect to direct. MoS_2 monolayer with direct bandgap of about $1,9\,eV$ is a promising candidate for applications in electronic and opto-electronic devices [1]. A first evidence for possible application was given by Radisavljevic et al. who demonstrate a well performing field-effect-transistor based on MoS_2 [2]. Most recent a field-effect-transistor of entirely two-dimensional material, graphene, MoS_2, and bor-nitrid is reported [3]. Since, there is still a lack of knowledge of the interface between MoS_2 and other two-dimensional materials such as graphene preliminary tests on mechanical exfoliated MoS_2 were conducted. The purpose of these investigations is to test its ability for photoelectron diffraction (XPD) studies which yield structure information of the interface [4].

There are mainly two characteristics that a sample has to fulfill for photoelectron diffraction studies. Namely these are the sample's homogenity and the absence of unwanted contamination. High resolution XPS spectra of molybdenum and sulfur, pictured in figure 1, show the presence of vacancy formation and oxygen contamination. Component 1 is dedicated to fully coordinated molybdenum and sulfur atoms and component 2 is dedicated to sulfur vacancys due to the exfoliation process. Owing to the preparation under ambient conditions, single and double substitution of the sulfur by oxygen is observed, illustrated by components 3 and 4. Depiction of different components in real space is given in figure 2.
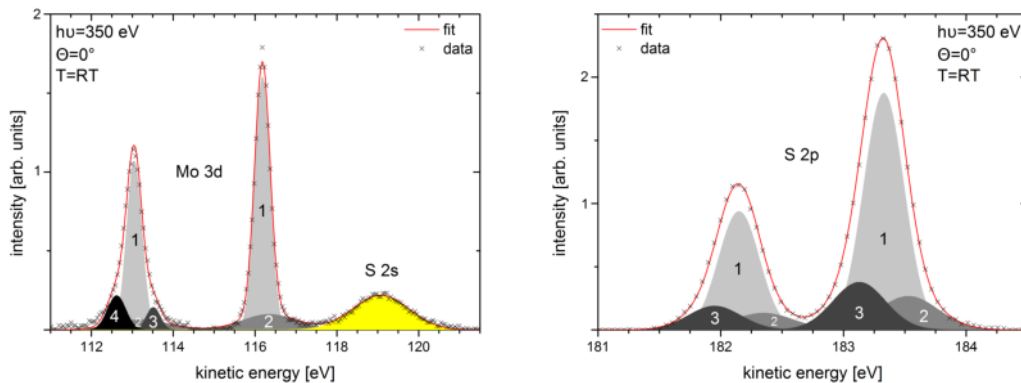
Figure 1: High resolution XPS spectra of (a) molybdenum-3d- and (b) sulfur-2p-peak.

Furthermore, it is a hint that mechanical exfoliated molybdenum disulphide lacks of the required homogenity. This observation is verified by investigations via optical microscopy.

Other preparations of monolayer MoS_2 via chemical and/or physical vapor deposition are still under investigation. The preparation of graphene, as it is needed for graphene/MoS_2 interface, is subject within another master thesis.
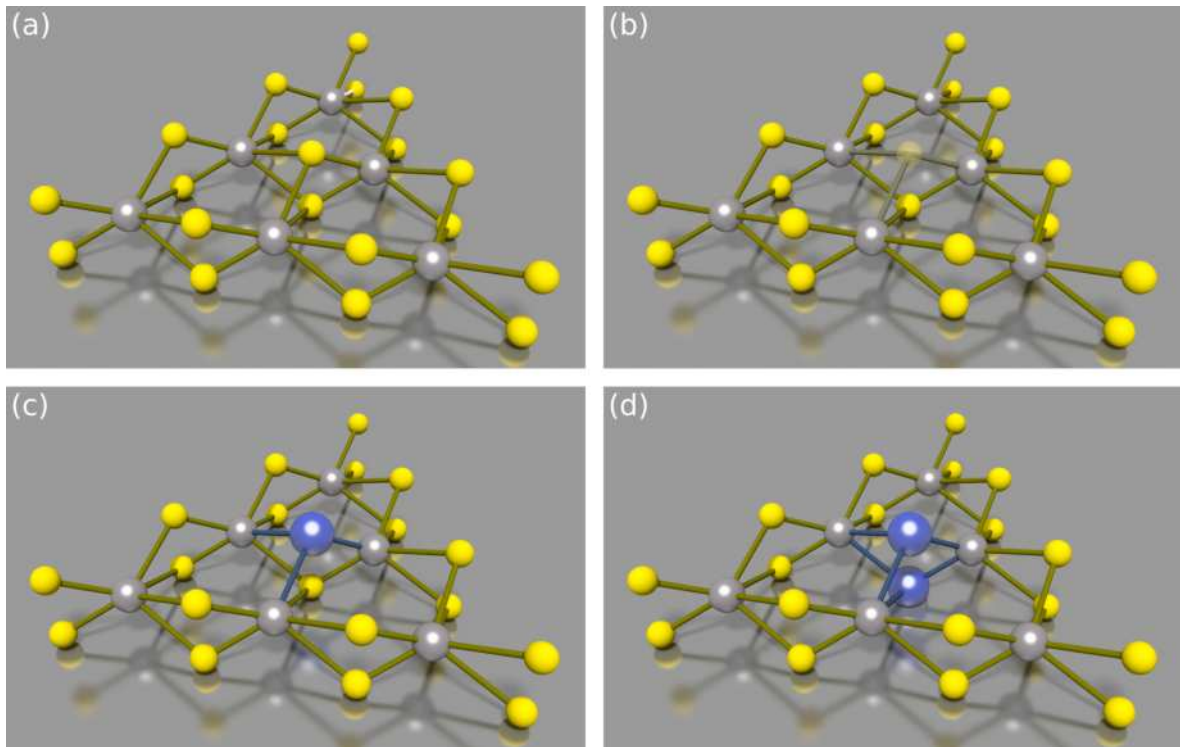
Figure 2: Depiction of (a) fully coordinated sulfur and molybdenum atoms, (b) sulfur vacancy formation, and (c) single, and (d) double oxydation.

References

[1] Q. H. Wang, K. Kalantar-Zadeh, A. Kis, J. N. Coleman und M. S. Strano, *Electronics and optoelectronics of two-dimensional transition metal dichalcogenides*, Nat. Nanotechnol. **7**, 699 (2012).

[2] B. Radisavljevic, A. Radenovic, J. Brivio, V. Giacometti und A. Kis, *Single-layer MoS$_2$ transistors*, Nat. Nanotechnol. **6**, 147 (2011).

[3] T. Roy, M. Tosun, J. S. Kang, A. B. Sachid, S. B. Desai, M. Hettick, C. C. Hu und A. Javey, *Field-Effect Transistors Built from All Two-Dimensional Material Components*, ACS Nano **8**, 6259 (2014).

[4] C. Westphal, *The study of the local atomic structure by means of X-ray photoelectron diffraction*, Surface Science Reports **50**, 1 (2003).

X-ray Scattering

VHCF Behaviour of an Austenitic-Ferritic Duplex Stainless Steel investigated during an in-situ experiment performed at BL10

Anne K. Hüsecken[1], Marcus Söker[2], Ulrich Krupp[2] and Ullrich Pietsch[1]
[1]Universität Siegen [2]Hochschule Osnabück

Austenitic-ferritic duplex stainless steel is normally used in offshore or petrochemical industries due to its excellent corrosion resistance and its high strength. There it has to resist cyclic loading up to 10 million cycles and more. Therefore it is very important to study the very high cycle fatigue (VHCF) behaviour of this material and how lifetime can be predicted. To do this the mechanisms inside the steel have to be investigated, which lead to crack initiation, crack propagation and finally to failure of the material.

Therefore an in-situ experiment was performed at beamline BL10 at DELTA. The used duplex steel (grade 1.4462) consists of Austenite (A, γ, fcc structure) and Ferrite (F, α, bcc structure) grains with an average grain size of 50µm (see Fig. 1c)). The sample was mounted on an Ultrasonic Fatigue Testing Machine (UFTM, from BOKU Vienna) and fixed at the Diffractometer (See Fig. 1a)).
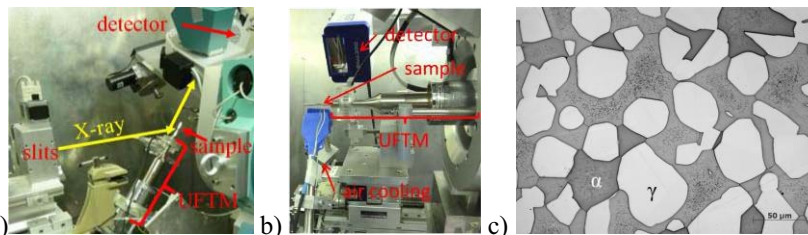
Fig.1 Experimental setup with a) vertical (after [2]) and b) horizontal position of the sample. c) Grain structure of used duplex steel [2].

By performing Rocking scans and record it with a 2D Pilatus detector it was possible to perform single grain analysis and investigate the evolution of rocking curves of one single grain during the whole fatigue process.
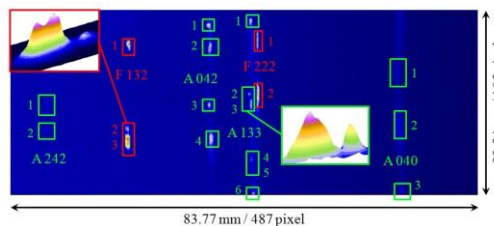
Fig.2 Summed up diffraction pattern of a whole rocking scan of a fatigued duplex stainless steel sample [1].

A summed up diffraction pattern of one whole rocking scan is shown in Fig. 2. There you can see single peaks from single grains arranged on rings, due to the relative large amount of illuminated grains (around 100 simultaneously).

In Fig. 3a) the evolution of the rocking curve of an Austenite 042 reflection is shown. There you can see that Peak 2 is increasing during the fatigue process. That can be due to a reorientation of lattice planes like a rotation of grains or the formation of slip bands. If the area underneath these peaks is now integrated one get the integrated intensity as a function load cycles shown in Fig. 3b). First the integrated intensity of both peaks decrease maybe due to a rotation of grains. After 4 million cycles the situation changed and the integrated intensity of Peak 1 stays nearly constant, so the belonging grain is not changing anymore, while the integrated intensity of Peak 2 increases first slightly and close to final fracture rapidly. This could be due to a formation of slip bands, so most of the slip bands are formed close to failure of the sample. This behaviour was also observed at other reflections. Because of the experimental setup, we could only measure at high angles in 2θ. Therefore we developed the setup and measured again at smaller angles (Fig. 1b)). The analysis of these measurements is still under way. The next step is to increase the flux at the sample by installing a capillary optic at the beamline BL10.
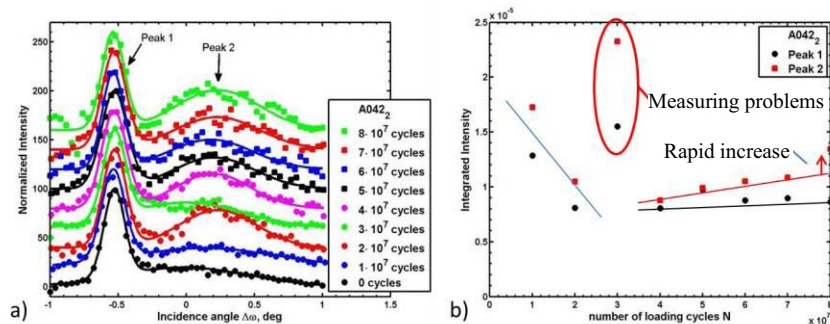
Fig.3 Evolution of a) rocking curves and b) integrated intensities as function of load cycles of an Austenite grain during fatigue process [1]

References

[1] A.K. Hüsecken, M. Söker, K. Istomin, B. Dönges, H.-J. Christ, U. Krupp and U. Pietsch: Influence of the number of fatigue cycles on the peak shape of X-ray rocking curves at duplex steel samples treated by VHCF, *Procedia Engineering* **74** (2014), 53-56.

[2] M.Söker, A.K. Hüsecken, B. Dönges, A. Giertler, U. Pietsch, C.-P. Fritzen, H.-J. Christ and U. Krupp: High and Very High Cycle Fatigue Behavior of an Austenitic-Ferritic Duplex Stainless Steel, Part 1 : Experimental Investigation, submitted to 6th International Conference on VHCF, October 15-18, 2014, Chengdu, China.

Monitoring the thermal induced crystal growth in [Nd/Pr]$_2$Fe$_{14}$B feedstock material

Sergej Schneider[1], Michael Paulus[1], Juri Nyrow[1], Christian Sternemann[1], Ralph Wagner[2], Martin Krengel[3], and Metin Tolan[1]

[1]Fakultät Physik/DELTA, TU Dortmund, 44221 Dortmund, Germany, [2]Fachbereich C-Physik, Bergische Universität Wuppertal, Gaußstr. 20, 42097 Wuppertal, Germany, [3]WILO SE, Nortkirchenstr.100, 44263 Dortmund, Germany

We report an in-situ x-ray diffraction study on the thermal induced crystal growth in the permanent magnet feedstock material [Nd/Pr]$_2$Fe$_{14}$B. This material is commonly used for the production of high strength permanent magnets, which are implemented e.g. in electric motors. Usually such magnets are produced by a process, were small polycrystalline grains are sintered at high pressure and high temperatures. However, hot pressing of partially amorphous feedstock material might be an alternative and more efficient production route. This approach should yield and oriented crystal growth and thus, anisotropic magnetic proprieties.

In order to study the thermal induced crystal growth in-situ, x-ray diffraction experiments were performed at the beamline BL10 of DELTA using a photon energy of 16 keV and the PILATUS 100k detector. The temperature treatment was applied using an Anton-Paar high temperature cell. Furthermore, ex-situ measurements were performed at BL9 at a photon energy of 27 keV. The mar345 detector was used for data aquisitation. Because of the high oxygen reactivity of the rare earth elements, the samples were heated up under constant helium flow. Starting at 20 °C the temperature was increased up to 1100 °C. A typical diffraction series is shown in figure 1. The diffraction pattern is composed of the [Nd/Pr]$_2$Fe$_{14}$B Bragg reflections, those who sharpen with rising temperature, and strong but unchanged Bragg reflections of the sample cells graphite dome (e.g at 14.5°). The crystal growth and the reduction of amorphous material was analysed by the determination of the width of the Bragg reflections and an integration of broad scattering intensity distribution below the Bragg peaks respectively. The results are shown in figure 2 and 3.
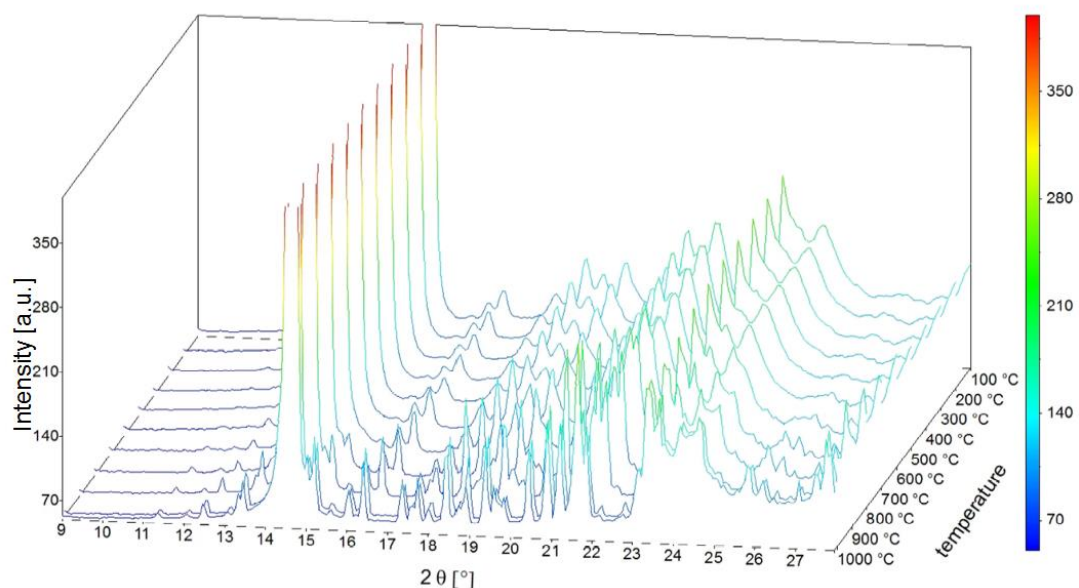
Figure 1: Temperature dependent diffraction series of [Nd/Pr]$_2$Fe$_{14}$B feedstock material.
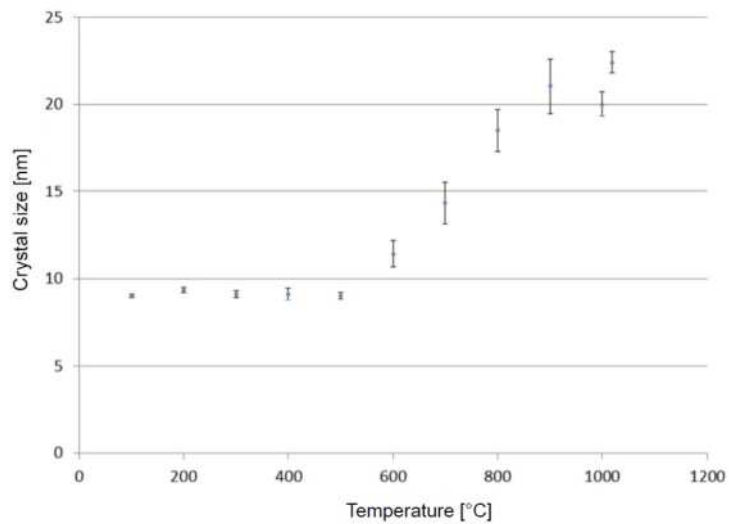
Figure 2: Temperature dependent crystal size. The size was determined using the well known Scherrer equation.
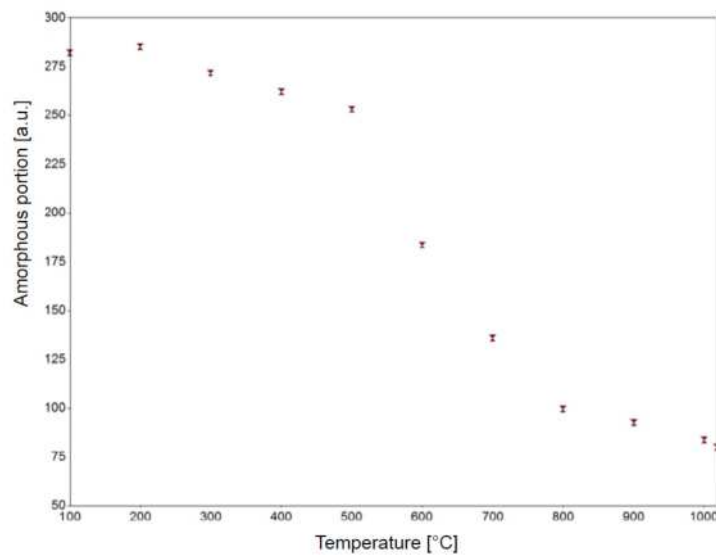
Figure 3: Reduction of the amorphous fraction within the sample.

From figure 2, it becomes obvious that the crystal growth sets in at temperatures above 500 °C, accompanied by a decrease of amorphous material. However, figure 3 shows, that a slight reduction of amorphous material is also present at lower temperatures. This behaviour might be explained by the formation of new small crystallites with sizes below 10 nm while the growth of existing crystals is still supressed at these low temperatures.

Acknowledgement

Supramolecular structure of pure and mixed monohydroxy alcohols

T. Büning, C. Sternemann, S. Bierwirth, C. Gainaru, M. Paulus, J. Bolle, R. Böhmer, M. Tolan

Fakultät Physik/DELTA, Technische Universität Dortmund, 44221 Dortmund, Germany.

Hydrogen bonds are essential for the structure of e.g. alcohols, aqueous solutions and water. They play a major role for many biophysical and biochemical processes. Monohydroxy alcohols (MAs) form supramolecular structures by aggregating their polar OH groups via hydrogen bonds. The alkyl chains of the molecules repel each other, thus depending on the position of the OH group different supramolecular structures are formed which results in different dielectrical absorption strength at ambient conditions in the mHz to GHz regime related to the so called Debye process [1]. Recent experiments show that mixing of 4-methyl-3-heptanol (4M3H) with 2-hexyl-1-decanol (2H1D) or 2-butyl-1-octanol (2B1O) leads to an up to tenfold enhancement of the dielectric absorption [2]. This is interpreted as a transition of ringlike structures in the neat MAs to chainlike structures in the mixture. Dielectric experiments are sensitive to microscopic dynamics, but a direct measurement of structural arrangements on a molecular scale is not possible with this technique. To obtain this information, wide angle x-ray scattering (WAXS) experiments were performed at the beamline BL 9 at DELTA using a MAR 345 detector.
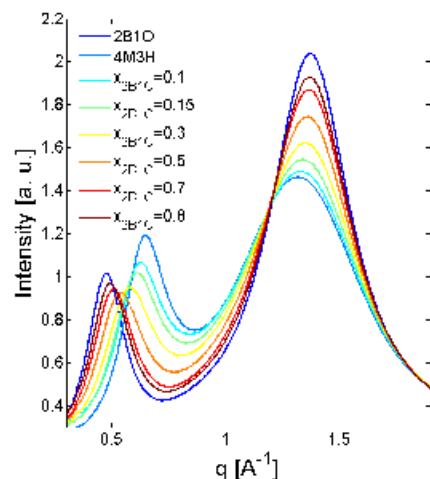
Figure 1: WAXS pattern of 2B1O, 4M3H and their mixtures.

WAXS pattern for mixtures of 2B1O and 4M3H are shown in figure 1. The observed prepeak is correlated with typical intermolecular oxygen-oxygen distances arising from a separation of supramolecular structures by the carbon chains, while the main peak is related to the intermolecular carbon distances in the liquid [3]. Mixing of 4M3H with 2B1O or 2H1D leads to a decrease of the intensity and a shift of the prepeak. The WAXS pattern of the mixture can not be expressed as a superposition of the individual contributions of the neat MAs. Both peaks shift non linearly, as displayed in figure 2, the oxygen distances are larger and the carbon distances are shorter than expected from a linear mixing behavior. This observation agrees with structural changes expected via ring to chain transformation. The outwards radiating alkyl chains
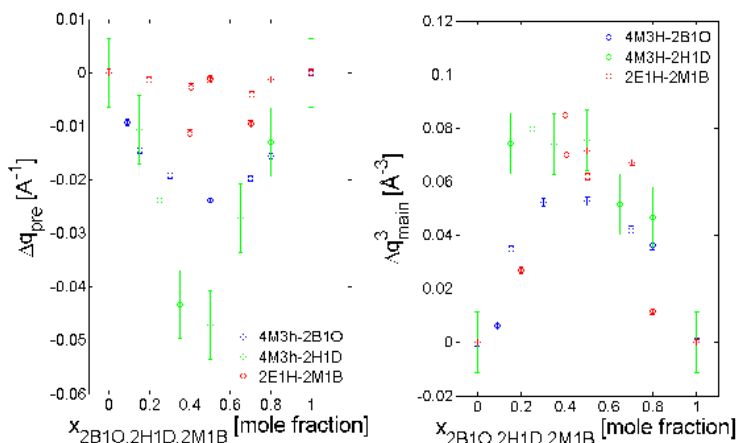
Figure 2: Deviation from linear mixing of the prepeak (Δq_{pre}) and of the microscopic density (Δq^3_{main}).

39

produce a less dense shell around their polar hydroxyl core, leading to shorter oxygen distances in ringlike than in chainlike arrangements, as shown in figure 3.

The enhancement of the dielectric Debye process is stronger in mixtures with 2H1D. A weak enhancement of ~10 % is known for mixtures of 2-ethyl-1-hexanol (2E1H) and 2-methyl-1-butanol (2M1B) [4]. Figure 2 shows that this enhancement correlates with the deviation of the prepeak behavior from linear mixing.

Because of the connection between the main peak position and the intermolecular carbon distance, q_{main}^3 correlates with the density of the liquid and Δq_{main}^3 shows the deviation of q_{main}^3 compared to a linear superposition of the neat alcohols. The mixtures are always denser than a linear variation would predict which has also been verified by macroscopic density measurement [2].
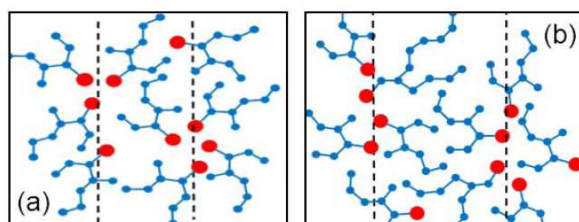
Figure 3: Schematic illustration of ringlike (a) and (b) chainlike cluster-cluster arrangements, dashed lines symbolizing typical inter-cluster distances (taken from [2]).

Up to now we have shown, that the structural origin of a dynamical phenomena can be probed with WAXS. The results would be in agreement with the picture of a structural change from ringlike to chainlike supramolecular clusters. As a next step we intended to perform inelastic x-ray scattering measurements of the oxygen K-edge which is sensitive to the local structure of the alcohol molecules and to changes in hydrogen bond configuration. These data will be compared with K-edge spectra calculated on basis of MD simulations to obtain a better understanding of the supramolecular structures.

[1] R. Böhmer, C. Gainaru, R. Richert, "Structure and dynamics of monohydroxy alcohols—milestones towards their microscopic understanding, 100 years after Debye." *Physics Reports* (2014), DOI: 10.1016/j.physrep.2014.07.005 and references theirin.
[2] S. P. Bierwirth, T. Büning, C. Gainaru, C. Sternemann, M. Tolan, R. Böhmer, "Supramolecular x-ray signature of susceptibility amplification in hydrogen-bonded liquids." PRE *preprint* (2014), DOI: 10.1103/PhysRevE.00.002800.
[3] M. Tomšič, A. Jamnik, G. Fritz-Popovski, O. Glatter, L. Vlček, "Structural properties of pure simple alcohols from ethanol, propanol, butanol, pentanol, to hexanol: comparing Monte Carlo simulations with experimental SAXS data." *The Journal of Physical Chemistry B* 111.7 (2007): 1738-1751.
[4] H. Gong, Z. Chen, D. Bi, M. Sun, Y. Tian, L. M. Wang, "Unusual Dielectric Strength of Debye Relaxation in Monohydroxy Alcohols upon Mixing." *The Journal of Physical Chemistry B* 116.37 (2012): 11482-11487.

In-situ XRD-diffraction at the diamond-metal interface in PVD coated synthetic diamonds

W. Tillmann[1,a], M. Tolan[2,b], M. Ferreira[1], S. Schneider[2] M. Paulus[2]

[1]Institute of Materials Engineering, University of Dortmund,

[2]Fakultät Physik/DELTA, TU Dortmund,
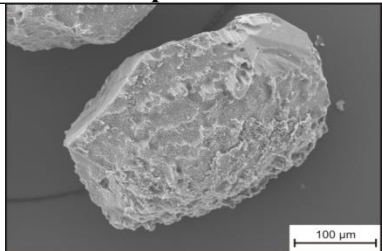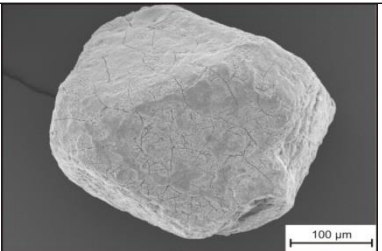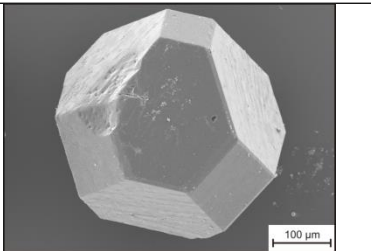
[a]wolfgang.tillmann@udo.edu, [b]Tolan@physik.uni-dortmund.de

Introduction

Powdermetallurgically fabricated diamond-metal composite materials attached to circular saws, wire saws, and drill bits are mainly used for grinding and cutting applications of high abrasive mineral materials such as natural stone or concrete. The manufacturing processes include the premixing of diamond-metal compositions, densification by mechanical uniaxial pressing, sintering in a vacuum furnace or hot-pressing [1]. Thus, the vacuum sintering procedure and hot-pressing are totally different powdermetallurgical process routes [2]. While hot-pressing is a very fast sintering method, which combines mechanical compaction and heating in one single step, vacuum sintering can only be realized in two steps: First the precompaction of the diamond-metal powder to greenbodies and second the sintering of a high amount of greenbodies in a vacuum furnace [3,4,5].

The production of these diamond-metal matrix materials and especially the used sintering procedure and parameters like the temperature and holding time have an essential influence on the materials characteristics in the final product. Besides temperature and time, the carbon reactivity of the used metalmatrix has an essential influence on the interface reactions at the diamonds. Possible interactions are shown in Table 1.

Table 1: Overview of interface reactions

Graphitization	Carbide formation	No reactions
Catalytic active elements: Fe, Ni, Co	High carbon reactive elements: Ti, Cr	No carbon solubility: Cu, CuSn

Based on this possible reactions, the effect of carbide forming PVD coatings (Ti,Cr), which have a positive influence on the diamond retention, has been investigated by in-situ xrd diffraction.

Experimental

Titanium and chromium coated diamonds were analyzed at the beamline BL9 of DELTA by using synchrotron radiation with a photon energy of E = 27 keV (λ = 0.459 Å). The XRD patterns were recorded by a MAR345 image plate detector. The distance between the samples and the detector was set as s = 342 mm. The diameter of the image plate was d = 345 mm with a pixel size of A = 100x100 μm^2. A maximum scattering angle of $2\theta_{max} = 25°$ was achieved.

Titanium coated CVD-diamonds

The following analysis of the XRD-spectra of titanium and chromium coated diamonds will mainly focus on the temperature dependent formation of metal carbides on the diamond surface. The XRD experiments on coated CVD-diamond samples were performed by in-situ phase analyses and the illustration of the important carbide and oxide reflections related to the existent temperature in the graphite furnace.
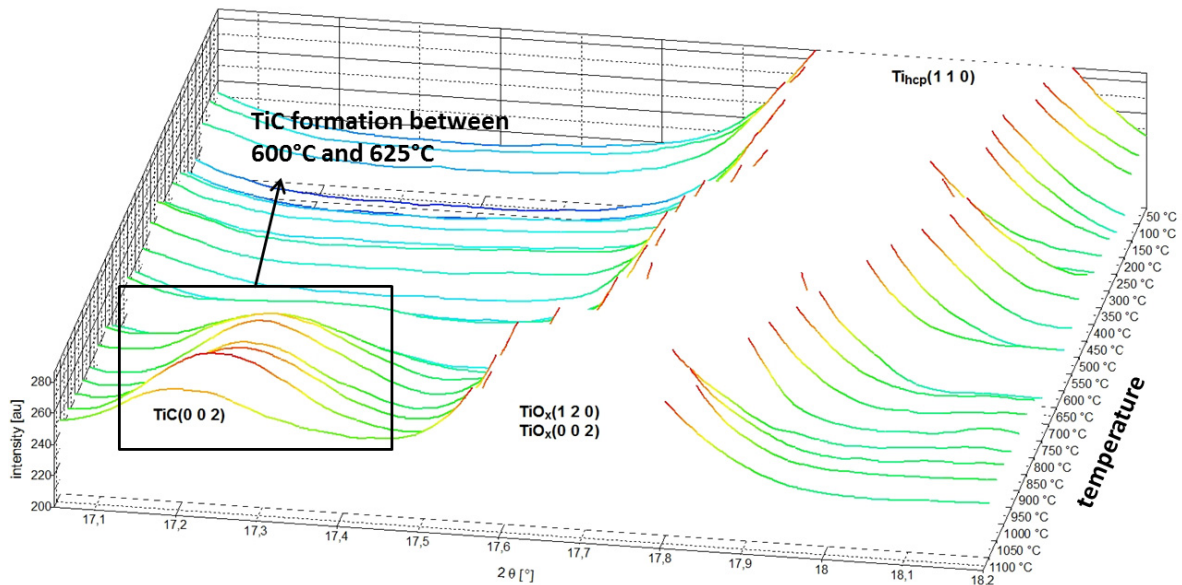
Fig. 1: In-situ XRD-spectrum of Ti-coated CVD-diamonds

Figure 1 shows the temperature dependent XRD-spectra of titanium coated CVD-diamond discs. As described in the introduction, the titanium layer on the diamond surface reacts with the diamond carbon at higher temperatures. The marked TiC peaks at 2θ=17.26° clearly identify a formation of titanium carbide at a temperature range from 600°C to 625°C. Additionally, the hexagonal titanium phase has a reflection at 2θ=17.91° at room temperature. The visible drift of this specific reflection at higher temperatures results from the increasing diffusion of carbon into the titanium lattice and the formation of a solid solution.

Acknowledgements

References

[1] Denkena B., Tönshoff H. K., Friemuth T., Gierse A., Glatzel T., Hillmann-Apmann H.: Innovative Trennschleifprozesse in der Natursteinbearbeitung, Werkstatttechnik online, Jahrgang 92, H. 6, 2002, S. 290-296

[2] J.D. Dwan: Production of Diamond Impregnated Cutting Tools, Powder Metallurgy, 1998, vol. 41, no. 2, S. 84–86

[3] Konstanty J., Bunsch A.: Hot pressing of cobalt powders, Powder Metallurgy, Vol. 34, No. 3, 1991, S. 195-198

[4] Tiziani A., et. al.: Effect of vacuum sintering on mechanical properties of stainless steel containing Cu, Powder Mettallurgy Int, Vol 22, No 4, 1990, pp. 17-19

[5] Zhang F., Yang L., Huang X.: The character of sintering under vacuum and its use in hot isostatic pressing in comparison with the air pre-sintering and slurry coating techniques for alumina-zirconia composites, Journal of Materials Processing Technology, Vol. 74, Issues 1-3, 1998, pp. 115-121

Thermal induced lattice distortion of diluted magnetic semiconductors

H. Göhring, M. Paulus, T. Büning, S. Wulle, K. Esch, C. Sternemann, M. Bayer, M. Tolan

Fakultät Physik/DELTA, Technische Universität Dortmund, 44221, Germany

Diluted magnetic semiconductors, which combine the properties of semiconductors and ferromagnets have been an important subject in materials science. Semiconductors with Curie temperatures above room temperature could revolutionize the field of spintronics by allowing control of the magnetization via application of voltage as observed e.g. for the ferromagnetic material galfenol [1]. Magnetic semiconductors, which are currently under investigation, still show a rather low Curie temperature making them inapplicable for application. However, GaMnAs seems to be a promising candidate for high Curie temperature material. GaMnAs is typically grown epitaxially on GaAs substrates with a limited manganese content of a few percent, as higher Mn contents cause the formation of Mn nanocrystals. This system was studied intensively in the past years. Starting at Curie temperatures of around 60 K, special hybrid systems containing GaMnAs show ferromagnetic behaviour up to temperatures of 200 K [2].

To understand the relation between ferromagnetic and structural properties, high resolution x-ray diffraction experiments were performed at beamline BL9 of DELTA using a photon energy of 20 keV and a helium flow cryostate setup. The PILATUS 100K detector was used for data acquisition. The sample under investigation had a Curie temperature of 60 K. The goal of our experiment was to detect structural changes due to magnetostriction passing the Curie temperature. The small changes in the GaMnAs lattice were determined by measuring both, the GaAsMn (004) and the GaAs(004) reflection of the substrate which serves as an internal reference. A first simulation of the Bragg rod and experimental data are shown in figure 1 on the left and right side, respectively.
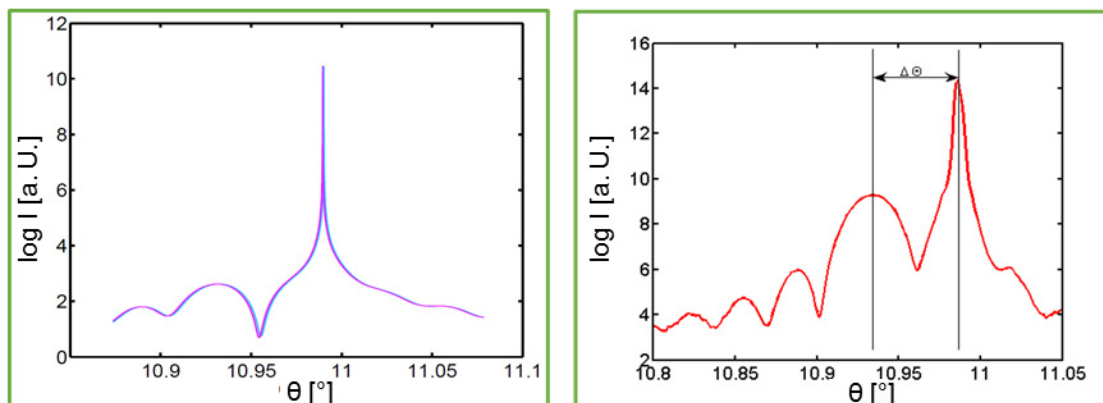
Figure 1: Left: Simulated Bragg rod of the GaAs - GaAsMn (004) reflection, right: Measured Bragg rod. The GaAsMn forms a thin film of only a few nm thickness on the GaAs surface.

To investigate the structural changes due to magnetostriction, the thermal effect on the lattice has to be separated. The separation can be achieved in a first step of the

data analysis by determining the relative changes Δθ between the GaAs and GaMnAs (004) Bragg peak positions.
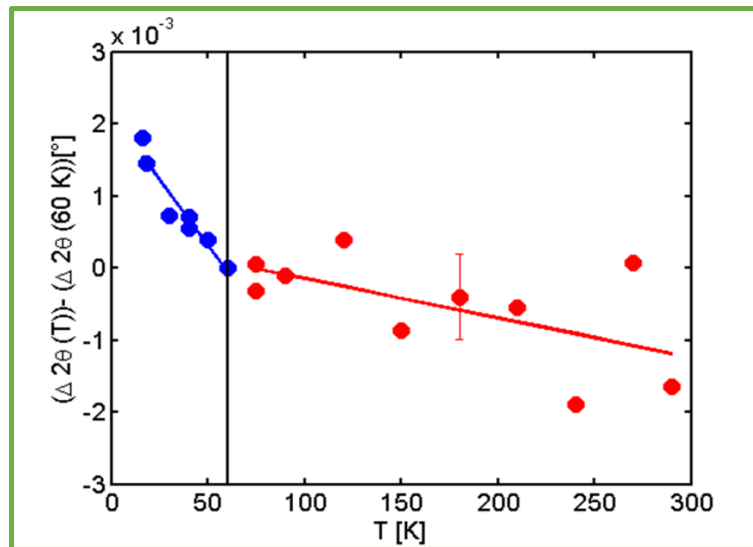
Figure 2: The angular separation between the GaAs and the GaAsMn (004) Bragg reflection. Experimental data show different slopes below (blue) and above (red) the Curie temperature.

The data presented in figure 2 show two different slopes above (red) and below (blue) the Curie temperature. This different behaviour hints on an impact of the ferromagnetic order on the lattice of GaMnAs. However, the data analysis is still in progress.

Reference:

[1] D. E. Parkes, S. A. Cavill, A. T. Hindmarch, P. Wadley, F. McGee, C. R. Staddon, K. W. Edmonds, R. P. Campion, B. L. Gallagher and A. W. Rushforth, *Non-volatile voltage control of magnetization and magnetic domain walls in magnetostrictive epitaxial thin films*, Appl. Phys. Lett. **101**, 072402 (2012).

[2] A. M. Nazmul, T. Amemiya, Y. Shuto, S. Sugahara and M. Tanaka, *High temperature ferromagnetism in GaAs-based heterostructures with Mn delta doping*, Phys. Rev. Lett. **95**, 017201 (2005).

Acknowledgement

Werkstoffe der Mikrotechnik, Institut für Werkstoffe, Fakultät Maschinenbau

Ruhr-Universität Bochum, D-44801 Bochum

Influence of dealloying temperature on the growth of WO₃ nanostructures

C. Khare
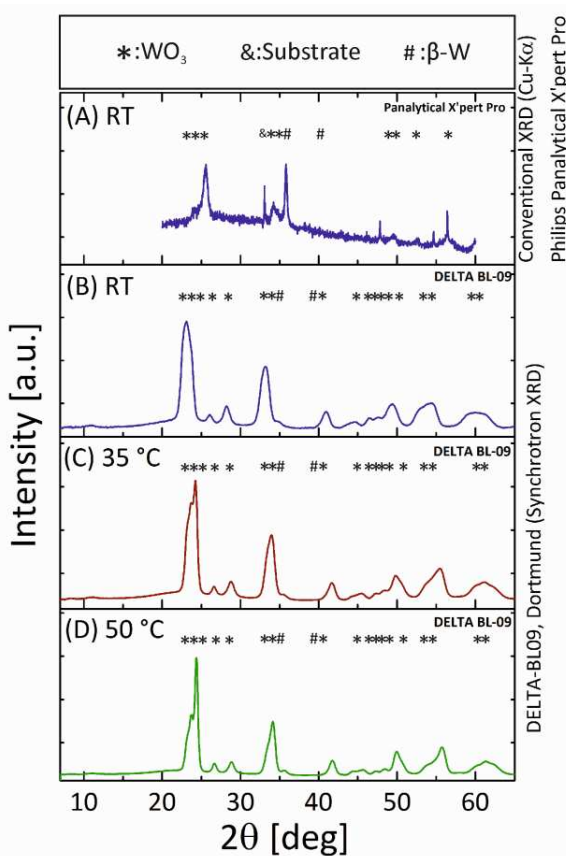
Dealloying of glancing angle deposited W-Fe nanocolumns results in formation of WO_3 nanostructures [1]. At room temperature the dealloying process, which is performed in acidic solution, continues gradually with dissolution of the less noble Fe. The process can be expedited by dealloying the precursor thin films at elevated temperatures. The synchrotron XRD analysis at Beamline 09 was performed at a grazing incidence angle with a beam energy of 20 keV using a MAR345 detector. It gave thorough structural insight for RT-, 35°C- and 50°C-dealloyed films. Figure 1 (B-D) shows several WO_3 peaks which were only detectable due to high resolution of synchrotron measurements. A significant number of peaks were attributed to monoclinic WO_3 nanostructures. Specifically, low angle peaks can be clearly identified confirming polycrystalline phase of the thin film. The effect of the dealloying temperature could be systematically explained based on these findings with complementary conventional XRD, TEM and SEM analyses. The fabricated WO_3 nanostructures offer promising applications in electrochemical solar water splitting.

Figure 1: Diffraction patterns of W-Fe nanocolumns that were dealloyed at RT (a) and (b), at 35°C (c) and at 50°C (d).

LiMn₂O₄ GLAD thin films for Li-ion battery electrodes

S. Borhani Haghighi

An important issue in the development of Li-ion batteries is the achievement of higher energy densities which in turn are dependent on the cells voltage and capacity. Therefore research on cathode and anode electrode materials is driven by the demand for lighter and thinner batteries

with higher capacities. The advantages of thin film electrodes over their composite counterparts is that they provide a better understanding of the interfacial reactions as they are free from conductive binders and impurities [2, 3]. The spinel cathode material $LiMn_2O_4$ is an isotropic material with a three dimensional network for Li-ion diffusion. It is interesting for Li-ion batteries as it allows reversible insertion and extraction of Li^+ without altering the Mn_2O_4 framework [4].

Conventional XRD was used along with synchrotron radiation based diffraction using the MAR345 detector at DELTA Beamline 09 to investigate the crystal structure of air-annealed $LiMn_2O_4$. The beam energy was set to 20 keV. Due to the grazing incidence setup used at Beamline 09, no substrate peaks are present in the respective diffraction patterns (Figure 2) allowing for better structural characterization of the thin films. From the diffraction patterns of the $LiMn_2O_4$ the presence of the spinel phase with Fd-3m space-group was identified. The diffraction peaks for (331) and (440) are not identifiable in the diffraction patterns obtained by conventional X-ray diffraction. Traces of the Mn_3O_4 were also only visible in the spectra measured at DELTA (as indicated by * in the pattern). A high intensity peak correlated to the (111) crystal plane of the Fd-3m spinel structure at $2\theta \approx 18.6°$ suggests that strongly textured films are formed. The broad hump observed in the 2θ range of 15° to 30° in all diffraction patterns might correspond to the background coming from the amorphous SiO_2 diffusion barrier layer. The spectra lines corresponding to the spinel $LiMn_2O_4$ are similar to that of the target material.
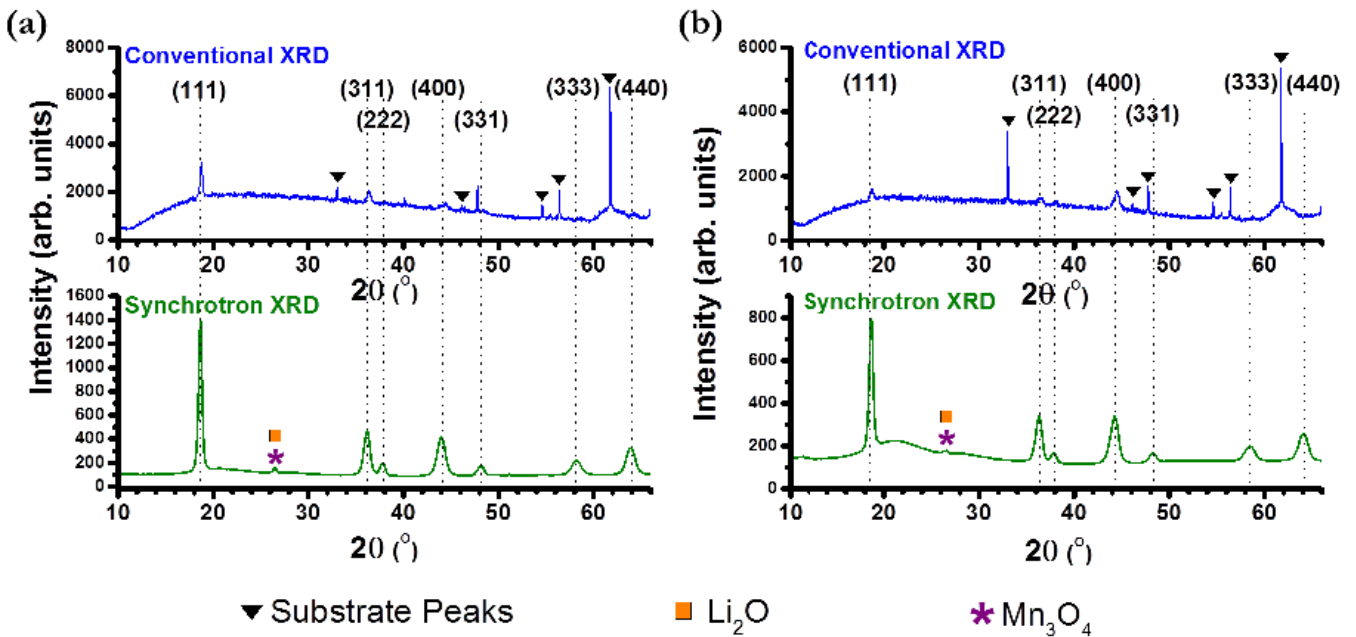
Figure 2: Conventional X-ray diffraction and synchrotron radiation of air-annealed (a) reference 600 nm and (b) 300 nm GLAD $LiMn_2O_4$ films on Pt/Ti/SiO_2/Si substrate.

Synchrotron radiation diffraction experiments of GLAD (300 nm) and reference (600 nm) Li-Mn-O films confirmed formation of a polycrystalline spinel $LiMn_2O_4$ films. Small amounts of Li_2O and/or Mn_3O_4 phase were also detected as shown in figure 2. Both films are textured along the (111) planes. A small hump is detected in the 2θ range of approximately 20.5° to 24°, which could indicate that there is small portion of the GLAD 300 nm film which is not fully crystalline. The peaks marked as * in figure 2 could also originate from a Li_2MnO_3 phase as described by Moon *et al.* [5].

References

[1] C. Khare, A. Stepanovich, B. J. S. Buenconsejo, A. Ludwig; Nanotechnology 25, 205606 (2014)

[2] Iriyama, Y., et al., *Preparation of c-axis oriented thin films of LiCoO2 by pulsed laser deposition and their electrochemical properties.* Journal of Power Sources, 2001. **94**(2): p. 175-182.

[3] Hwang, B.-J., et al., *Structure, Morphology, and Electrochemical Investigation of LiMn2O4 Thin Film Cathodes Deposited by Radio Frequency Sputtering for Lithium Microbatteries.* The Journal of Physical Chemistry C, 2009. **113**(26): p. 11373-11380.

[4] Shokoohi, F.K., J.M. Tarascon, and B.J. Wilkens, *Fabrication of thin-film LiMn2O4 cathodes for rechargeable microbatteries.* Applied Physics Letters, 1991. **59**(10): p. 1260-1262.

[5] Hee-Soo Moon and J.-W. Park, *Characteristics of In-situ Annealed LiMn2O4 Thin Films for a MEMS Power System.* Journal of Korean Physical society, 2002. **41**(6): p. 872-875.

In-situ observation of stress-induced phase changes in Cobalt films on polymer substrate

V. M. Marx[1], C. Kirchlechner[1,2], S. Djaziri[1], B. Breitbach[1], C. Sternemann[3], M. Paulus[3], G. Dehm[1]

[1] Max-Planck-Institut für Eisenforschung GmbH, D-40237 Düsseldorf, Germany
[2] University of Leoben, A-8700 Leoben, Austria
[3] Technische Universität Dortmund, D-44227 Dortmund, Germany

To produce reliable flexible electronic devices such as flexible displays or sensors, it is very important to investigate and understand the mechanical behavior of the material systems consisted of thin metal films on polymer substrates. A material for thin metal films can be cobalt, which may be able to take large strains of the underlying substrate from a possible stress-induced phase transformation. In this case, a martensitic phase transition from hexagonal to face-centered cubic can be found in bulk cobalt as well as in thin cobalt films on Si substrate during heating at around 400 °C [1, 2]. Furthermore, the phase transition can also be observed in cobalt powder with a particle size of a few micrometer by applying a plastic deformation (e.g. ball milling and annealing) [3].

The aim of this work is to study if 50-2000 nm thick Co films on 50 µm thick polyimide show a stress-induced phase transition like shape memory alloys (for instance NiTi [4, 5]), and to measure the stress-thickness-dependency of the required stress levels. Synchrotron radiation is required, because the diffraction peaks of the close-packed planes of the cubic and hexagonal phases ((111)fcc and (0001)hcp) overlap in case laboratory X-ray sources due to the higher divergence [1, 2] and (2) a high intensity is required to ensure short acquisition times for in-situ measurements.

In this study, the samples were measured in transmission geometry with the $\sin^2\varphi$ method [6] during uniaxial tensile tests (Figure 1), so that approximately half of the Debye Scherer rings can be detected on the MAR345 image plate detector (Figure 2). Therefore, an Anton Paar TS600 straining device, providing a hole on the backside, was used so that a measurement in transmission without shadowing was feasible. The beam energy was 15.2 keV to ensure to radiograph also the thicker Co films with a thickness of 2 µm.
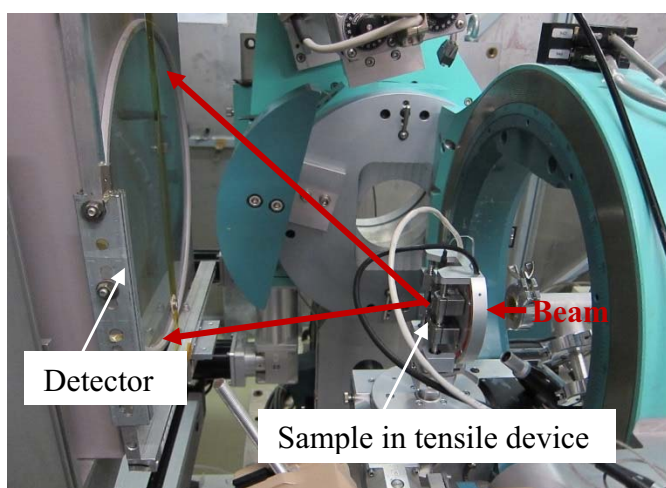
Figure 1. Setup of the Anton Paar TS600 straining device in the goniometer of BL9 to measure the Debye-Scherer rings in transmission geometry. The beam is indicated by red arrows.
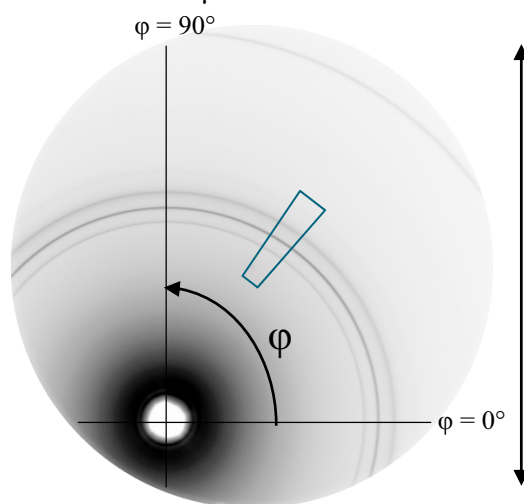
Figure 2. Measured Debye-Scherer rings. The straining direction is indicated by a double sided arrow. $\varphi = 90°$ corresponds to the longitudinal and $\varphi = 0°$ to the transverse direction.

The samples were strained stepwise, i.e. due to the long read-out time of the detector a hold of 6 min was applied after every 0.5 % strain,

during which the Debye-Scherer rings were detected. For the evaluation, the inner Debye-Scherer rings (see blue marked area in Figure 2 and Figure 3a) were integrated with the program Fit2D in 10° steps from -5° to 95° for every strain (each 0.5 %). After that, the interplanar spacing, d, was calculated for each peak and each strain individually and plotted against the $\sin^2\varphi$ values so that a linear fit could be applied (Figure 3b). With the slope of these linear fit one is able to calculate a film stress (for more information about the evaluation see reference [6]).
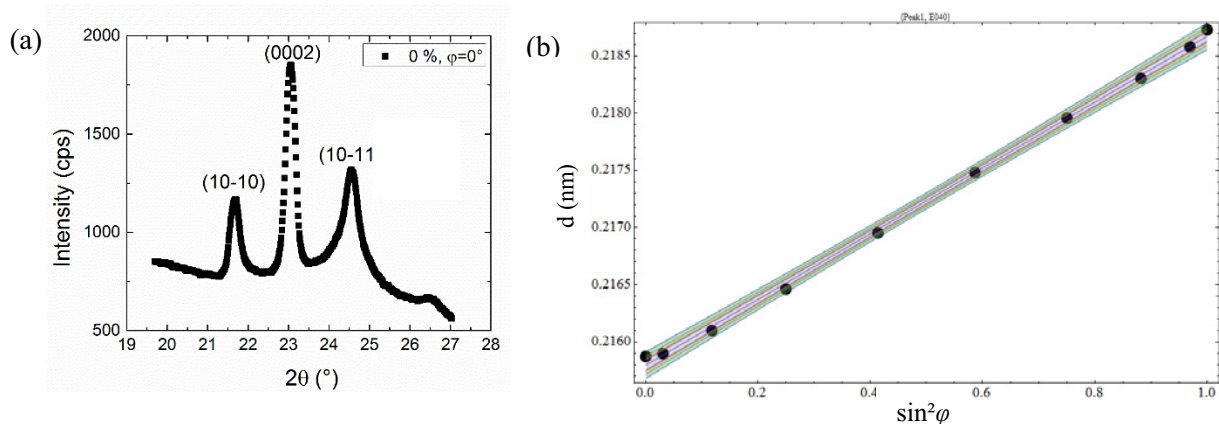
Figure 3. (a) Integrated peaks of the 2 µm thick Co film at 0 % strain and $\varphi = 0°$. (b) Plot of the interplanar spacing, d, against $\sin^2\varphi$ of the first peak from the 2 µm thick Co film at 4 % strain.
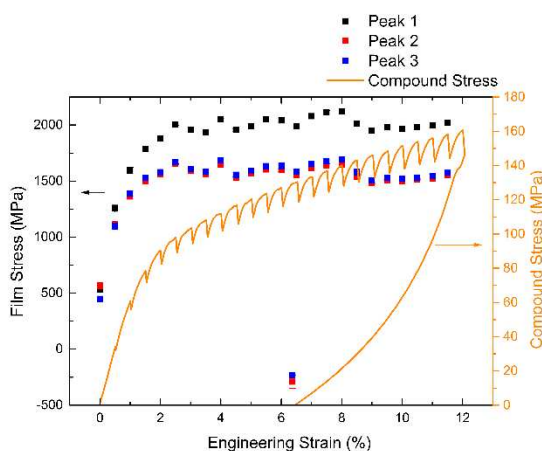
Figure 4. Plot of the film stresses evaluated from three different peaks and the compound stress against the engineering strain for the 2µm thick Co film. The role of texture, grain-grain interaction and anisotropy has been neglected for the stress analysis, which explains the observed discrepancy.

Figure 4 shows exemplarily the film stresses for the three different peaks evaluated with the $\sin^2\varphi$ method as well as the compound stress (film + substrate) against the engineering strain measured with the tensile device. The drops in the compound stresses indicate the stress relaxation due to the 6 min hold for detecting the Debye-Scherer rings.

In summary, by comparing the integrated peaks at different strains, no phase transformation is observable. A solution can be annealing of the samples at around 400°C before the tensile test as well as during the tensile test to induce the phase change. Further experiments with heating the samples are in progress. However, the internal stresses in the films could be successfully evaluated during stepwise straining of the samples.

References:

[1]   Hesemann HT, Müllner P, Arzt E. Scr. Mater. 2001;44:25.
[2]   Hesemann HT, Müllner P, Kraft O, Nowak D, Baker SP, Finkelstein K, Arzt E. Scr. Mater. 2003;48:1129.
[3]   Cardellini F, Mazzone G. Phil. Mag. A 1993;67:1289.
[4]   Frick CP, Lang TW, Spark K, Gall K. Acta Mater. 2006;54:2223.
[5]   Ng KL, Sun QP. Mech. Mater. 2006;38:41.
[6]   Wanner A, Dunand DC. Metall. Mater. Trans. A 2000;31:2949.

Structural and electrical characterization of Poly(3-hexylthiophene) based bulk heterojunction thin films.

C. Kwamen, L. Grodd, E. Mikayelyan, S. Grigorian.

Conjugated polymer-based photovoltaics have become the subject of intense research as they have displayed significant potential for competition with conventional inorganic-based solar cells. Understanding their microstructure development will enable control and optimization of cell morphology [1].

The grazing incidence x-ray diffraction (GIXD) experiment was realized on as-casted blends of poly(3-hexylthiophene) (P3HT) with fullerenes : [6,6]-phenyl-C_{60} butyric acid methyl ester (PCBM) on one side and Indene-C_{60} bisadduct (ICBA) on the other using different blending ratios. Their chemical structures are shown in figure 1.

Figure 1: Chemical structures of P3HT, PCBM, and ICBA.

It was found that the crystallinity of P3HT can be affected by the relative amount of fullerene molecules in the blends. For example P3HT: PCBM and P3HT:ICBA blends of various ratios 1 : 0.5, 1 : 0.8, 1:1 and 1 : 2 exhibit differing morphological organizations (figure 2). On increasing the fullerene content in the blend, the P3HT interchain pi–pi stacking disappear progressively. This indicates that excess fullerene impedes on the pi–pi stacking of P3HT molecules.
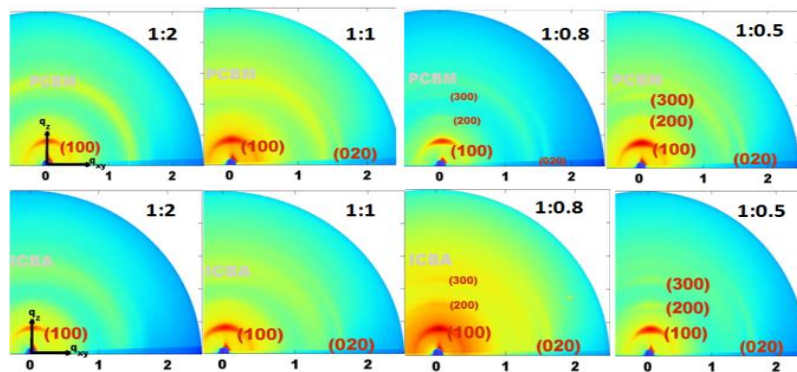
Figure 2: 2D GIXD pattern obtained for P3HT:PCBM (first row) and P3HT:ICBA (second row) blend films.

Taking a close look at P3HT:PCBM and P3HT:ICBA films with same blending ratio (figure 3), the crystallinity of the polymer did not appear to be significantly affected by the difference in acceptors unlike their respective film morphology and fullerene domains. The latter reveal smaller domain size for ICBA (~2nm) with respect to PCBM (~4nm), when blended with P3HT. These results are in accordance with that reported by Y.-H. Lin et al. who already suggested the stronger tendency of PCBM form larger domains than ICBA in either pure or blend films [2].
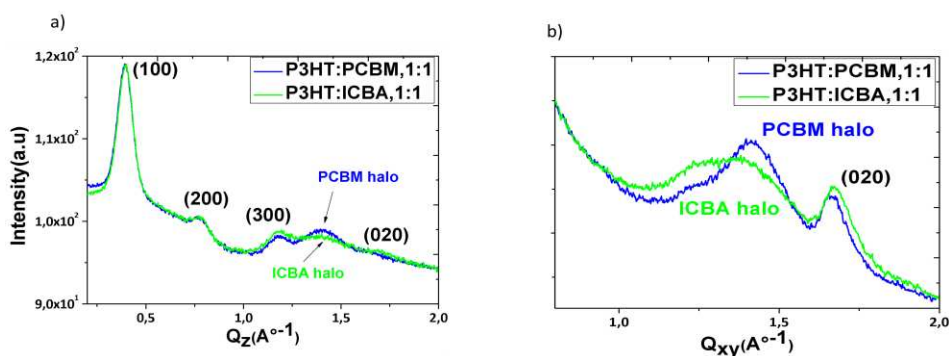
Figure 3: (a) out-of plane (b)in plane line profiles of P3HT:PCBM and P3HT:ICBA 1:1 w:w blend films.

The second part of the study aimed at correlating the structural and electrical properties of the two systems during solvent evaporation by casting from solution (1:1 w:w) under applied constant voltage (10V). The evolution of current and P3HT (100) Bragg peak intensity is shown in figure 4; with a two slope increase in structure and current for the PCBM-based film. No delay was observed between structure and current maxima for both blends. This is not the case for pristine P3HT thin film for which the current reaches its maximum before complete drying [3].
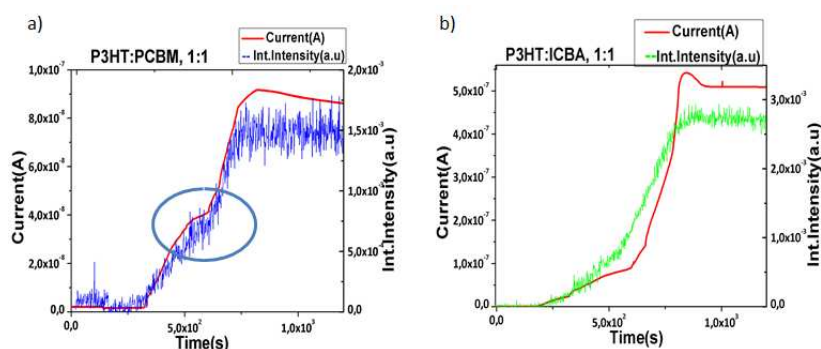
Figure 4: Time dependence of current (red curve) and integrated (100) peak intensity of P3HT in a) (blue curve) P3HT:PCBM film and b) (green curve) P3HT:ICBA film during solidification.

The current evolution is identical to that of the structure development for PCBM-based film; whereas for ICBA case, there is a delay in such response. During solidification, current slope is higher than that of structure in the ICBA-based film (see red and green curves in figure 4(b)). This confirms a higher charge carrier transfer and better incorporation of ICBA into polymer matrix already suggested by the GIXD experiment. Interestingly, for the final solid state, current appears to be higher for the film with ICBA, indicating a higher electrical conductivity for P3HT:ICBA blend film. Thus, the reported higher efficiency of ICBA-based cells can be justified by its higher miscibility with P3HT, and also higher electrical conductivity.

Literature

[1] Eric Verploegen, Chad E. Miller, Kristin Schmidt, Zhenan Bao, and Michael F. Toney. Chem. Mater. 2012, 24, 3923−3931. dx.doi.org/10.1021/cm302312a

[2] You-Heng Lin, Yu-Tang Tsai, Chung-Chih Wu , Chih-Hung Tsai, Chien-Hung Chiang, Hsiu-Fu Hsu, Jey-Jau Lee, Ching-Yuan Cheng. Organic Electronics, Volume 13, Issue 11, November 2012, Pages 2333–2341. DOI: 10.1016/j.orgel.2012.07.023

[3] L.Grodd, U.Pietsch, S.Grigorian. Macromol.Rapid commun. 2012, DOI: 10.1002/marc.201200309

Investigation of phase formation in Iron-Carbon-Boron (Fe-C-B) alloys - Experimental report DELTA beamline 9

Jonathan Lentz[I], Ruben Schneider[I], Arne Röttger[I]

[I]Ruhr-Universität Bochum, Institut für Werkstoffe, Lehrstuhl Werkstofftechnik, Universitätsstraße 150, D-44801 Bochum, Germany

Tool steels are used to machine and process metallic and mineral materials. Therefore, tool steels possess high hardness, high wear resistance and a sufficient toughness, simultaneously. The combination of these often counteracting requirements brings out the challenge of an alloy development in this field. In this context, iron-carbon-boron alloys (Fe-C-B) exhibits the opportunity fulfill the tribo-mechanical requirements. Due to the strong hard phase forming ability of the element boron, hardness as well as wear resistance of boron alloyed steels can be improved, significantly. However, research has to be performed in the basic alloying system Fe-C-B, which is controversially described and discussed in the literature. Furthermore, the effect of the alloying elements Cr, Mn, Si, V and Mo on the system Fe-C-B has to be investigated and fully understood to utilize the element B in tool steels. Computational techniques like the CALPHAD- and the multi-phase-field-method (MPF) make it possible to simulate and to reproduce the phase formation of complex alloying systems. Modern alloy development takes advantage of these techniques to reduce the experimental effort, to accelerate the development and to gain insight into microstructural processes. However the performance of these computational approaches is limited to the thermodynamic material databases and simplifying constraints they rely on. Consequently, these simulations have to be experimentally validated. The objective of the experiments that were performed at DELTA's beamline 9 was the validation of simulations performed for the alloying systems Fe-C-B and Fe-C-B-X (where X was Si, Mn, Cr or Mo). Therefore 5 different series of laboratory melts were manufactured and metallographically analyzed. Thereby, the alloying content of the respective elements (B, Si, Mn, Cr, Mo) was stepwise increased. The C-content was kept constant at 0.6 mass%. The high energetic X-ray radiation provided by beamline 9 was used to perform diffraction experiments and thus determine the crystallography of the phases that were present in the laboratory melts. Experimental series were performed for specimens at "ex-situ" and "in-situ" conditions. The specimens for "ex-situ" conditions were heat treated at 700, 800, 900 and 1000 °C for 288h and quenched to approximate and freeze the thermodynamic equilibrium condition at the corresponding temperature. The measurements at "in-situ" conditions were performed at elevated temperatures to analyze the kinetics of phase formation. One main result of this investigation is that the performed thermodynamic calculations fit well with the reality, which was verified by synchrotron radiation experiments. Figure 1 shows an excerpt of the ex-situ measurements that were used to validate the calculated phase diagram presented in figure 2.
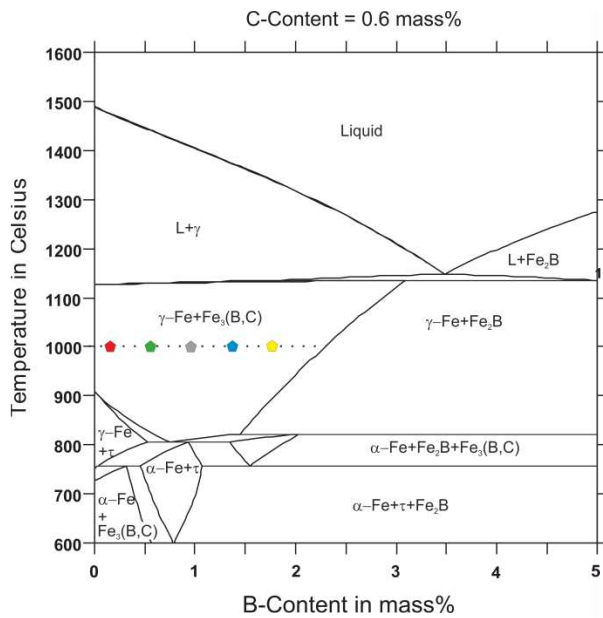
Figure 2: Quasi binary phase diagram. colored points are indicating laboratory melts' composition

Until now the results are part of the following thesis and publications:

GEFÜGEAUSBILDUNG UND MIKROMECHANISCHE EIGENSCHAFTEN EINZELNER PHASEN VON UNTEREUTEKTISCHEN FE-C-B LEGIERUNGEN -J. Lentz, A. Röttger, W. Theisen - Prakt. Met. Sonderband 46 (2014), Frank Mücklich, Günter Petzow (Hrsg.): Fortschritte in der Metallographie: Berichte der 14. Internationalen Metallographie-Tagung Leoben,. 2014, pg. 283-288.. - ISBN 978-3-88355-403-7

Charakterisierung des Erstarrungsverhaltens untereutektischer Stähle im ternären System Fe-C-B –master thesis, Jonathan Lentz, Februar 2014

Further publications and student works that evaluate the results are going to be completed soon.
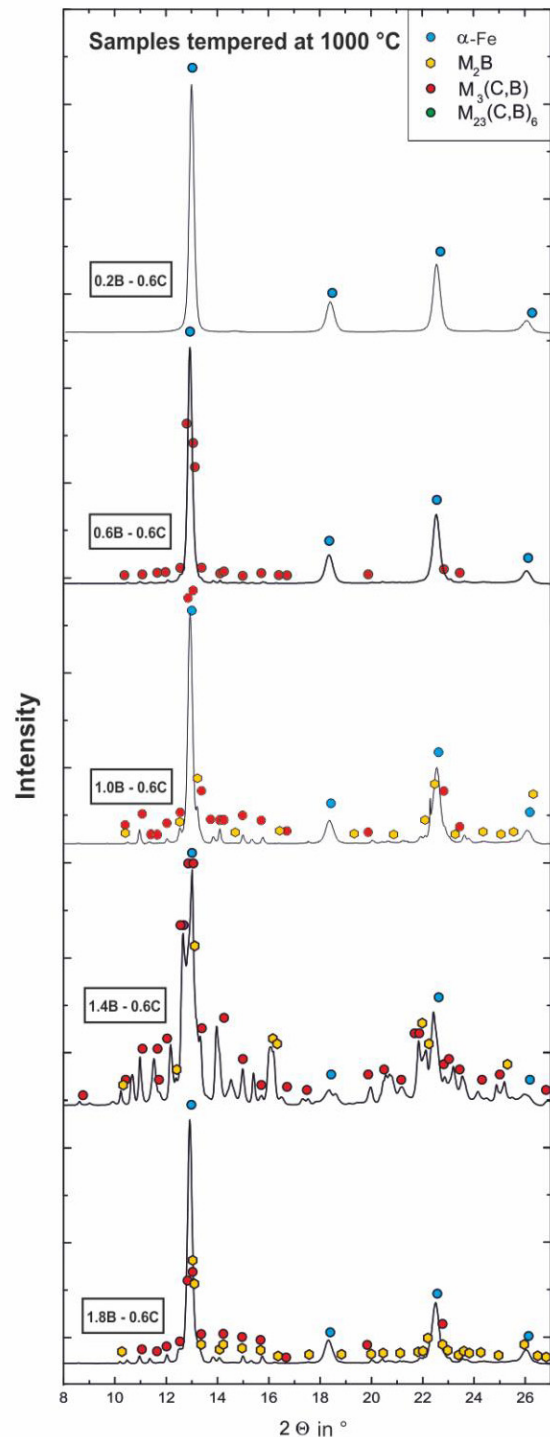
Figure 1: **D**iffractograms **measured at Beamline 9**

In-situ recrystallization of thiophene based oligomer films

Eduard Mikayelyan, Linda Grodd, Christelle Kwamen, Souren Grigorian

Organic semiconductors are attractive for electronics due to the low cost processing methods and their high electrical conductivity. Conjugated semiconductors (polymers and oligomers) are providing relatively high field effect mobility. Novel thiophene based oligomer α,α'-dihexylquinquethiophene (D5HT)[1,2] system (see inset fig. 1, left) was under investigation. These oligomers are promising material for utilizing in organic field effect transistors (OFETs).[3] Our intention is to tailor the structure of the film by means of recrystallization.

The improvement of the crystallinity is even possible after initial casting by reorganization (temperature treatment, solvent vapour annealing, etc.), however, this process is much slower than the initial growth. In contrast to polymers for the small molecules transition from one form to another is taking place in very sharp temperature range and for this reason high time resolution experiment using synchrotron radiation high intense x-ray beam is necessary. Because many properties are dependent on the structure and crystallization of the material, it is of interest to understand the dependence of electrical properties on structure. The overall intention is to optimize the molecular organization of thin films with enhanced electrical properties for organic electronics.

Phase transition for the drop cast DH5T films was found by in-situ grazing incidence x-ray diffraction (GIXD) experiment performed at BL9 beamline, DELTA. During the experiment the film was heated to 250°C and then cooled down to room temperature (fig. 1, right) while only the most intense out-of-plane reflection (see Fig. 1, left) was measured which is associated to the direction of the molecule stem. From this experiment it was observed a phase transition where during a first step the shrinking of the crystal structure was observed by corresponding change of the peak position from 0.19 to 0.21Å^{-1} in reciprocal space. Further heating initiated the abrupt expansion with jump of peak position from 0.21 to 0.11Å^{-1}.

The evolution of out-of-plane line profile
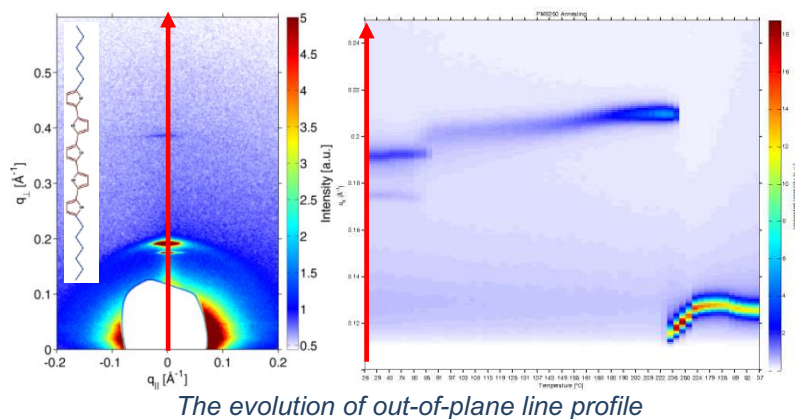
Figure 1: Grazing incidence x-ray diffraction experiment results of the DH5T recrystallization.

The alkyl side chain substitutions can affect the molecular organization during the thermal treatment they can stabilize and destabilise the crystal domains.[1] It was found different phases during the temperature treatment for hexyl substituted quaterthiophene (4T) however, for the reflections associated to molecular length abrupt jump to small or higher q was not observed[1]. In the experiment initially the reflection at $q_z = 0.19$Å^{-1} (corresponding to a distance of one molecule length) at the higher temperature of 250°C was modified to a new position of about 0.11Å^{-1} (expansion up to 1.5 times of initial distance). Further

investigations will be done to obtain the full structure of the crystal system at all stages of the phase transition and correlated to electrical performance to reveal the structure associated to high charge transport.

Literature

(1)   Anokhin, D. V.; Defaux, M.; Mourran, A.; Moeller, M.; Luponosov, Y. N.; Borshchev, O. V.; Bakirov, A. V.; Shcherbina, M. A.; Chvalun, S. N.; Meyer-Friedrichsen, T.; Elschner, A.; Kirchmeyer, S.; Ponomarenko, S. A.; Ivanov, D. A.: Effect of Molecular Structure of alpha,alpha '-Dialkylquaterthiophenes and Their Organosilicon Multipods on Ordering, Phase Behavior, and Charge Carrier Mobility. J Phys Chem C **2012**, 116, 22727-22736.

(2)   Sizov, A. S.; Agina, E. V.; Gholamrezaie, F.; Bruevich, V. V.; Borshchev, O. V.; Paraschuk, D. Y.; de Leeuw, D. M.; Ponomarenko, S. A.: Oligothiophene-based monolayer field-effect transistors prepared by Langmuir-Blodgett technique. Appl Phys Lett **2013**, 103.

(3)   Agina, E. V.; Usov, I. A.; Borshchev, O. V.; Wang, J. B.; Mourran, A.; Shcherbina, M. A.; Bakirov, A. V.; Grigorian, S.; Moller, M.; Chvalun, S. N.; Ponomarenko, S. A.: Formation of Self-Assembled Organosilicon-Functionalized Quinquethiophene Monolayers by Fast Processing Techniques. Langmuir **2012**, 28, 16186-16195.

Analysis of crystal structure of highly crystalline thin polymer films

Zahra Molla, Tungalag Naran and Ullrich Pietsch

Festkörperphysik, Universität Siegen.

According to a shared project between BASF Company and University Siegen, we had to determine the crystal structure of new oligomer molecules with exceptionally high electric mobility prepared as thin films. By our last beamtime at **BL9 of Delta in May 2014**, the first experimental 2D GISAXS pattern of the new polymer has been recorded using PILATUS detector und although detailed information about the chemical nature of the molecules are secret but these preliminary data revealed certain similarities with the molecule PDI8-CN2 which has been investigated previously at DELTA [master thesis of Yun Gu 2010]. The 2D GISAXS pattern exhibited a large number of Bragg spots arranged along q_z and q_x (Fig.1). Based on these data the crystalline structure of this new polymer has been determined. All peaks could be indexed considering monoclinic crystal structure with oblique 2D lattice parallel the surface. The structure contains two molecular layers where each molecule is tilted by a small angle with respect to the surface normal. The polymer film is composed by nanocrystals. They are stacked along the surface normal but show random orientation in azimuth direction. .

(a)   **(b)**
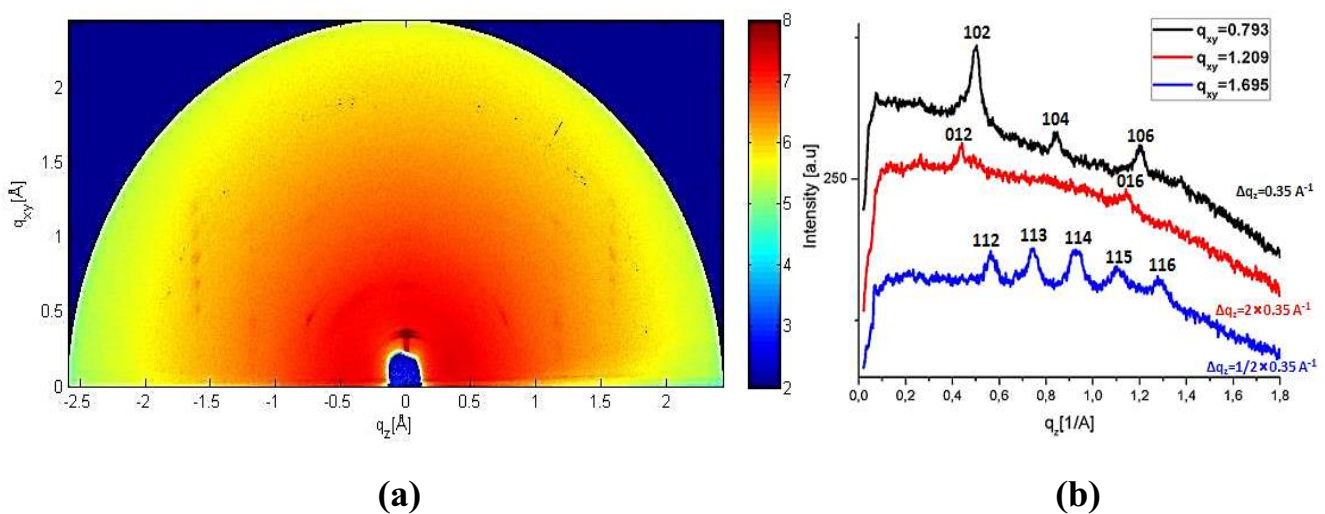
Fig.1 (a) Shows the first two-dimensional GIWAXS plots of the new polymer taken at BL9 of DELTA; **(b)** Vertical linecuts of the films, q_z is the perpendicular wave vector transfer with respect to substrate surface.

In-situ XRD(T) analysis of Ti-Ta high-temperature shape memory alloy thin films sputter deposited at room temperature

Y. Motemani, A. Lange

Werkstoffe der Mikrotechnik, Institut für Werkstoffe, Fakultät Maschinenbau

Ruhr-Universität Bochum, D-44801 Bochum

Ti-Ta based alloys are promising materials for actuators operating above 100°C [1, 2]. In these alloys the shape memory effect, i.e. the actuation response, occurs by a martensitic phase transformation between the parent phase (ß, body centered cubic) and the martensite phase (α´´, orthorhombic) [1]. The aim of our study was to observe the phase transformation (from ß to α´´ and vice versa) and also an expected aging effect in Ti-Ta binary alloys by in-situ XRD analysis at DELTA. In this study, we investigated a Ti-33 at.% Ta thin film (4 µm in thickness) as well as a Ti-33 at.% Ta bulk alloy. For these analyses, BL 09 was equipped with an Anton Paar DHS 1100 hot stage and a Pilatus 100 K detector. The beam energy was set to 20 keV. The samples were heated at a heating rate of approximately 50 K min^{-1}. The XRD patterns were recorded at certain temperature intervals. The holding time at each temperature was approximately 30 s, and the exposure time to detect the diffracted x-rays during the actual measurement was only 4 s to avoid aging of the samples especially at high temperatures.

Figure 1 (a) clearly shows the transformation from the martensite (α´´) to the austenite (ß) during heating in the bulk sample. The (022) and (200) Bragg diffraction peaks correspond to α´´, whereas (200) peak corresponds to the ß phase. From the stacking of the patterns it is expected that the austenite start temperature (A_s) is around 70°C and the austenite finish temperature (A_f) is around 200°C. From the cooling cycle (Figure 1 (b)) the martensite start temperature (M_s) is expected to be around 170°C and the martensite finish temperature (M_f) is expected to be around 65°C.
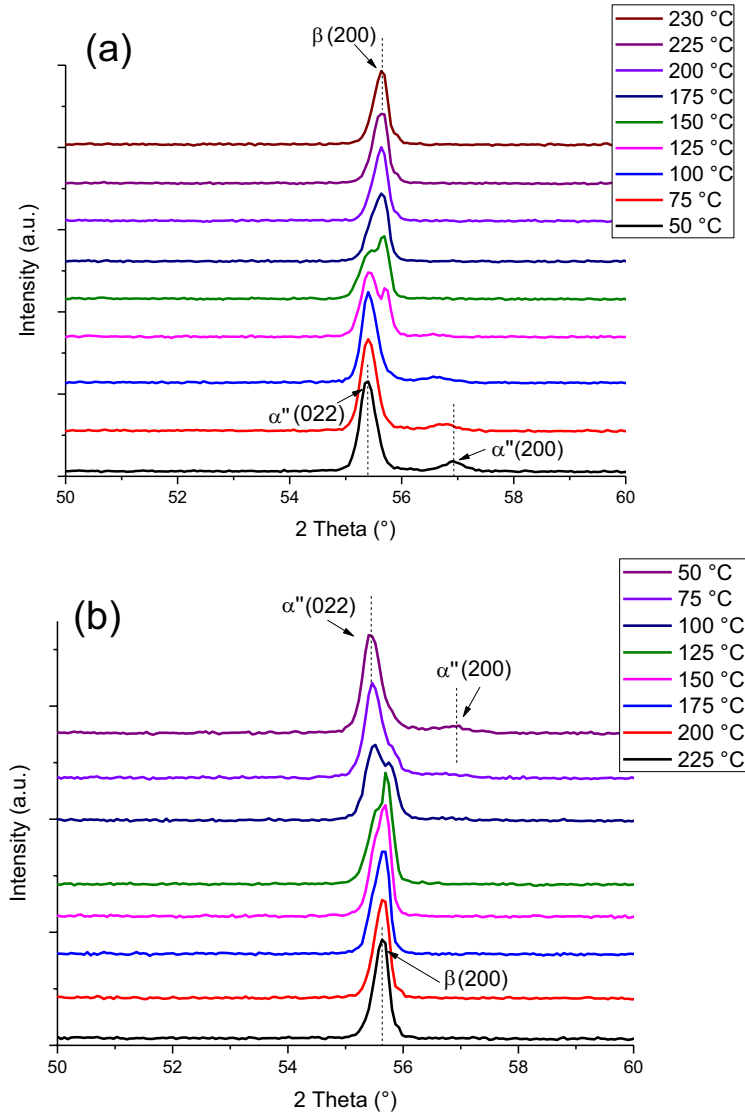
Figure 1: Ti-33Ta (at.%) Bulk – (a) Heating cycle ($A_s \sim 70°C$, $A_f \sim 200°C$); (b) Cooling cycle ($M_s \sim 170°C$, $M_f \sim 65°C$)

Figure 2 shows the heating (a) and the cooling cycle (b) for the 4 μm thin film sample, where a clear martensitic transformation between α´´ and ß phases like that identified in the bulk sample (Figure 1) can be observed. Figure 2 (c) shows the diffraction patterns at 50°C from the heating cycle as well as the cooling cycle. The main peak (113) in figure 2 (b) becomes broader and decreases in intensity. Furthermore the (131) as well as (202) peaks decrease in intensity. It is assumed that the sample was aged at high temperatures during cycling. At high temperature it is expected that the ω phase (very small precipitates, <20 nm, with ellipsoidal morphology[3]) forms and that by cooling back to room temperature, the ß phase is retained in the sample, which leads to an overlapping of peaks at the (113) peak position and causes the observed broadening. The range of phase transformation temperatures

observed during in-situ XRD measurements agrees with those obtained from our stress measurement analyses (cantilever measurement, data not shown).
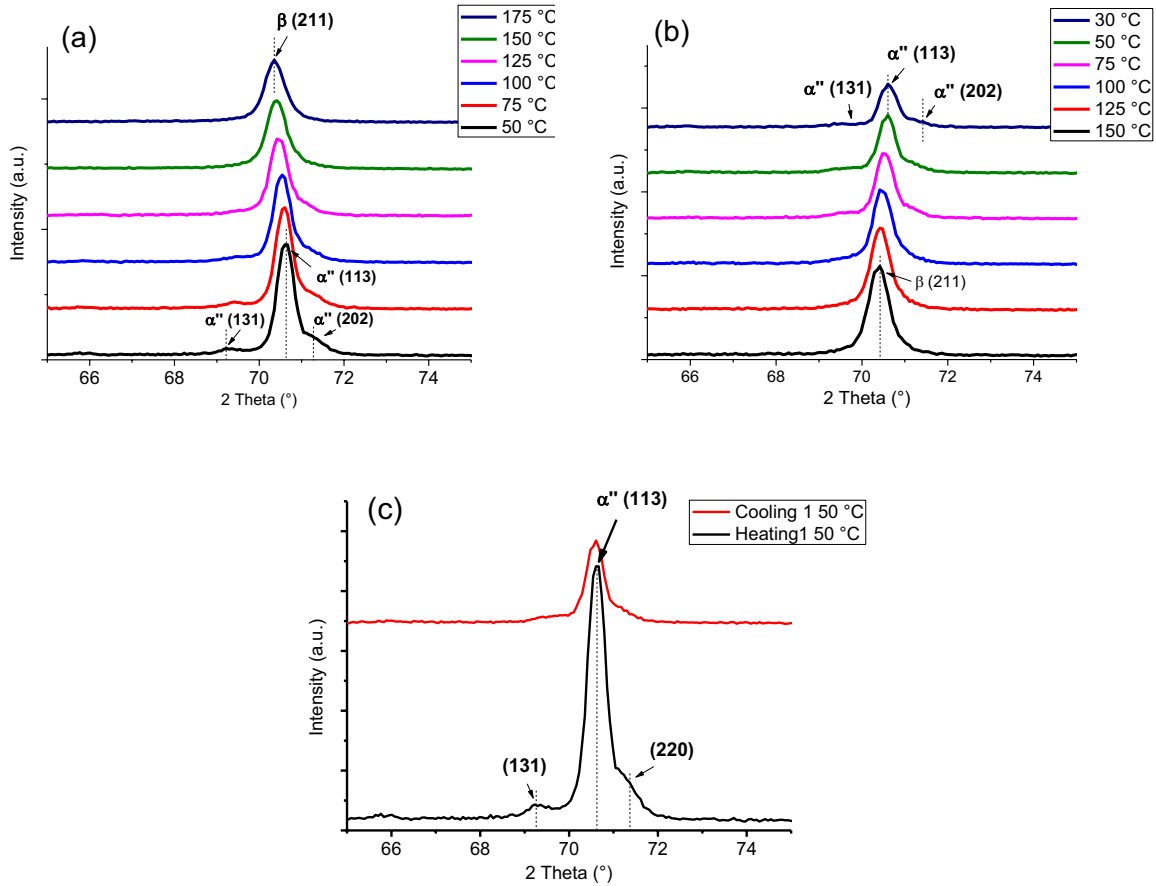
Figure 2: Ti-33Ta (at.%) 4 µm thin film – (a) Heating cycle ($A_s \sim 70°C$, $A_f \sim 170°C$); (b) Cooling cycle ($M_s \sim 130°C$, $M_f \sim 65°C$)

References

[1]   P. J. S. Buenconsejo et al, Acta Mater. **2009**, 57. 1068.

[2]   Y. Motemani et al, Adv. Mater. Inter. **2014** ,1, 1400019.

[3]   H. P. Ng et al, Acta Mater, **2011**, 2981–2991.

A high hydrostatic pressure x-ray diffraction study of vulcanized fiber and paper

Karin Esch[1], Dominik Dumke[2], Michael Paulus[1], Christian Sternemann[1], Thomas Büning[1], Julian Schulze[1], Simon Wulle[1], Sergius Janik[1], Holger Göhring[1] and Metin Tolan[1]

[1]Fakultät Physik / DELTA, Technische Universität Dortmund, D-44221 Dortmund, Germany
[2]Fakultät Maschinenbau, Technische Universität Dortmund, D-44221 Dortmund, Germany

Vulcanized fiber, consisting of cellulose, is a material of various applications, for example it is used as an insulator in electrical industry, and can be found in washers/gaskets and welding shields. As vulcanized fiber and paper are made from renewable resources, these materials gained increasing interest in the recent years.

One way to produce vulcanized fiber is parchmentising. Raw paper is soaked with a 70% $ZnCl_2$-solution, pressed to interconnect the layers, rested for a certain time, and washed out in steps of descending concentrations. Paper consists mostly of cellulose I_α [1] and I_β [2], which transforms to cellulose II [3] During this process, the material's structure changes on a molecular level. Consequently, macroscopic properties change, e.g. the material becomes harder and stiffer. The underlying structural changes can be analysed by x-ray diffraction (XRD).

Paper and vulcanized fiber were studied under high hydrostatic pressure (up to 4 kbar). The experiments were performed at beamline BL9 of DELTA [5] with a photon energy of 27 keV using a MAR345 image plate detector.
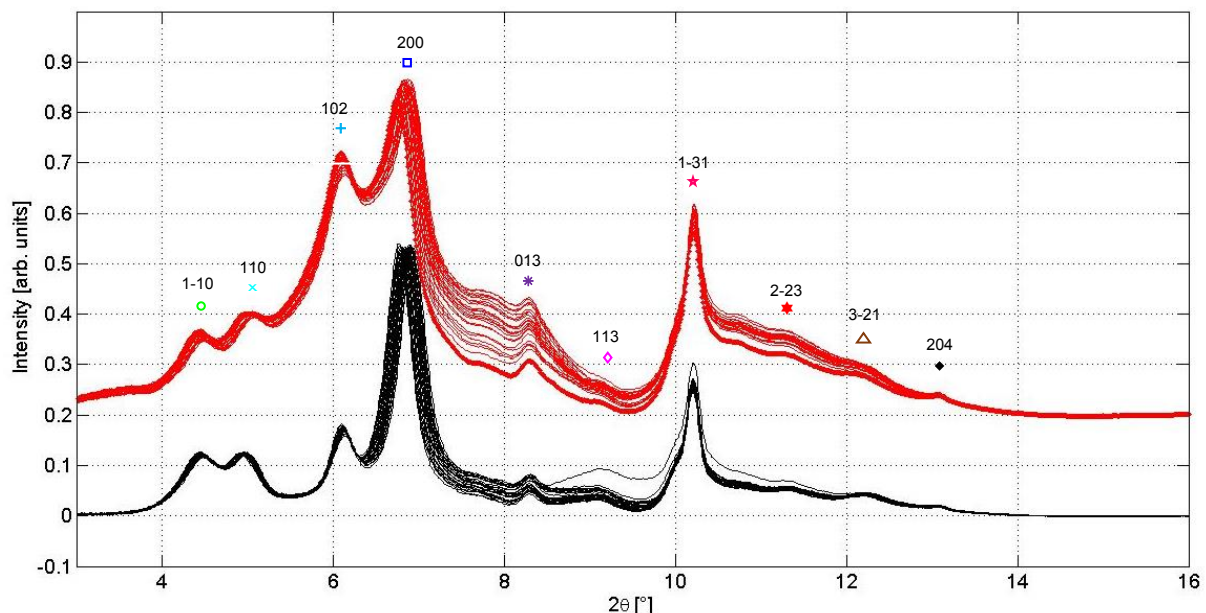
Figure 1: Diffraction patterns of paper (black) and vulcanized fiber (red) exposed to pressures between 1 bar and 4 kbar. The peaks are indexed with the miller indices of cellulose I_β.

In figure 1 the diffraction patterns of paper and vulcanized fiber under increasing and decreasing pressure between 0 and 4 kbar are shown. A shift of certain Bragg reflections can be seen, whereas other reflections hardly change. Moreover, a higher amorphous contribution in vulcanized fiber compared to paper is indicated. From the reflection positions, the interplanar distances d can be calculated. The relative interplanar distances d/d_0 are displayed in figure 2 as a function of pressure.
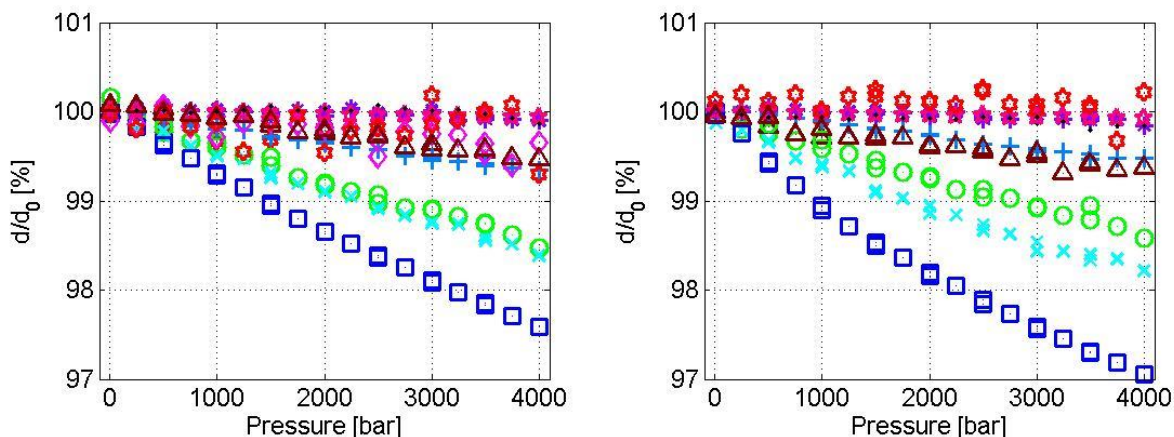
Figure 2: Relative change of the interplanar distance in dependence of the pressure. Paper (left) vulcanized fiber (right)

Here, it can be seen, that rising pressure decreases the interplanar distances anisotropically. This effect is reversible. The interplanar distance of the Bragg reflection assigned with the 200-plane of cellulose I_β (blue squares) shows the strongest changes with pressure. The 2nd (cyan x) and the first reflection (green circles) also show a change, they are assigned with the 110 and the 1-10-plane. The 3rd peak (middle blue crosses) and the 9th (brown triangles) also show minor changes. Further data analysis is in progress.

Acknowledgement

References

[1] Y. Nishiyama, J. Sugiyama, H. Chanzy, P. Langan; *Crystal Structure and Hydrogen Bonding System in Cellulose I alpha from Synchrotron X-ray and Neutron Fiber Diffraction*, JACS **125**, 14300-14306 (2003) [2] Y. Nishiyama, P. Langan, H. Chanzy; *Crystal Structure and Hydrogen-Bonding System in Cellulose I beta from Synchrotron X-ray and Neutron Fiber Diffraction*, JACS **124**, 9074-9082 (2002) [3] J. A. Kaduk, Thomas N. Blanton; *An improved structural model for cellulose II*, Powder Diffr. **28**, 3, 194-199 (2013) [4] Y. Nishiyama, S. Kuga, T. Okano; *Mechanism of mercerization revealed by X-ray diffraction*, J. Wood Sci., **46**, 452-457 (2000) [5] C. Krywka, C. Sternemann, M. Paulus, N. Javid, R. Winter, A. Al-Sawalmih, S. Yi, D. Raabe and M. Tolan, J. Synchrotron Rad. 14, 244 (2007)

Fabrication of zeolitic-imidazolate framework (ZIF) thin films on quartz crystal microbalance substrate

Min Tu[a], Suttipong Wannapaiboon[a], Christian Sternemann[b] Roland A. Fischer[a]

[a]Lehrstuhl für Anorganische Chemie II – Organometallics and Materials, Ruhr Universität Bochum; [b]Fakultät Physik/DELTA, Technische Universität Dortmund

As a sub-class of MOFs, zeolitic-imidazolate frameworks (ZIFs) constructed by linking metal centers (e.g., Zn, Co and Cd) with imidazolate ligands show high porosity, structural diversity, tunable surface functionality, structural flexibility, and in particular, good chemical and thermal stability which are essential for realistic applications.[1] Generally, in order to employ ZIFs for chemical detection (except those based on luminescence quenching), external means of signal transduction such as optical, electrical, or mechanical are necessary. Thus, integrating MOFs as thin films on device surfaces enables to form a physical interface for signal transduction.[2] As the change in oscillating frequency of quartz crystal microbalance (QCM) is directly related to the mass change on the surface, it has shown its applicability. Both, single chemical detection and selective sensing from a mixture of two components can be realized by coupling the QCM with MOF thin films.[3,4] Therefore, we fabricated thin films of sodalite-type (SOD) ZIFs (ZIF-7, 8, 9, 67, 90 and ZIF-65-Zn) with different metal centers (Zn and Co) and functional organic moieties on SiO_2 coated QCM substrates for the detection of volatile organic compounds in the vapor phase(VOCs) (Figure 1).
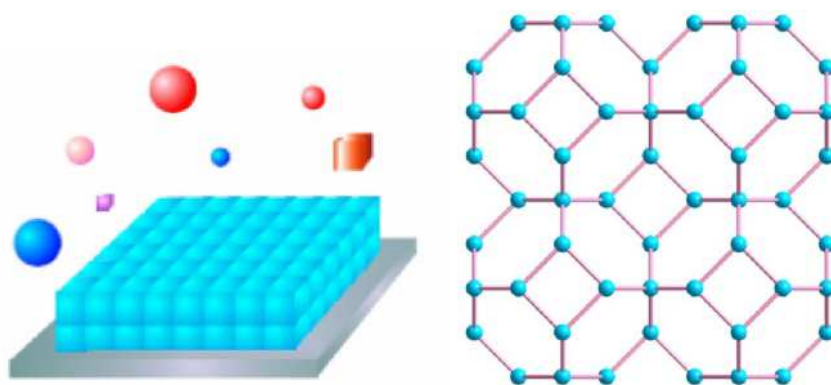
Figure 1 Schematical illustration of the detection of vapor phase VOCs using ZIF/QCM devices (left) and the topology (SOD) of ZIF thin films fabricated in this work.

In order to determine the crystal structure of the fabricated thin films, grazing incident x-ray diffraction (GIXRD) measurements were performed at Beamline BL09 at

DELTA Dortmund. The integrated GIXRD patterns are shown in Figure 2. The XRD patterns of as-prepared ZIFs match the corresponding calculated bulk ones, demonstrating the successful fabrication of these ZIF structures on the QCM substrates without impure phases. In addition, as shown in Figure 3, more growth cycles give rise to higher reflection intensity, indicating the increase of film thickness.
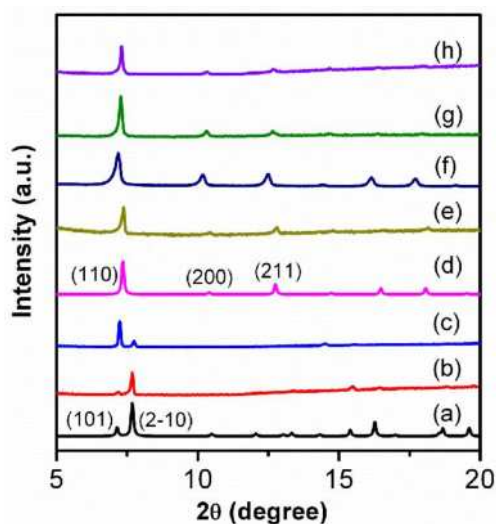
Figure 2 GIXRD patterns of ZIF thin films grown on SiO_2 surface with 10 deposition cycles in comparison with calculated ZIF-7 and ZIF-8, respectively: (a) calculated bulk ZIF-7 (hexagonal); (b) ZIF-7; (c) ZIF-9; (d) calculated bulk ZIF-8 (cubic); (e) ZIF-8; (f) ZIF-65-Zn; (g) ZIF-67; (h) ZIF-90.
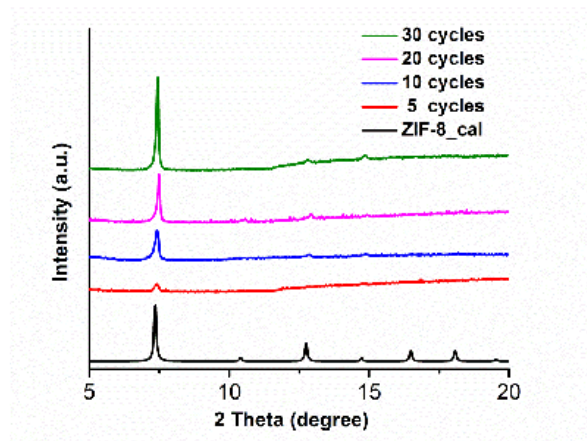
Figure 3 GIXRD patterns of ZIF-8 thin films deposited on SiO_2 coated QCM substrates with different number of growth cycles.

References

1 R. Banerjee, A. Phan, B. Wang, C. Knobler, H. Furukawa, M. O'Keeffe and O. M. Yaghi, *Science*, 2008, **319**, 939-943.

2 M. Tu, S. Wannapaiboon and R. A. Fischer, *Inorganic Chemistry Frontiers*, 2014, **1**, 442-463.

3 M. Tu and R. A. Fischer, *Journal of Materials Chemistry A*, 2014, **2**, 2018-2022.

4 B. Liu, M. Tu and R. A. Fischer, *Angewandte Chemie International Edition*, 2013, **52**, 3402-3405.

Investigation of phase formation and identification of phase boundaries in Ti-Ni-Sn thin-film materials libraries

Matthias Wambach

Werkstoffe der Mikrotechnik, Institut für Werkstoffe, Fakultät Maschinenbau

Ruhr-Universität Bochum, D-44801 Bochum

The main concept of combinatorial materials science (CMS) is to accelerate the process of finding new materials with optimized properties by fabricating and analyzing multiple samples in a single step. One of the prominent techniques of creating a so-called materials library is the thin film approach. Here compositional gradients are created on a substrate, e.g. by sputtering, followed by processing and analysis steps. By using the CMS approach large areas of the compositional space can be mapped for their properties and singular effects may be identified that might not be found in a "one-by-one" approach.

A critical success factor of this technique is managing the opposing objectives of covering a wide compositional area with one sample and the ability to identify features in narrow compositional regions in a reasonable time frame. In this regard X-ray diffraction using a Synchrotron source can be beneficial. Due to a more intense source of X-Rays, the diffraction measurements can be performed in less time with a smaller spot size than comparable lab X-Ray diffractometers allow.

As a proof of principle, a materials library of the Ti-Ni-Sn system was investigated. This system has been investigated especially for the thermoelectric properties of the TiNiSn phase. For this phase the concept of enhancing the thermoelectric performance by impurity doping has been proven [1]. The initial crystal structure of the TiNiSn phase is maintained while the impurities scatter phonons thus reducing the thermal conductivity (usually by substitution of isoelectronic elements on the Ti-site) or adjusting the carrier concentration (usually on the Sn-site). A similar approach to enhance the thermoelectric performance of a system is to introduce a finely dispersed second phase which also impedes the phonon propagation through the material. Douglas et al. showed that this can be realized for TiNiSn with $TiNi_2Sn$ being the second phase [2].

In the Ti-Ni-Sn materials libraries it is important to be able to identify single- and multi-phase regions in order to extract the structure-property relationship. In this study XRD patterns of a Panalytical X'Pert Pro are compared with results from the Synchrotron
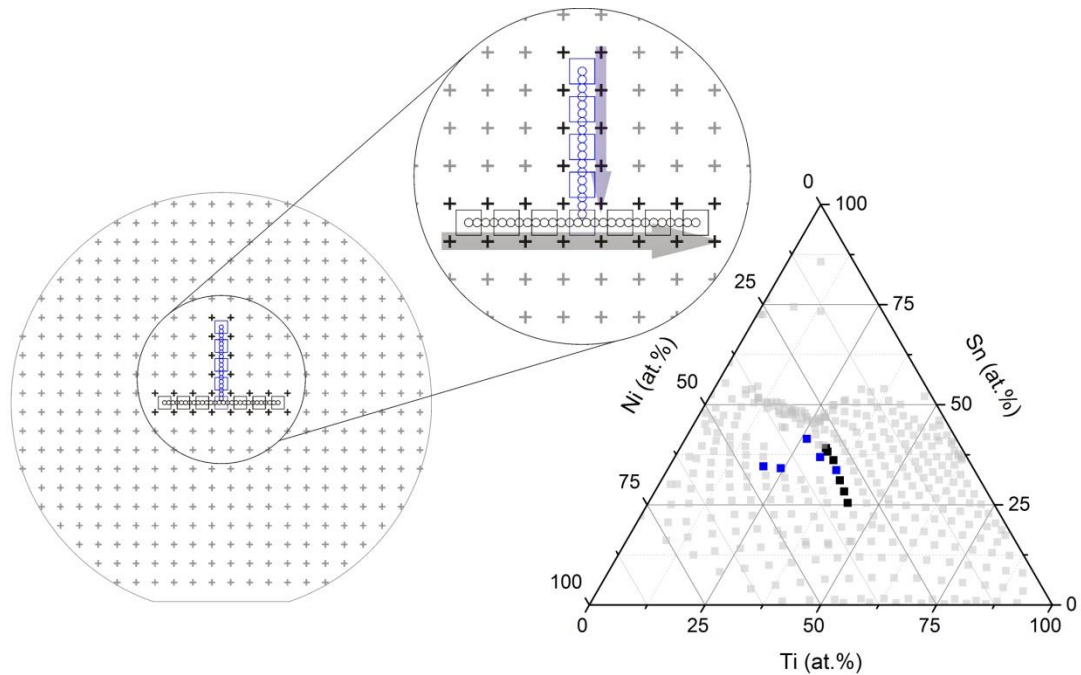
Figure 1: View of the materials library (left) and the ternary diagram of the investigated Ti-Ni-Sn system (right). The blue and black squares show the measurement areas that were measured using the X'Pert Pro setup while the circles show measurement areas measured at the DELTA beam line in Dortmund.

Beamline 09 at DELTA Dortmund using a beam energy of 20 keV and a MAR345 detector. Figure 1 shows the investigated measurement areas. The distance between adjacent measurement areas for X'Pert Pro data is 4.5 mm while the distance between points taken at DELTA is 1 mm. A finer measurement grid could be used at DELTA since the spot size of the beam is approximately 0.8×1 mm^2 compared to 3×5 mm^2 for the X'Pert Pro setup. The line scan setup at DELTA was realized by a computer-controlled x-y stage. Two line scans were measured at DELTA around the 1:1:1 composition of the Ti-Ni-Sn materials library.

The results of the two line scans are shown in figures 2 and 3. In figure 2 the XRD patterns of compositions from $Ti_{20}Ni_{45}Sn_{35}$ to $Ti_{36}Ni_{30}Sn_{34}$ are presented. For a comparatively low Ti and high Ni content a three phase region of the TiNiSn, $TiNi_2Sn$ and Ni_3Sn_4 was identified. When the composition approaches the 1:1:1 ratio of Ti, Ni and Sn, the diffraction peaks of $TiNi_2Sn$ and Ni_3Sn_4 disappear and only TiNiSn peaks are visible.

Compared to the X'Pert Pro data, the patterns taken at DELTA Dortmund show a better signal to noise ratio. The absence of diffraction peaks for the Si substrate is due to the glancing angle diffraction setup that was used. This additionally facilitates the phase identification and further analysis of the pattern. Especially weak peaks appear clearer and a distinct transition from multi-phase to a single-phase pattern can be identified.

Figure 3 shows a line scan taken perpendicular to the line scan shown in figure 2. Here composition ranges from $Ti_{43}Ni_{31}Sn_{26}$ to $Ti_{32}Ni_{29}Sn_{39}$ were investigated. At a composition of $Ti_{43}Ni_{31}Sn_{26}$ the structure seems to mainly consist of the Ti_2Ni_2Sn phase with traces of $TiNi_2Sn$ and $TiNiSn$. The tetragonal Ti_2Ni_2Sn phase (U_2Pt_2Sn structure type) has only recently been identified by Romaka et al. [3]. With decreasing Ti and increasing Sn concentration, the TiNiSn phase becomes the dominant phase while peaks of Ti_2Ni_2Sn and $TiNi_2Sn$ disappear. At the composition of $Ti_{32}Ni_{29}Sn_{39}$ diffraction peaks of the pure Sn phase appear alongside TiNiSn. Here also weak peaks can be identified easier than with the X'Pert Pro setup.

In this study the realization of a line scan diffraction setup with improved resolution compared to lab-size diffraction setups was proven. Due to the smaller spot size of the beam a finer measurement grid was realized while also utilizing a better signal to noise ratio in the diffraction patterns. To further improve this technique, the measurement time has to be decreased. While the average measurement time per data point is about 12 minutes with the X'Pert Pro setup, measurements with the described setup at DELTA took around 7 minutes per data point. Taking into account that the amount of diffraction patterns per measurement area increases by at least five-fold, future efforts should either focus on small areas of interest or try to optimize the time per measurement.

References

[1] Sung-Wng Kim, Yoshisato Kimura, Yoshinao Mishima, High temperature thermoelectric properties of TiNiSn-based half-Heusler compounds, Intermetallics, Volume 15, Issue 3, March 2007, Pages 349-356, ISSN 0966-9795, http://dx.doi.org/10.1016/j.intermet.2006.08.008.

[2] Enhanced thermoelectric properties of bulk TiNiSn via formation of a TiNi2Sn second phase Douglas, Jason E. and Birkel, Christina S. and Miao, Mao-Sheng and Torbet, Chris J. and Stucky, Galen D. and Pollock, Tresa M. and Seshadri, Ram, Applied Physics Letters, 101, 183902 (2012), DOI:http://dx.doi.org/10.1063/1.4765358

[3] V.V. Romaka, P. Rogl, L. Romaka, Yu. Stadnyk, N. Melnychenko, A. Grytsiv, M. Falmbigl, N. Skryabina, Phase equilibria, formation, crystal and electronic structure of ternary compounds in Ti–Ni–Sn and Ti–Ni–Sb ternary systems, Journal of Solid State Chemistry, Volume 197, January 2013, Pages 103-112, ISSN 0022-4596, http://dx.doi.org/10.1016/j.jssc.2012.08.023.
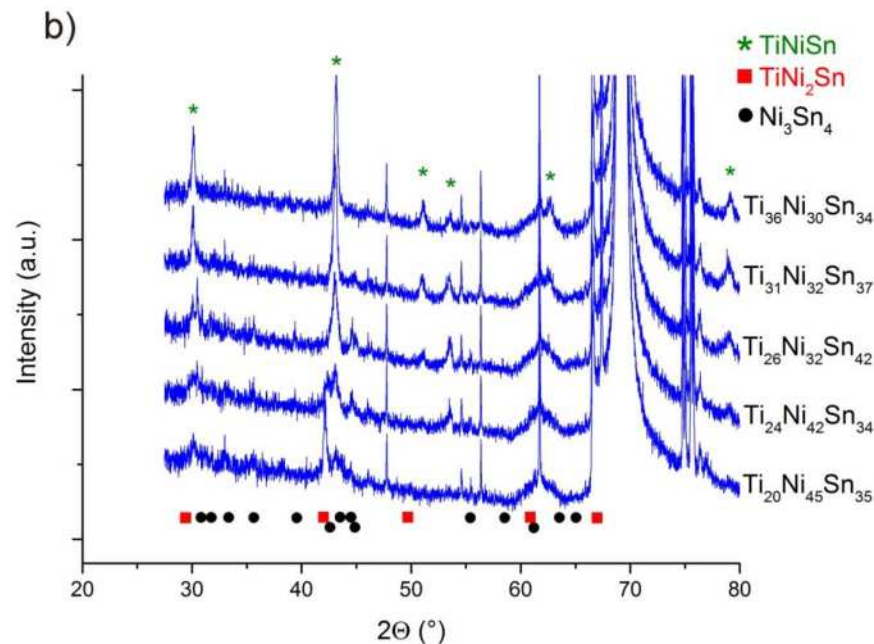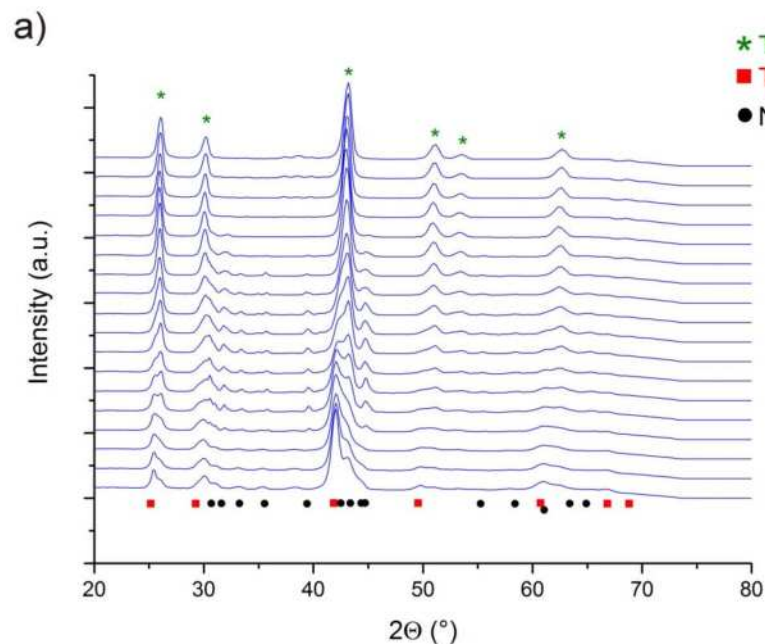
Figure 3: a) XRD patterns obtained at Beamline 09, b) XRD patterns measured using a Panalytical X'Pert Pro setup for $Ti_{20}Ni_{45}Sn_{35}$ to $Ti_{36}Ni_{30}Sn_{34}$.
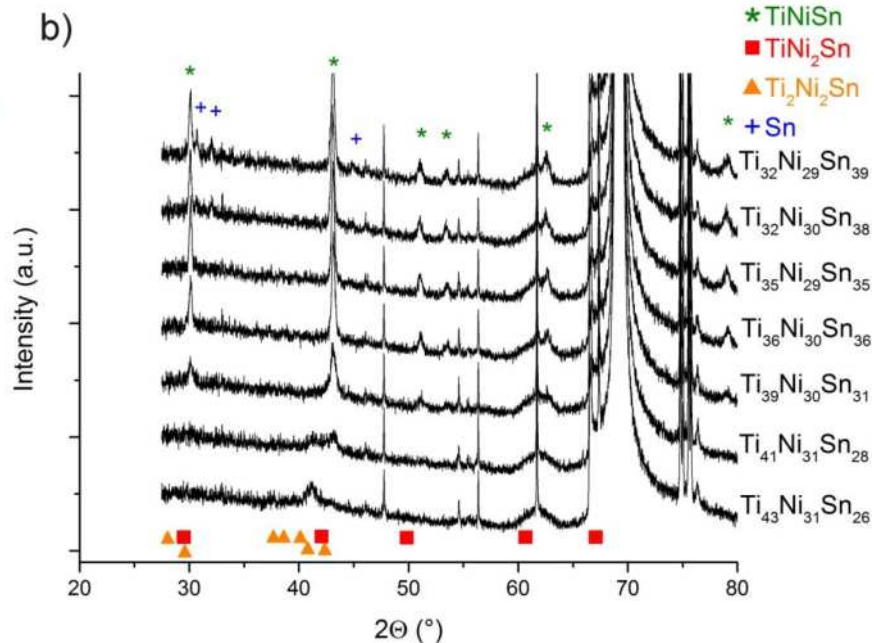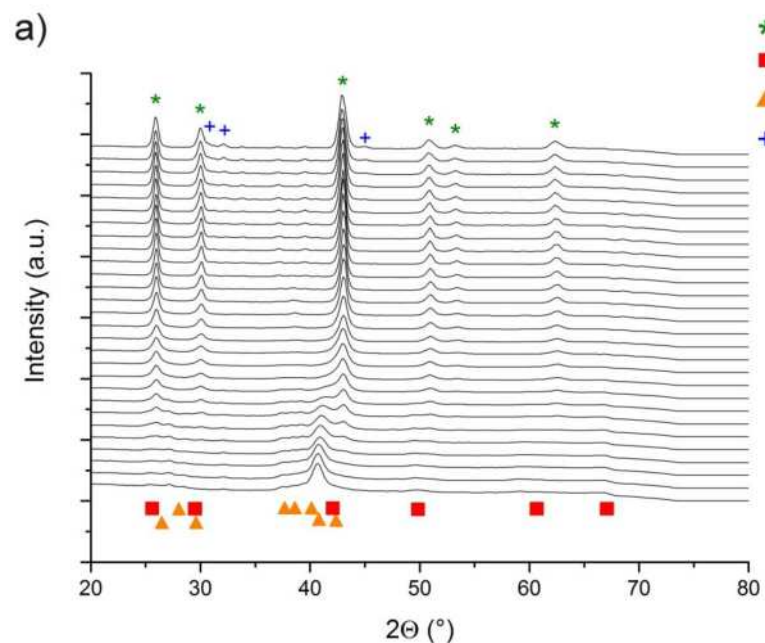
Figure 2: a) XRD patterns obtained at Beamline 09, b) XRD patterns measured using a Panalytical X'Pert Pro setup for $Ti_{43}Ni_{31}Sn_{26}$ to $Ti_{32}Ni_{29}Sn_{39}$

Crystallinity and Adsorption Capacity Enhancing of Stepwise Liquid Phase Epitaxial Moisture-tolerant MOF Thin Film Growths by Coordination Modulation Method

Suttipong Wannapaiboon[1], **Kenji Sumida**[2], **Katharina Dilchert**[1], **Min Tu**[1],

Shuhei Furukawa[2], **Susumu Kitagawa**[2], **Roland A. Fischer**[*,1]

[1] *Chair of Inorganic Chemistry II-Organometallics and Materials Chemistry, Faculty of Chemistry and Biochemistry, Ruhr-Universität Bochum, D-44780 Bochum, Germany*
[2] *Institute for Integrated Cell-Material Sciences (iCeMS), Kyoto university, Yoshida, Sakyo-ku, Kyoto 606-8501, Japan*

Stepwise liquid phase epitaxial growth (LPE) is a promising method to fabricate precise-controlled MOF thin films even at low temperature when coupled with the controlled SBUs approach (CSA) [1,2]. Integrating into practical uses, not only MOFs with high stabilities but also the preparative methods need to be considered to achieve such desired performances. The $[Zn_4O(L)_3]_n$ MOF-5 analog structures [L = functionalized derivatives of the 3,5-dimethyl-4-carboxypyrazolato (dmcapz) parent linker] is one of candidates that feature such high chemical, thermal and mechanical stabilities and good selective adsorption properties even when operated at ambient conditions [1,2]. According to our previous work, the highly-crystalline homostructured and the heteroepitaxial MOF-on-MOF $[Zn_4O(L)_3]_n$ thin films were successfully fabricated by employing the stepwise LPE method in the continuous flow fashion [2]. In order to improve the synthetic procedure, Coordination Modulation (CM) technique [3,4] is applied into the CSA-LPE method aiming to retard the high degree of nucleation at the early stage and enhance the growth of the preformed nuclei into well-defined particles by altering the coordination equilibrium between metal SBUs and linkers (Figure 1).
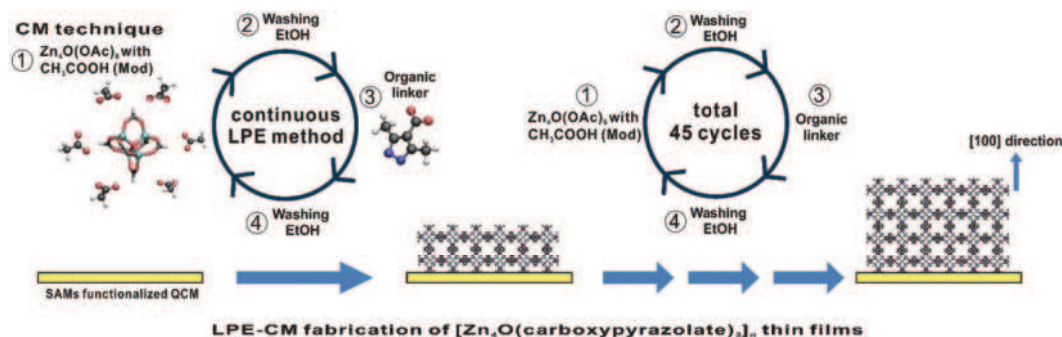
Figure 1. Schematic illustration of the fabrication of $[Zn_4O(dmcapz)_3]_n$ thin films by the stepwise liquid phase epitaxial growth coupled with the coordination modulation technique (LPE-CM)

The presence of acetic acid as a modulator plays a role in altering the coordination equilibrium between metal SBUs and organic linker, which therefore affects the kinetic LPE growth of MOF thin films. The adding of modulators up to the modulator-to-linker (Mod:L) mole ratio of 2:1 enhances the deposition of the MOF film on the substrate. However, the higher Mod:L ratio retards the kinetic deposition leading to the significantly lower deposited mass (Figure 2, Left). Interestingly, using of modulators in the optimal ratio during the LPE fabrication improves the crystallinity of the MOF films and controls the crystallographic orientation along the film growth direction as shown the prefered [100]–related orientation in the out-of-plane XRD patterns

(Figure 2, Middle). The discrete pattern of 2-dimensional grazing incidence X-ray diffraction (2D-GIXRD, performed at Beamline BL9 of DELTA) provides that the MOF crystallites have been preferably attached to the substrate surface by their bottom facets regarding to the epitaxial growth in the [100]-related orientation during the deposition (Figure 2, Right). Moreover, the methanol total adsorption capacity of the LPE-CM-fabricated MOF films is significantly enlarged according to the higher contribution of the effective mass (or the highly-crystalline MOF component) on the QCM substrate (Figure 3). The integrated LPE-CM method opens the way to fabricate the high-quality MOF thin films on the given substrates in a precise-controlled manner.
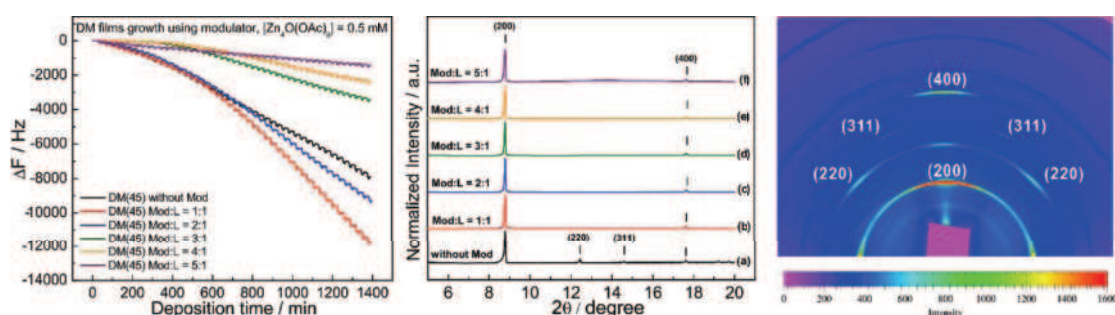
Figure 2. (Left) In-situ monitoring of QCM frequency change during the fabrication of $[Zn_4O(dmcapz)_3]_n$ thin films by LPE-CM method using the different modulator-to-linker ratio; (Middle) the corresponding out-of-plane XRD patterns and (Right) the two-dimensional grazing incidence XRD (2D-GIXRD) pattern of the film using 2:1 modulator-to-linker mole ratio.
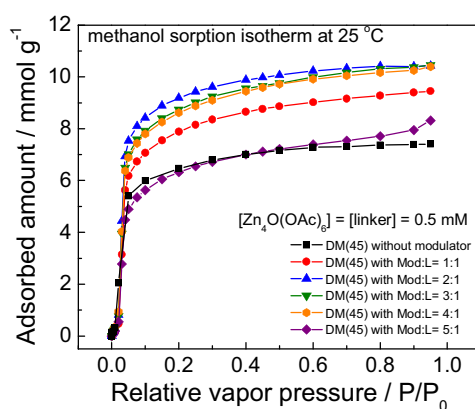
Figure 3. Methanol adsorption isotherm at 25°C of the $[Zn_4O(dmcapz)_3]_n$ thin films fabricated with various modulator-to-linker mole ratio

References

[1] A. Betard, S. Wannapaiboon, R.A. Fischer, *Chem. Commun.*, 2012, 48, 10493.

[2] S. Wannapaiboon, M. Tu, R.A. Fischer, *Adv. Funct. Mater.*, 2014, 24, 2696.

[3] T. Tsuruoka, S. Furukawa, Y. Takashima, K. Yoshida, S. Isoda, S. Kitagawa, *Angew. Chem. Int. Ed.*, 2009, 48, 4739.

[4] A. Umemura, S. Diring, S. Furukawa, H. Uehara, T. Tsuruoka, S. Kitagawa, *J. Am. Chem. Soc.*, 2011, 133, 15506.

Investigation of time dependency of phase transformation during diffusion alloying of Nb-rich tool steels by x-ray diffraction using synchrotron radiation

A. Weddeling[1], F. van gen Hassend[1], S. Huth[1]

[1]Ruhr-Universität Bochum, Institut für Werkstoffe, Lehrstuhl Werkstofftechnik, Universitätsstraße 150, D-44801 Bochum, Germany

Stainless tool steels highly alloyed with niobium can be powder metallurgical produced using the novel technique of diffusion alloying. Gas atomized carbon free steel powder is subsequently mixed with graphite and hot isostatically pressed (HIP). The atomized powder contains the intermetallic $NbFe_2$ Laves phase that, when carbon has been added in the form of graphite, transforms into MC-type carbides during HIP. The obtained microstructure features a fine distribution of MC-type carbides to increase wear resistance and chromium fully dissolved in the matrix to provide good corrosion resistance [1, 2].

Ex situ XRD measurements and SEM investigations have been performed to study the phase transformation of $NbFe_2$ Laves phase into NbC carbides in Nb-alloyed stainless tool steel. The ex situ investigations showed that carbon uptake and carbide formation occur at temperatures of about 1050 °C [3]. Figure 1 shows the Nb-rich steel powder HIPed with and without graphite addition.
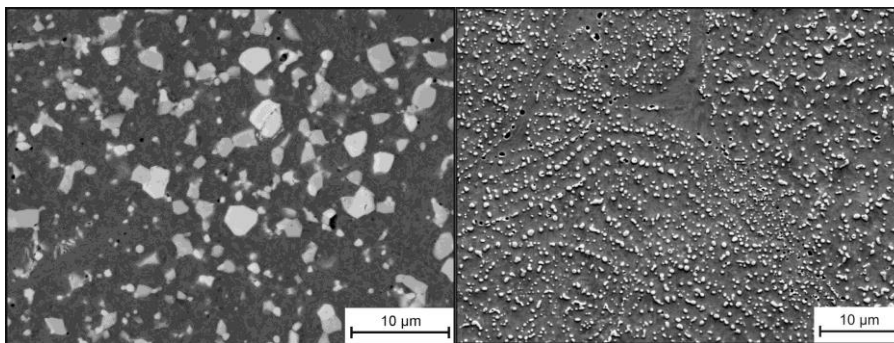
Figure 1: Intermetallic Phases $NbFe_2$ are shown on the left side, after HIP with graphite addition a finde carbide structure can be obtained (right side)

Phase transformations at elevated temperatures were investigated by means of in situ synchrotron experiments within this work. The measurements have been conducted at BL9 at the synchrotron facility DELTA using synchrotron radiation of a wavelength of 0.45919 Å. The use of the HTK 16 heating chamber from Anton Paar makes it possible to study phase transformations at high temperatures. In this study, temperatures of 950 °C and 1100 °C were chosen.
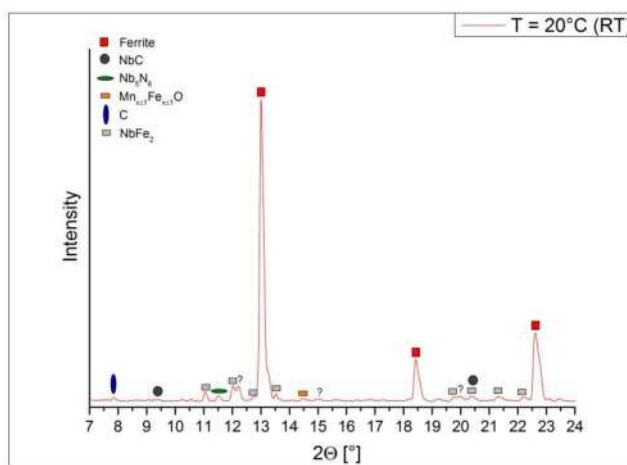
Figure 2: Diffraction pattern of the Niobium alloyed steel powder admixed with graphite prior to heat treatment

Figure 2 shows the measurement at room temperature prior to the heating stage. It can be seen that the steel is containing mainly ferrite and Laves phase. Small amounts of NbC carbide, Nb_5N_6 nitride and MnFeO oxide can be detected. The added graphite can be measured as well.

The measurement at 950 °C confirms prior performed ex situ investigations. No Nbphase transformation can be observed at that temperature. The reflections of Laves phase are of the same intensity at 0 minutes and ant 10 minutes heat treatment time. The admixed graphite is detectable all the time which leads to the conclusion that no carbon has been taken up. Oxide and nitride reflections are still measurable.

Changes in the phase composition can be detected in the heating stage at 1100 °C. From the beginning on the reflections of Laves phase are smaller. With increasing holding time the reflex is further decreasing. The reflex of admixed graphite is measured at t=0 min but not measurable any more afterwards. This shows that carbon uptake has taken place. As Laves phase is decreasing other niobium rich phases are forming. A very small NbC reflection is detectable, another phase, the mixed Fe_3Nb_3C carbide is detected. In addition to niobium rich carbides also chromium rich carbides of the $M_{23}C_6$ and M_7C_3 type are forming after holding for 5 and 10 minutes at a temperature of 1100 °C. As it was mentioned before, niobium is alloyed to form carbides and withhold chromium from carbide formation to keep it dissolved in the matrix for corrosion resistance. Hence, chromium carbides are unwanted to form. A very important result of this study is to see that the chromium rich carbides cannot be detected after holding for 15 minutes at 1100 °C. This means that after formation of chromium rich carbides they dissolve again. For the application it is important to avoid the time and temperature regions where those carbides are formed.

A complete transformation from $NbFe_2$ Laves phase into NbC monocarbides could not be observed within this work. As carbon uptake and formation of carbides starts at 1100 °C the holding time has been chosen too low to finish carbide formation, completely. Therefore, further measurements with the possibility to detect time resolved precipitations will be at elevated temperatures and longer dwell times.
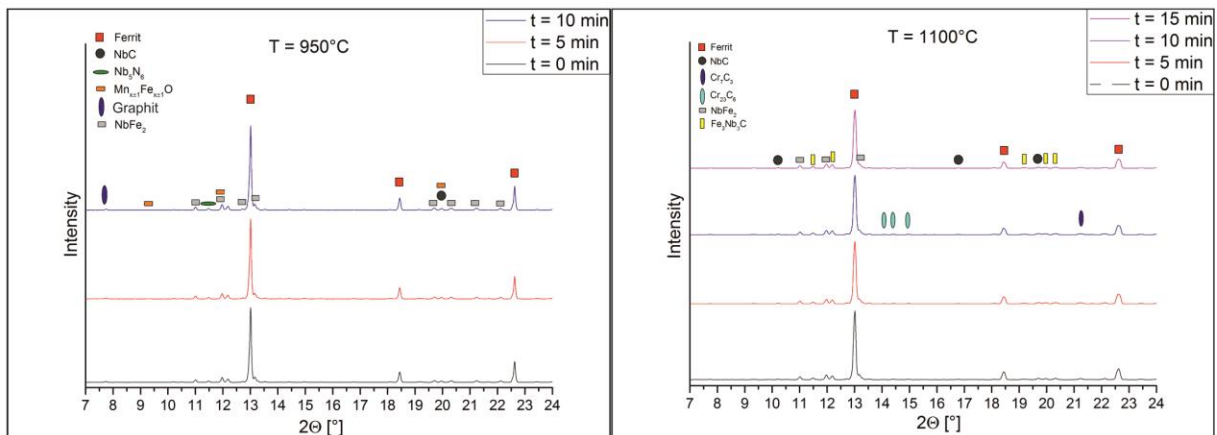
Figure 2: Measurement of the Nb rich steel powder admixed with graphite measured after reaching the aimed temperature of 950 °C and 1100 °C respectively

References

1. **Huth S, Theisen W (2009) Diffusion alloying - a new manufacturing method for PM tools steels. Powder Metall. Doi:10.1179/174329009X459593**
2. **Huth S, Krasokha N, Theisen W (2009) Development of wear and corrosion resistant cold work tool steels produced by diffusion alloying. WEAR 267(Part 1 Sp. Iss. SI):449–457**
3. **Huth S, Zumsande K, Mujica L, Krasokha N, Theisen W (2012) In: European Powder Metallurgy Association (ed) Euro PM 2012: Congress & Exhibition, Shrewsbury, pp 507–512**

Stimuli-Induced Organization Changes of Conjugated Polymers in Thin Films

Wojciech Zajaczkowski,[1] Tomasz Marszalek,[1] Felix Hinkel,[1] Marius Kuhn,[2] Manuel Hamburger,[2] Adam Kiersnowski,[3] Marzena Gradzka,[3] Klaus Müllen,[1] Wojciech Pisula[1,*]

[1] Max Planck Institute for Polymer Research, Ackermannweg 10, 55128 Mainz, Germany
[2] Organisch-Chemisches Institut, Ruprecht-Karls-Universität Heidelberg, Heidelberg, Germany
[3] Polymer Engineering and Technology Division, Wroclaw University of Technology, Wybrzeze Wyspianskiego 27, 50-370 Wroclaw, Poland
* Email: pisula@mpip-mainz.mpg.de

π-Conjugated polymers as rigid-rod type macromolecules possess limited solubility in organic solvents. The main approach to increase solubility, which is essential for their processing as organic semiconductors, is the attachment of alkyl substituents at the periphery of the polymer backbone. This allows integration of these functional materials by solution processing in organic electronics such as organic field-effect transistors. An additional effect of such solubilizing groups is the formation of distinct phases and the organization into supramolecular structures. The geometry and substitution position of the alkyls play a fundamental role for the organization. To tune the polymer organization in the cast solid-state only few approaches have been reported. One concept is based on the chemical or stimuli-induced modification of the alkyl substituents to change the polymer packing in the film.
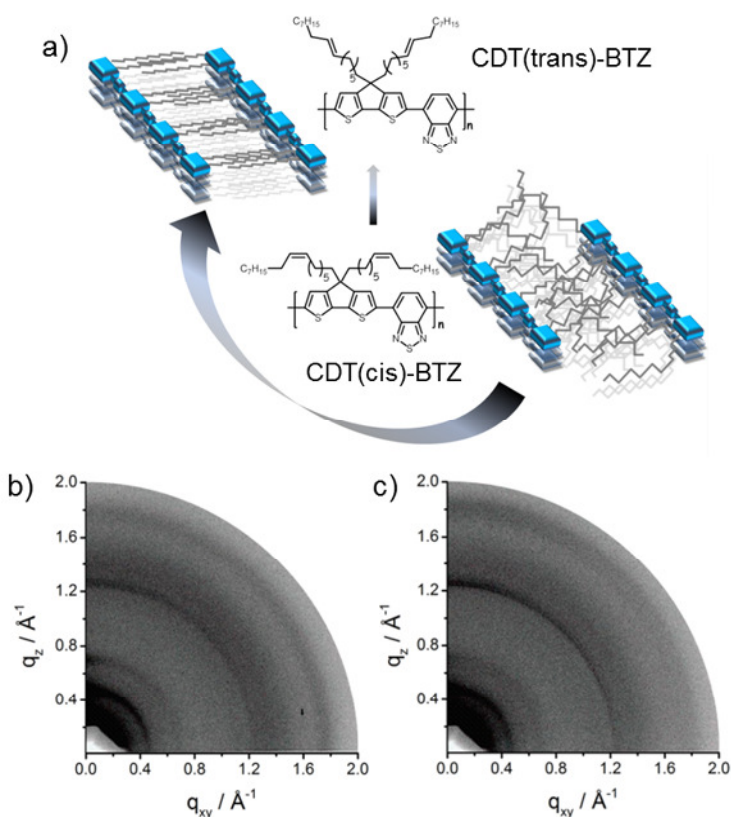
Figure 1. a) Chemical structures of CDT(*trans*)-BTZ and CDT(*cis*)-BTZ with a schematic illustration of the polymer packing and the peripheral side chain ordering, GIWAXS patterns of the films of CDT(*cis*)-BTZ for which the isomerization of the carbon-carbon double bond has been performed in b) solution and c) solid state.

In the first project published under [1], we have investigated the impact of alkenyl substituents on the behavior of cyclopenta dithiophene–benzothiadiazole (CDT–BTZ) donor (D)–acceptor (A) polymers on the supramolecular organization. The zigzag shape of *trans*-alkenes attached at the periphery of CDT(*trans*)-BTZ allows interdigitation of the solubilizing groups in the layer structure and prevents them from backfolding. On the other hand, *cis*-substituents in CDT(*cis*)-BTZ are curved and less regularly shaped providing no space for side chain interdigitation. The impact of the carbon-carbon double bond configuration in the solubilizing groups on the organization was studied

for thin films by grazing incidence wide-angle X-ray scattering (GIWAXS) on the beamline 9 of the DELTA electron storage ring in Dortmund. Furthermore, *cis−trans*-isomerization studies of CDT(*cis*)-BTZ were performed to modify the thin film organization (Figure 1a). These phenomena were in full agreement with the hypothesis that altering the configuration in the alkenyl substituent leads to a shape variation toward *trans*-isomers which was beneficial for the interlayer ordering (Figure 1b,c).
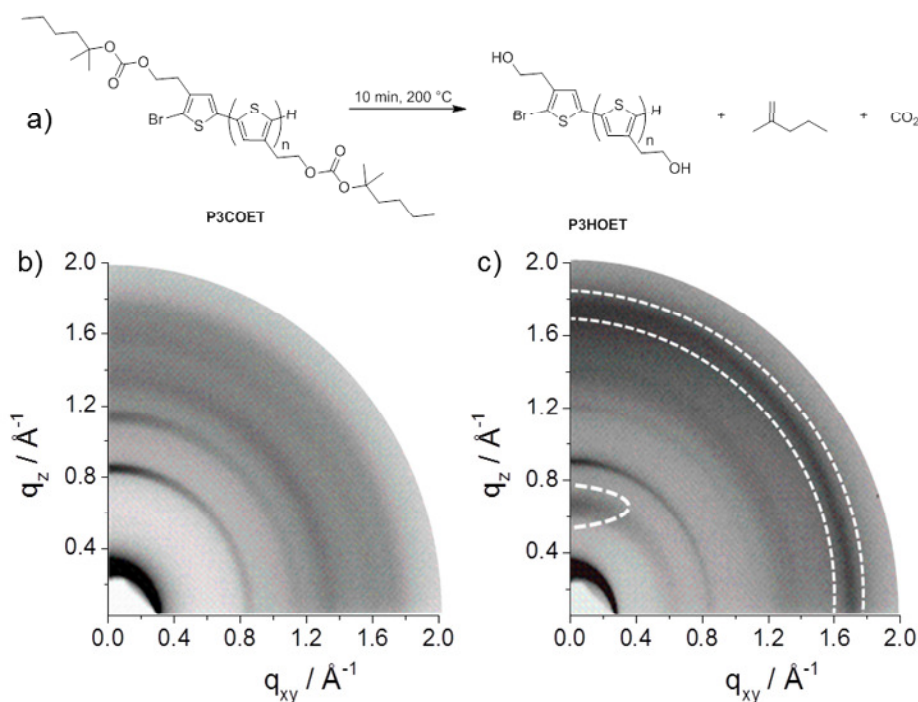
Figure 2. a) Decomposition reaction of P3COET to P3HOET after heating at 200 °C for 10 minutes, GIWAXS patterns of drop-cast films of P3COET after annealing b) at 100 °C and c) at 200 °C (meridional reflection related to the new interlayer and π-stacking peak are indicated by dashed circles).

In the second case [2], the impact of a new class of thermo-labile groups on the organization of regioregular polythiophenes (P3COET) was studied by GIWAXS before and after thermo-cleavage of the substituents. The reaction taking place at higher temperatures is shown in Figure 2a. After pyrolysis the polymer becomes insoluble and changes its organization also in blend films with PCBM. The large variation in packing for P3COET drop-cast films before and after annealing at 200 °C is evident from the GIWAXS patterns presented in Figure 2a,b. The maximum intensity of the *h00* reflection on the meridional plane implies certain preference for a quasi edge-on arrangement of the polymer backbones. The lack of a corresponding π-stacking peak of P3COET before annealing suggests highly disordered polymer packing within these layer structures (Figure 2b). After thermal cleavage of the substituents a new reflection on the meridional plane is observed related to a shorter interlayer distance (Figure 2c). A further interesting change in the drop-cast film is the increased packing order of the polymers as evident from the additional π-stacking reflection in the wide-angle scattering range related to a distance of 0.37 nm. It can be assumed that the steric demand of the substituent is reduced after thermo-cleavage allowing a stronger interaction between the conjugated P3HOET backbones.

[1] F. Hinkel, T. Marszalek, W. Zajaczkowski, S. R. Puniredd, M. Baumgarten, W. Pisula, K. Müllen, *Chem. Mater.* **2014**, *26*, 4844.
[2] M. Kuhn, J. Ludwig, T. Marszalek, T. Adermann, W. Pisula, K. Müllen, A. Colsmann, M. Hamburger, *submitted*, **2014**.

The influence of hydrostatic pressure on the structure of lipid layers

T. Zander[1], D.C.F. Wieland[1], A. Raj[2], P. Layer[1], P. Claesson[2,3], A. Dedinaite[2,3], V. Haramus[1] R.Willumeit-Römer[1]

[1] *Helmholz-Zentrum Geesthacht, Institute of Materials Research, D-21502Geesthacht*
[2] *KTH Royal Technical Institute, Department of Chemistry, SE-10044 Stockholm*
[3]*SP Technical Research Institute of Sweden, SP Chemistry, SE-11486 Stockholm*

Experimental studies indicate that the self-organisation of phospholipids and macromolecules (e.g. HA) on the cartilage is a key for low friction and wear in synovial joints and that the single components cannot provide such superior lubrication properties on their own. [1-4] Knowledge on the structural organization of the amphiphilic molecules in the presence of macromolecular constituents of synovial fluid under high pressure conditions is thus crucial for the understanding of the principles of biolubrication. We aim to gain insight into the self-assembly of structures that are responsible for providing low friction in joints, and the molecular mechanism behind the superb lubrication provided by them.

To this end we performed an in situ x-ray reflectivity (XRR) experiment on the liquid-solid interface to investigate the influence of hydrostatic pressure on the structural arrangement of multilayer systems consisting of hyaluronan (HA) and phospholipids.

The measurements were performed at the Beamline Bl9 at the synchrotron source DELTA, Dortmund, making use of the high pressure sample cell.[5] The samples were investigated at x-ray energy of 27keV in a pressure range from 1bar up to 2kbar at 55°C.

For the experiment we probed silicon (Si) supported bilayers composed of 1,2-dipalmitoyl-*sn*-glycero-3-phosphocholine (DPPC) and an composite layer of DPPC and HA in a 150mM NaCl-solution. DPPC was purchased from Avanti Polar Lipids and HA with a molecular weight of 1500kDa was purchased from Creative PEGWorks. For the DPPC/HA coating, we first let DPPC adsorb to the Si surface and let HA adsorb on top of this structure afterwards.
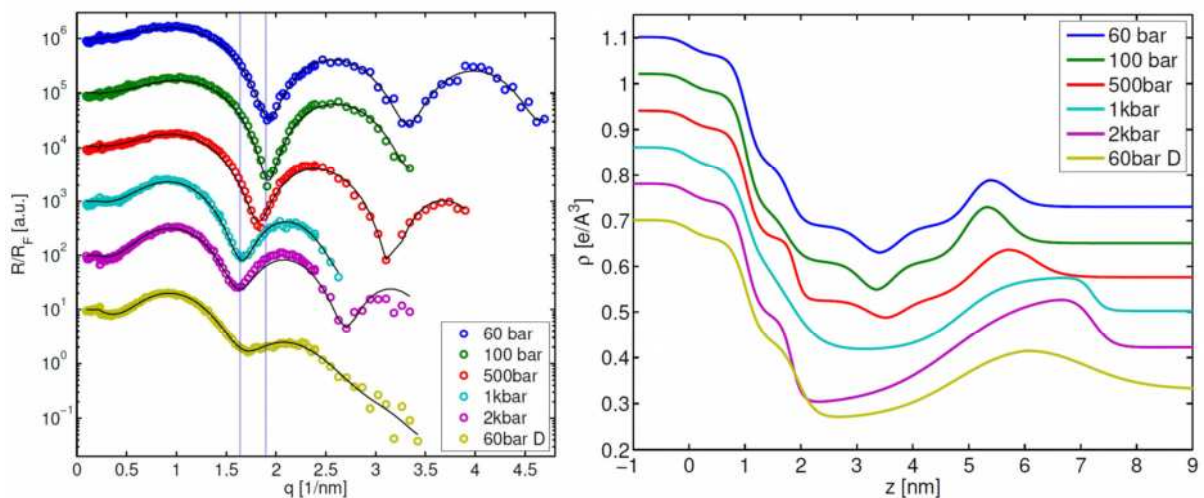
Figure 1 *Left: Fresnel normalised reflectivity curves of a DPPC bilayer at different pressures and 55°C. Black lines indicate the Fits. Right: Resulting electron density distributions.*

In figure 1 left the Fresnel normalised reflectivity curves of a DPPC sample at different pressures and 55°C can be seen. On the right hand side the corresponding electron density profiles are shown. Pressures have been first increased from 60bar up to 2kbar and afterwards a final measurement at 60bar has been performed. It can be clearly seen that an increase of the pressure has a huge effect on the sample structure. At low pressures (60bar and 100bar) the first minimum is at higher values than at high pressures (1kbar and 2kbar), indicating a lower overall thickness of the structure at low pressures. It can also be observed that the structural change, induced by high pressures, is not reversible since the last curve measured at 60bar does not has the same shape as the first curve, measured at 60bar.

The structural change that occurs after increasing the pressure above 500bar is due to the phase transition of the lipids from the liquid crystalline to the gel phase. [6]

From the electron density profiles (figure 1 right) it can be concluded, that there is a typical bilayer structure at low pressures, as it was expected for DPPC. At high pressures (above 500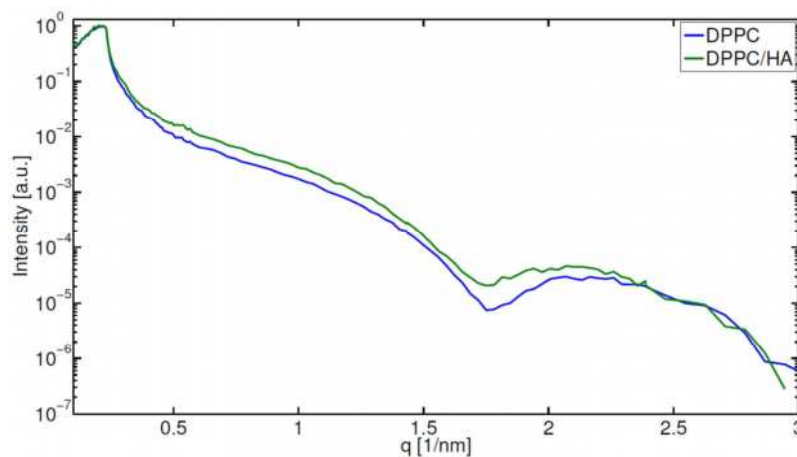bar) the density profiles show a significant different shape. They could still be interpreted as bilayers, but the structure is very smeared out and disturbed. Also a hysteresis of the layer structure after decreasing the pressure to 60 bar has been observed.

Figure 2 *Reflectivity curves of a pure DPPC sample (blue curve) and the same sample after immersing it into a HA solution (green curve). Measurements were performed at 55°C and ambient pressure.*

In figure 2 two reflectivity curves measured at 55°C and ambient pressure are shown. The blue curve shows a pure DPPC-sample and the green curve shows the same sample with an additional HA layer on top. Since the first minimum of the green curve can be found at a slightly lower q-value than the minimum of the blue curve it can been concluded that curve that there is an increase of the effective thickness of the layer, i.e. HA has adsorbed to DPPC.

References

[1] Hills, B. A. (2002) Internal Medicine Journal **32**, 242-251,

[2] Klein, J. (2006) Proceedings of the Institution of Mechanical Engineers, Part J: Journal of Engineering Tribology **220**, 691-710,

[3] Liu, C., Wang, M., An, J., Thormann, E., and Dedinaite, A.(2012) Soft Matter, **8**, 10241,

[4] Dedinaite, A.(2012) Soft Matter, **8**, 273,

[5] Wirkert, F.J. , Paulus, M. , Sternemann, C. , Nase, J. , Schroer, M.A., Wieland, D.C.F. , Bieder, S. ,Degen, P. , Rehage, H. and Tolan, M. (2013) Study of time and pressure dependent phenomena at the hard x-ray beamline bl9 of delta, In Journal of Physics: Conference Series, **425**, 202006

[6] Winter, R. and Jeworrek, C. (2009) Effect of pressure on membranes, Soft Matter, **5**, 3157

The adsorption of soy proteins at the solid - liquid interface

Paul Salmen, Michael Paulus, Patrick Degen, Julia Nase, Florian Wirkert, Christian Sternemann, Benedikt Nowak, and Metin Tolan

Fakultät Physik/DELTA, TU Dortmund, 44221 Dortmund, Germany

The encapsulation of aqueous solution in a hydrophobic matrix like fat is a common process e.g. in the food industry. However, such systems suffer from the diffusion of water molecules through the matrix, which makes these products perishable. First test experiments show that soy sauce in the capsules reduces the diffusion of water through the matrix material. A change of the contact angle of water from approximately 106° on a hydrophobic surface to 84° after dipping the surface into soy sauce hints to adsorption processes at the interface. To determine the origin of this behaviour, we characterised in situ the interfaces between hydrophilic and hydrophobic silicon wafers and aqueous solutions of soy sauce and of acid hydrolysed soy protein (AHSP) with x-ray reflectivity (XRR) at a photon energy of 27 keV. The experiments were performed at beamline BL9 using a cell developed by I. Kiesel [1]. For the production of hydrophilic surfaces, the silicon wafers were cleaned in a piranha solution for 30 minutes. For the preparation of hydrophobic surfaces, the silicon wafers were coated with octadecyl-trichlorosilane (OTS) as described in [2].

Figure 1: Electron density profiles for different concentrations of soy sauce in buffer on a hydrophobic OTS covered silicon wafer. The inset shows the XRR measurements divided by the Fresnel reflectivity of an ideal flat silicon surface and the corresponding fits.

The soy sauce and AHSP were diluted in a phosphate buffer solution in different concentrations. The pure surface was first characterised in pure buffer solution. Afterwards, most of the buffer was removed and the sample liquid including the protein solution was filled into the cell. In figure 1, XRR data and the corresponding electron density profiles obtained by a refinement of the XRR data are displayed for different

amounts of soy sauce in buffer solution. There is no clear dependence of the layer thickness on the concentration. In figure 2, the XRR data and the electron density profiles for AHSP are shown. In contrast to the first experimental series, a dependence of the layer thickness on the concentration is clearly observable. The layer thickness increases with the concentration of AHSP. Only the 50 mg/ml system does not fit into the series. For a clear determination of this effects, these measurements need to be reproduced. However, because of the similar shapes of the layers, we think that we observe in both cases (soy sauce and pure AHSP) the formation of a thin AHSP layers at the interfaces. On hydrophilic silicon wafers, no adsorption was observed (data not shown).
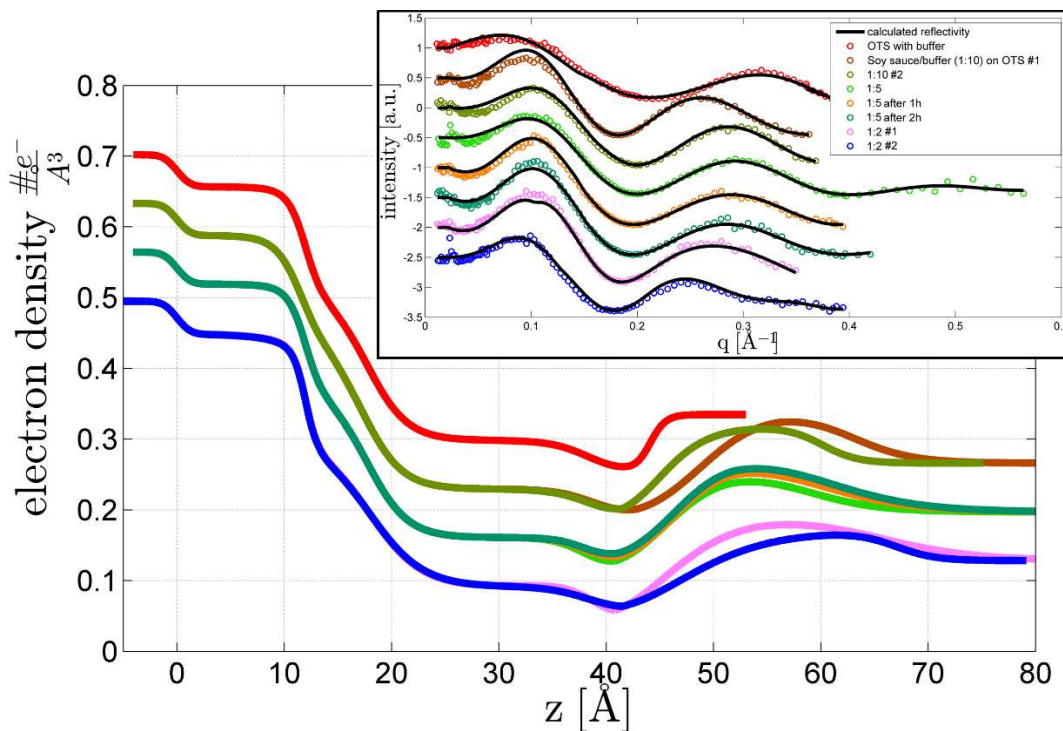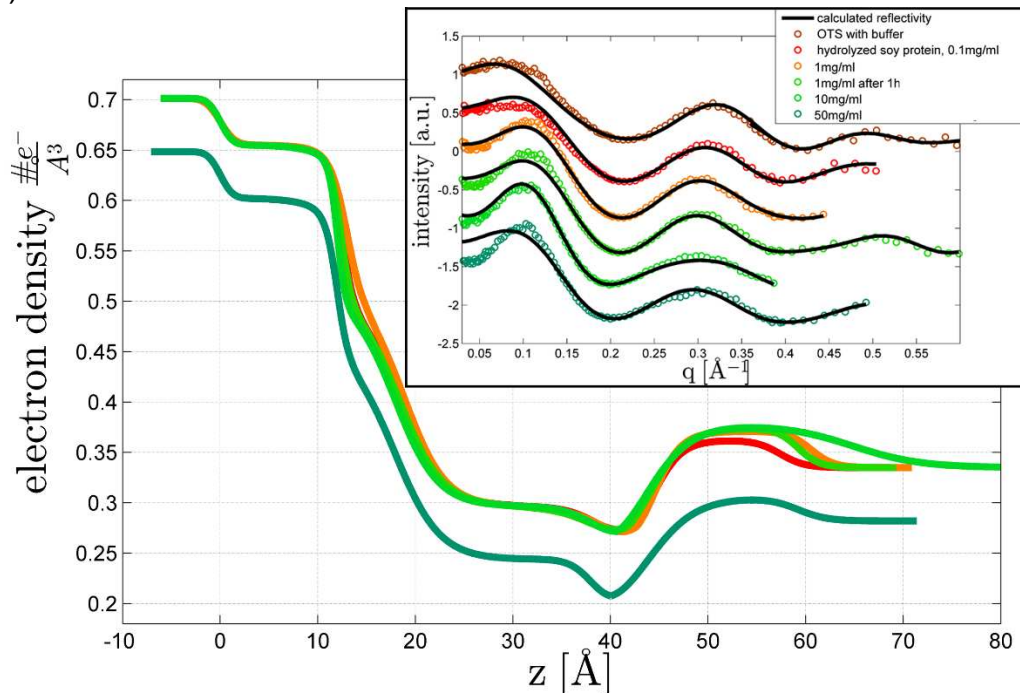

Figure 2: Electron density profiles for different concentrations of AHSP in buffer on a hydrophobic OTS covered silicon wafer. The inset shows the XRR measurements divided by the Fresnel reflectivity of an ideal flat silicon surface and the corresponding fits.

In summary, the adsorption of AHSP on hydrophobic and hydrophilic silicon wafers was analysed. The AHSP, which is a part of soy sauce, adsorbs at the interface, resulting in layers of approximately 1.5 nm thickness. Since no adsorption has been observed at hydrophilic interfaces, we assume that the adsorption is mainly driven by hydrophobic interactions. As the formed layer might act as a diffusion barrier for water molecules, AHSP can be used to stabilize water – fat capsules.

Acknowledgment

[1] I. Kiesel, M. Paulus, J. Nase, S. Tiemeyer, C. Sternemann, K. Rüster, F.J. Wirkert, K. Mende, T. Büning, M. Tolan, *Temperature Driven adsorption and desorption of proteins at solid-liquid interfaces*, Langmuir **30** 2077-2083 (2014) [2] M. Mezger, H. Reicher, S. Schöder, J. Okasinski, H. Schröder, H. Dosch, D. Palms, J. Ralston, V. Honkimäki, High resolution in situ x-ray study of the hydrophobic gap at the water octadecyl-tricholorosilaneinterface, PNAS **103**(49) 18401-18404 (2006)

A high hydrostatic pressure study of palmitic acid multilayers at the solid -liquid interface

Benedikt Nowak, Michael Paulus, Paul Salmen, Florian Wirkert, Irena Kiesel and Metin Tolan

Fakultät Physik/DELTA, TU Dortmund, 44221 Dortmund, Germany

In all living organisms, cell membranes regulate the mass transfer between the intracellular and extracellular region. The basic membrane structure consists of a lipid bilayer. These systems undergo pressure- and temperature-dependent phase transitions, which are unfavorable for living cells because they are only able to survive in the so-called fluid phase. In the presented study the pressure-dependent behavior of solid supported lipid multilayers was investigated with x-ray reflectivity (XRR) at the solid-liquid interface using the 27 keV set up of beamline BL9 at DELTA. The lipid multilayers of palmitic acid were prepared by spin coating. The measurements on multilayer systems at hydrostatic pressures up to 4000 bar were conducted in a custom-made high-pressure cell designed at the TU Dortmund and described in [1]. The temperature was 20°C.

In figure 1, the XRR data for a palmitic acid multilayer system under different pressures up to 4 kbar can be seen as a function of the wave vector transfer perpendicular to the samples surface q_z. Three Bragg reflections are clearly visible. From the q_z-position of the reflexes the thickness of a single palmitic acid bilayer has been calculated in a first step of the data analysis. The thickness of a single bilayer determined from the position of the first and third Bragg reflection in dependence of the respective pressure is displayed in figure 2. The compression of a single layer from 15 bar to 4 kbar is around 0.4 Å -0.5 Å. The deviation of 0.7 Å between the first and third reflex might be due to local variations of the surface structure. The multilayer system did not undergo a phase transition because in this case, the changing of the layer thickness would be much larger.

For a more detailed analysis of the system, the electron density profile has been determined using the Parratt algorithm. In figure 3, the density profiles obtained by a fit of the reflectivity data (see inset) are shown. For the fit, a sublayer system of five layers has been assumed.
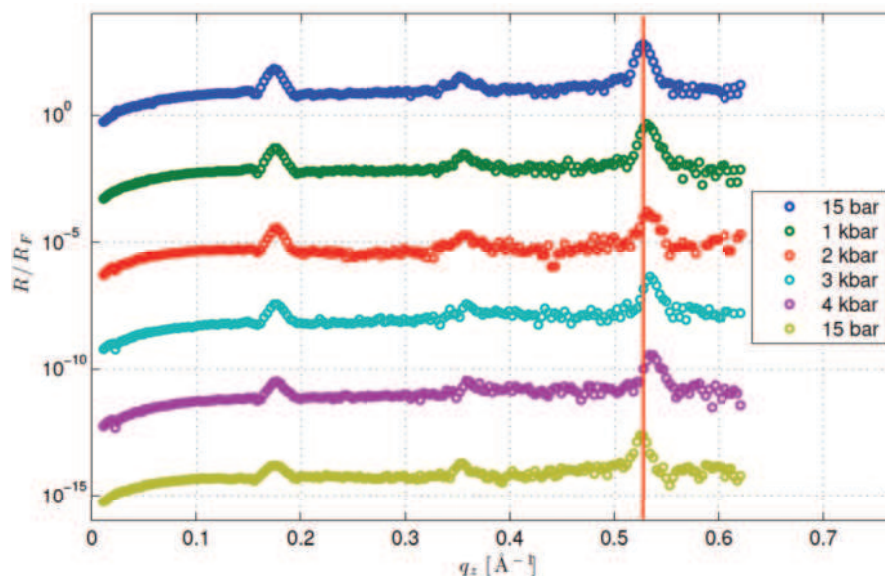
Figure 1: XRR data of a palmitic acid multilayer system. The pressure varied between 15 bar and 4 kbar. The auxiliary line illustrates the reflex shift.
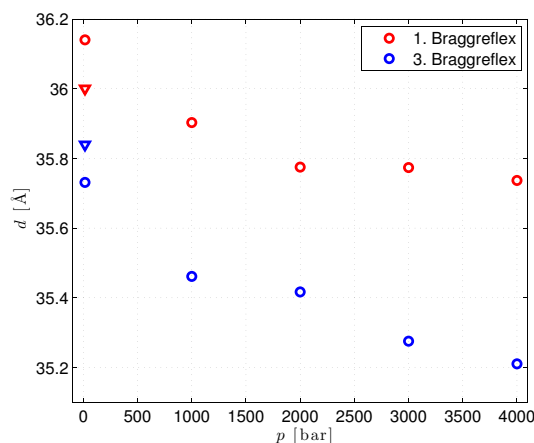
Figure 2: Bilayer thickness in dependence of the pressure calculated from the position of the first and third Bragg reflection.
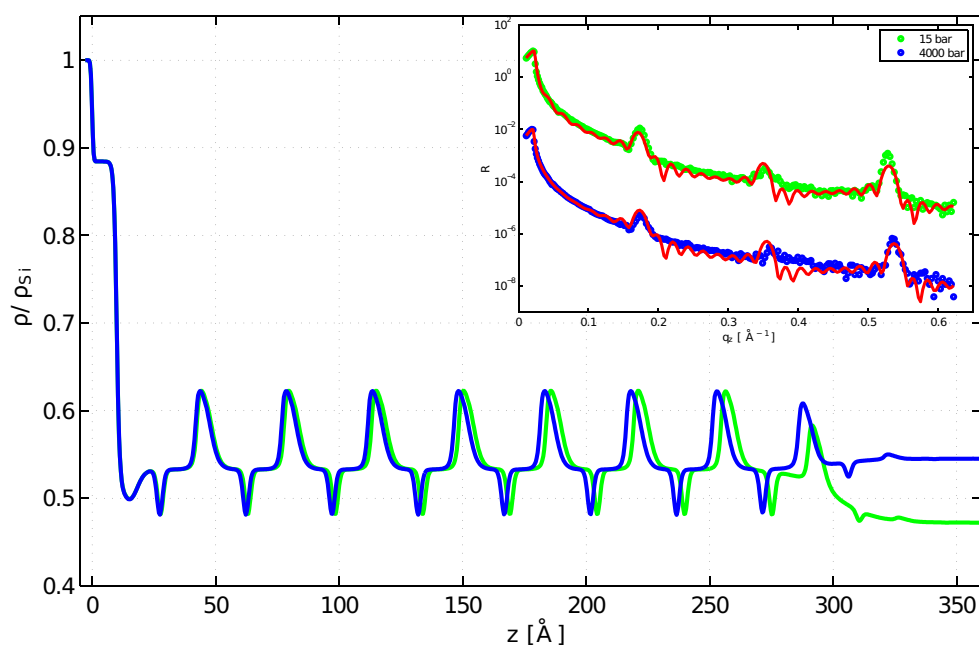
Figure 3: Electron density profile for the measurements at 15 bar and 4 kbar.
Inset: XRR data and fit for the palmitic acid multilayers.

The presented measurements demonstrate that a multilayer system consisting of palmitic acid layers is stable in water also under HHP. It has been proved, that this system didn't undergo a phase transition up to 4000 bar at 20°C. From the compression an elasticity modulus of 32 GPa was determined.

[1] F.J. Wirkert, M. Paulus, J. Nase, J. Möller, S. Kujawski, C. Sternemann and M.Tolan, X-ray reflectivity measurements of liquid/solid interfaces under high hydrostatic pressure conditions, Journal of Synchrotron Radiation **21**, 76-81 (2014)

Structural evolution of bidisperse alkyl-silane self assembled monolayers; influence of structure on wetting and dynamical properties of thin polymer films

Joshua D. McGraw, Antoine Bridet[1], Hendrik Hähl[1], and Karin Jacobs[*1]

[1] *Experimentalphysik, Universität des Saarlandes, 66123 Saarbrücken*

[*]email: k.jacobs@physik.uni-saarland.de

Over the last decades, the concept that fluids may slide along a solid boundary, slip, has become an experimentally observable phenomenon. Probes of slip range from direct, with the use of tracer particles moving near a boundary [1], to indirect, with the use of dewetting thin films [2-4], to give just two examples. The scales at which slip phenomena are observable range from nanoscopic to microscopic this is why observations have come only lately (i.e., the last few decades), in the time since miniaturization of devices and systems have become experimentally accessible and well enough controlled.

One intriguing aspect of slip of thin polymer films has been consistently observed in the last years in our group, and remains to be fully explained. By placing identical polymer films on only slightly different self assembled monolayers (SAMs), large and consistent changes in the degree to which fluids slide against the monolayers can be observed. The monolayers are typically composed of either octadecyl- or dodecyl-trichlorosilane (OTS and DTS; 18- or 12-alkanes terminated with a silicon atom). When 100 nm thick films of low molecular weight polystyrene (PS, typically less than 20 kg/mol) are placed onto the SAMs, a larger slip velocity can be seen on DTS than on OTS. Since these SAMs differ only in their respective number of carbon atoms, it has been suggested that the underlying reason for the different slip velocities is that the structure of the monolayers is different. Thus, we prepared SAMs that were prepared from silane solutions with different silane mass fractions, ϕ, of DTS, with the silane mass fraction of OTS being $1 - \phi$. The goal of this study is to relate the structure of the respective monolayer, revealed in part by X-ray reflectivity measurements performed on beamline 9 at DELTA, to the slip properties of PS on the monolayers. The latter shall be revealed by dewetting at temperatures above the polymer glass transition.

Figure 1 shows data collected at beamline 9 in March, 2014. The data for the pure
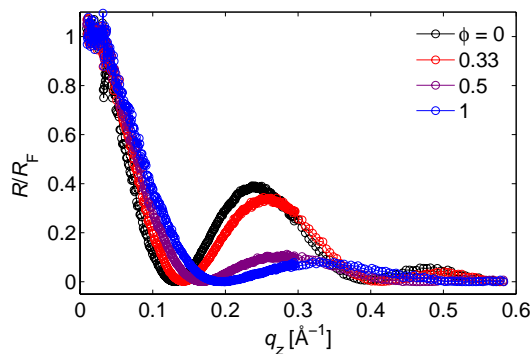
Figure 1: Figure 1. Reflectivity profiles (normalized by the Fresnel reflectivity) collected at beamline 9 from OTS ($\phi = 0$) and DTS ($\phi = 1$) SAMs, as well as SAMs with mixed compositions of OTS and DTS molecules.

OTS and DTS, $\phi = 0$ and 1 respectively, are consistent with what we have collected at the same beamline in the past [5]. The non-extremal compositions, $\phi = 0.33$ and 0.50, show reflectivity profiles that are markedly different from either of the two profiles at $\phi = 0$ and 1. Preliminary results also show that the slip velocities measured on the 'intermediate substrates are also different from those measured on the 'pure substrates.

References
[1] D. Tretheway and C. Meinhart. Phys Fluids 2002; 14: L9.
[2] R. Fetzer et al., Langmuir 2007;23:10559.
[3] O. Bumchen et al., J Phys Condens Matter 2012; 24: 325102.
[4] J.D. McGraw et al., Adv. Coll. Int. Sci., 2014; 210: 13.
[5] P. Gutfreund et al., Phys. Rev. E, 2013; 87: 012396.

Control of protein adsorption at the solid - liquid interface

Holger Göhring, Michael Paulus, Patrick Degen, Paul Salmen, Florian Wirkert, Christian Sternemann, and Metin Tolan

Fakultät Physik/DELTA, TU Dortmund, 44221 Dortmund, Germany

Many biological processes taking place at liquid - gas and solid - liquid interfaces are associated with the adsorption of proteins. Here, different surface - protein interactions like van der Waals and Coulomb interactions, but also the hydrophobic effect determine the degree of adsorption. However, the Coulomb interaction between the proteins but also between the proteins and charged interfaces can be tuned by the addition of ions into the aqueous protein solution. Here, the formation of an ion adsorption shell at charged interfaces yields a screening of charges.

We present an x-ray reflectivity study on the adsorption behaviour of the protein lysozyme at the solid - liquid interface. The experiment was focussed on the effect of sodium chloride (NaCl) on the adsorption behaviour of lysozyme at hydrophilic silica − water interfaces. Via x-ray reflectivity measurements the electron density profiles of the adsorbed lysozyme layers were determined and the adsorbed amount of protein at these interfaces was calculated.

A 10 mM phosphate buffer consisting of H_2PO_4Na and HPO_4Na_2 in ultrapure water was used, at a pH of 7. Thus, lysozyme, offering an isoelectric point of 11, carried a positive charge. The protein concentration in the buffer solution was 0.1 mg/ml. The x-ray reflectivity experiments were performed at beamline BL9 of DELTA using the 27 keV set-up. The silicon wafers (Wacker Siltronic, Burghausen, Germany) were cleaned by the Piranha cleaning procedure and stored under water until use. This treatment produces an approximately 1 nm thick silicon dioxide layer on the wafer, yielding at pH 7 a negative surface charge in contact with water. During the experiments, the sodium chloride (Merk, Germany) concentration was varied between 0 mM and 1000 mM. The wafers were first analysed in pure buffer-salt solution. Subsequently, the liquid phase was replaced by the protein-salt solution. A reflectivity scan including the measurement of the diffuse scattered radiation took about 20 minutes.

After subtracting the signal of the diffusely scattered radiation from the reflectivity signal, the data was analysed by the Parratt algorithm [1] in combination with the effective density model [2]. Two layers were used to model the silicondioxide and protein layer. The reflectivity data together with the simulated curves are shown in figure 1, while the corresponding electron density profiles are shown in figure 2. Obviosly, a monolayer of lysozyme adsorbs at the interface. However, with rising NaCl concentration the density of the layer drops down until no
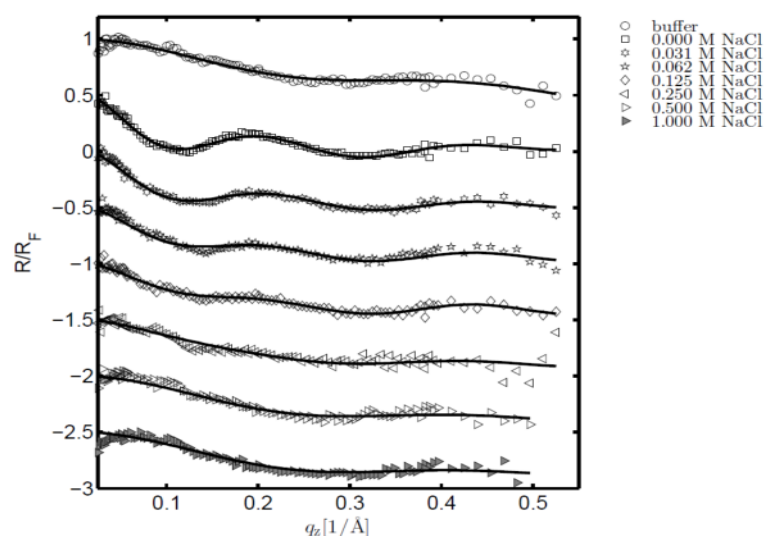
Figure 1: X-ray reflectivity data and simulations of the solid - liquid interface. The x-ray reflectivities are normalized to the Fresnel reflectivity of an ideal flat silicon wafer.

absorption is observable at a NaCl concentration of 500 mM. In a second step the electron density profile of the bare wafer – water interface was subtracted, in order to obtain the lysozyme density profile. Following the procedure as described in [3] the volume fraction profile ϕ was calculated and the layer thickness was determined (see figure 3). Again, the decreasing adsorption of lysozyme with rising salt concentration becomes visible. Interestingly, the layer thickness drops from 45 Å, which corresponds to the long axis of lysozyme, to 32 Å, which is similar to the length of the short axis of lysozyme (dimensions 30 x 30 x 45 Å^3).

In summary, the addition of NaCl reduces the absorbed amount of lysozyme at a hydrophilic silicon wafer. This behaviour can be explained by a reduced electrostatic interaction between positively charged proteins and the negatively charged surfaces. The reduced adsorption goes in hand with a transition from unoriented adsorption to adsorption with the short axis perpendicular to the solid liquid interface.

Figure 2: Electron density profiles of adsorbed lysozyme at the solid - liquid interface at different NaCl concentrations between 0 mM and 1000 mM obtained by the refinement of the reflectivity data.
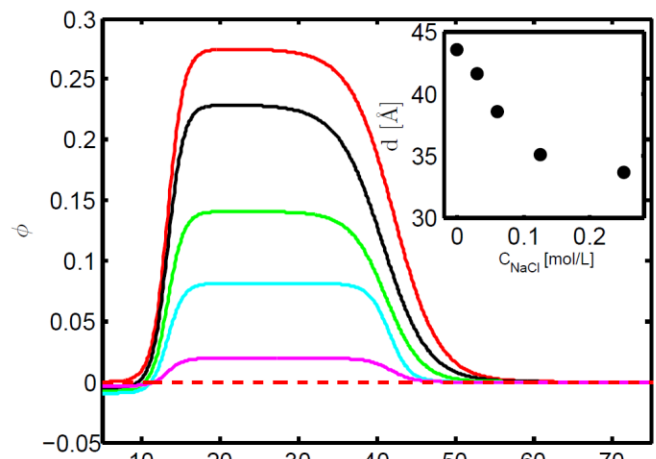
Figure 3: Salt concentration dependent volume fraction profiles of lysozyme adsorbed at the solid - liquid interface. red: c_{NaCl} = 0 mM, black: c_{NaCl} =30 mM, green: c_{NaCl} = 60 mM, cyan: c_{NaCl} = 125 mM,, magenta: c_{NaCl} = 250 mM, red dashed line: c_{NaCl} = 500 mM and 1000 mM. The inset shows the salt concentration dependent layer thickness of the lysozyme layer.

Acknowledgement

References

[1] L. Parratt, Phys. Rev. 1954, **95**, 359-369.

[2] M. Tolan, *X-ray scattering from Soft Matter Thin Films*; Springer: Berlin, 1999.

[3] I. Kiesel, M. Paulus, J. Nase, S. Tiemeyer, C. Sternemann, K. Rüster, F. J. Wirkert, K. Mende, T. Brüning, M. Tolan, Langmuir 2014, **30**, 2077.

Apolipoprotein A1 adsorption at hydrophobic solid/liquid-interfaces
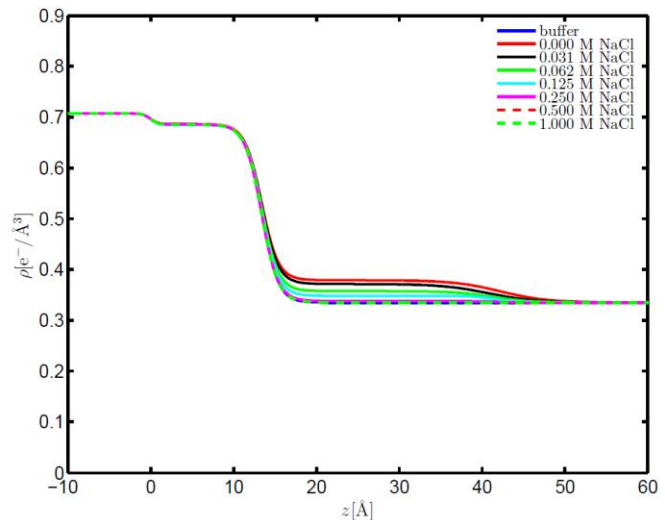
Irena Kiesel, Kolja Mende, Florian J. Wirkert, Michael Paulus, Christian Sternemann, Metin Tolan

Fakultät Physik/DELTA, Technische Universität Dortmund, 44221 Dortmund, Germany

High-density lipoproteins (HDL) are complex proteins and are essential for many processes in human live, such as transport processes though cell membranes and in the body. One of the most important proteins for the lipidmetabolism is the HDL Apolipoprotein A1 (ApoA1) [1]. It has an ringlike structure formed by four subunits (see figure 1). The ring is slightly tilted and has a size of 135 x 90 x 60 Å³. The inner ring is hydrophobic whereas the outer ring is hydrophilic. Due to this, ApoA1 forms particles with lipids and cholesterol for transportation purposes. Here, the hydrophobic part of the protein interacts with the hydrophobic tail

Fig. 1: Apolipoprotein A1

groups of the lipids. Thus, it is probable that ApoA1 interacts also with hydrophobic surfaces.
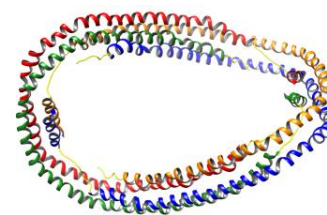
To study the adsorption behavior of ApoA1 at hydrophobic surfaces, x-ray reflectivity experiments at the solid-liquid interface at the beamline BL9 at DELTA were performed using the 27 keV x-ray reflectivity setup [2]. Previous experiments have shown that performing temperature dependent adsorption experiments in different environments gives access to different adsorption mechanisms [3]. Therefore, x-ray reflectivity measurements were conducted at several temperatures. The hydrophobic surfaces were prepared using octadecyltrichlorosilan (OTS) on a silicon wafers [4]. By dipping the wafers into protein solution, the proteins adsorb at the wafers surface. Afterwards the wafers were transferred into two different environments, namely pure phosphate buffer and protein solution.

The resulting reflectivities, normalized by the Fresnel reflectivity for an ideal flat silicon substrate, are shown in figure 2. The reflectivities on the left side are the measurements in protein solution, whereas the right reflectivities are measured in buffer. Reference measurements of a pure silicon wafer with a native silicon dioxide layer in buffer and a OTS coated wafer in buffer are also displayed (dark and bright gray data points). The colored data points are the measurements with protein under increasing temperature. In order to investigate time-dependent changes, some reflectivity measurements were repeated at selected temperatures. The solid lines in figure 2 represent reflectivities calculated from the electron density profiles (EDP) shown in figure 3.
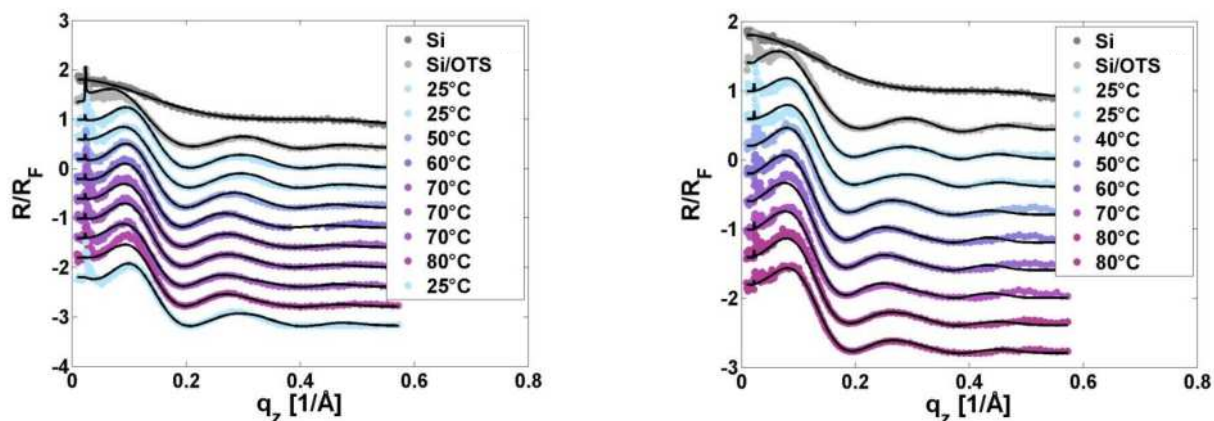
Fig. 2: Temperature dependent x-ray reflectivitiy data of Apolipoprotein A1 at a hydrophobic interface in protein solution (left) and in buffer (right). The reflectivities are Fresnel-normalised and shifted by a constant value for clarity. Some reflectivity measurements were repeated to exclude
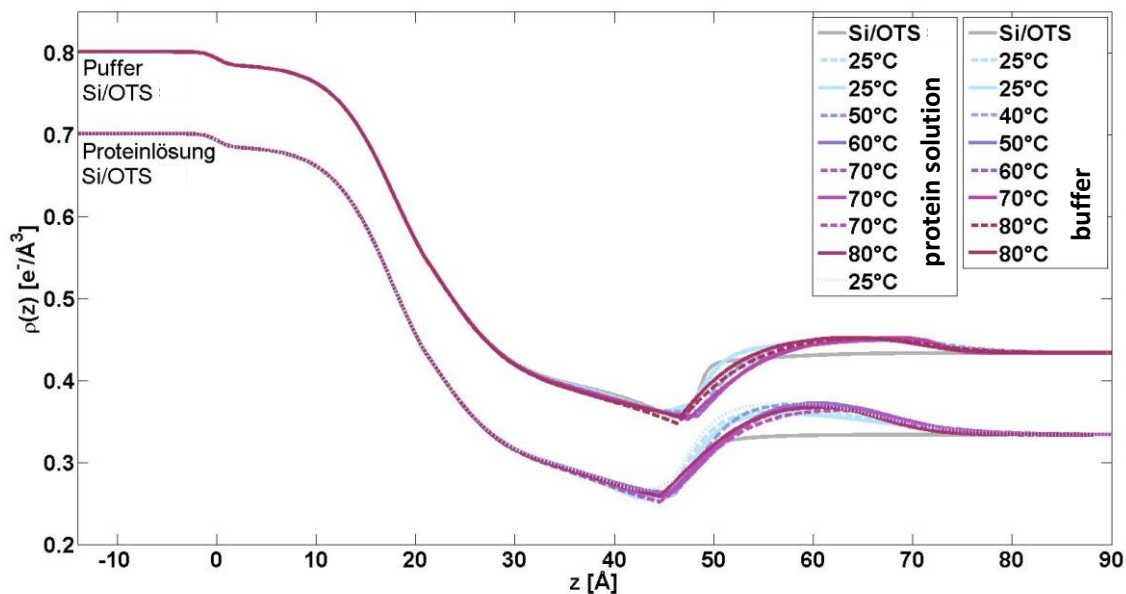
Fig. 3: Temperature dependent electron-density profiles (electron density ρ vs the depth *z)* of Apolipoprotein A1 at a hydrophobic interface in protein solution and in buffer. The profiles are shifted by a constant value for clarity.

The EDP include the electron density of Si, SiO_2, OTS headgroup, OTS tailgroup, depletion layer and protein layer. The thickness of the protein layer is 20 Å thus, slightly smaller than the smallest diameter of ApoA1. This indicates a deformation of the tilted ring at the hydrophobic interface. An explanation for this behavior could be a maximization of the contact area between the hydrophobic inner part of the ring and the hydrophobic interface. Similar results were found for ApoA1 adsorption at the liquid/air interface [5, 6]. With increasing temperature, the thickness does not change significantly, whereas the slope at z=50 Å, which is the proteins contact line to the wafers surface decreases with increasing temperature. This trend is slightly more pronounced in protein solution. A decreasing slope indicates an increasing roughness at the interface. *Gursky at al* [7] observed in a calorimetric study a broad signal between 25°C and 90°C for ApoA1. This indicates a conformational transition of ApoA1 over several non-separated states with increasing temperature. These conformational changes could be present also for the adsorbed protein and then explain the increased roughness.

In comparison to previous experiments [6], ApoA1 do neither adsorb in protein solution nor desorb in buffer solution with increasing temperature.

In summary, an adsorption and a deformation of ApoA1 at the hydrophobic solid/liquid-interface was observed. The temperature dependent behavior indicates further conformation transitions of the adsorbed protein.

[1] D. J. Voet, J. G. Voet, und C. W. Pratt (2002) *Lehrbuch der Biochemie*. Wiley-VCH Verlag GmbH & Co. KGaA, 2. Edt.
[2] M. Paulus et al. (2008) J. Synchrotron Radiat., 15(6), pp. 600–605.
[3] I. Kiesel et al. (2014) Langmuir, 30(8), pp. 2077–2083.
[4] M. Mezger et al. (2006), PNAS, 103(49), pp. 18 401–18 404.
[5] M. Kampmann (2014), *Diplomarbeit, Adsorption von Apolipoprotein an der Flüssigkeits-Gas-Grenzfläche*,
        TU Dortmund
[6] I. Kiesel (2014), *Dissertation, In-situ Untersuchung von Proteinen an Grenzflächen mit oberflächensensitiven
        Röntgenstreumethoden*, TU Dortmund
[7] O. Gursky und D. Atkinson (1996), PNAS, 93(7), pp. 2991–2995.

Protein film structure of wild type hydrophobins and variants at solid/liquid interfaces

Hendrik Hähl[1], Jonas Heppe[1], Christian Spengler[1], Michael Klos[1], and Karin Jacobs[*1]

[1]*Experimentalphysik, Universität des Saarlandes, 66123 Saarbrücken*

[*]email: k.jacobs@physik.uni-saarland.de

In a biological environment, proteins are usually the first molecules covering new interfaces. Especially on solid/liquid interfaces, they form a conditioning film for further biofilm development, a crucial process in medicine as well as in biotechnical applications. We aim at controlling the protein film formation by characterizing and controlling the interactions present between all involved partners, *i.e.* proteins, solution and substrate surface. In previous studies, we could already determine the substrate's influence on the kinetics of the protein adsorption as well as on the final film structure [1, 2]. Here, we aim at characterizing the effect of changes in the protein/protein interactions by measuring the adsorbate's film structure using *in situ* X-ray reflectivity (XRR).

For this purpose, a special class of proteins, hydrophobins, appears to be an ideal candidate: They are highly amphiphilic and hence adsorb in a well-defined orientation on interfaces [3, 4]. Moreover, the employed class members HFBI and HFBII from *Trichoderma reesei* are quite small (7.5 and 7.2 kDa), compact, and conformationally very stable. Therefore these proteins do not denature upon adsorption – even on very hydrophobic surfaces – and form very dense adsorbates, yielding a high electron density contrast compared to commonly used model proteins. Additionally, using genetically engineered mutants of HFBI with different charge distribution or with attachments of different sizes allows for the study of the effects of steric and electrostatic interaction between the proteins.

In previous experiments, we used native silicon wafers and silicon wafers covered with self-assembled monolayers (SAM) of silanes with hydrophobic ends (octadecyltrichlorosilane, OTS) as models for hydrophilic and hydrophobic surfaces. As these surfaces do not only differ in hydrophobicity but also in their structure (SAM vs. amorphous silica), a third type of surface was needed to be able to discriminate between hydrophobicity and structural effects when comparing protein films on different surfaces. As an intermediate, we tested a silane SAM featuring a C-C double bond at the surface (undecenyltrichlorosilane, UDTS). These were then oxidized resulting in a negatively charged and hence hydrophilic surface [5]. Moreover, the silane SAMs have a similar electron density as water, which is the ambient phase in the *in situ* XRR experiments. Therefore, the contrast of the protein film should be enhanced in comparison to films on the silicon oxide surface.

The XRR experiments were performed at DELTA's beamline 9 at a photon energy of 27 keV. Substrates were placed in a teflon liquid cell at room temperature. They were immersed in acetate buffer solution at a pH of 5. Protein solution was injected into the cell such that the protein concentration was 5 μM. Each sample was measured before protein injection and several times afterwards to ensure stable measurement conditions (*i.e.* a stable protein film). Protein films of HFBI, HFBII, three charge variants of HFBI, and two size variants of HFBI
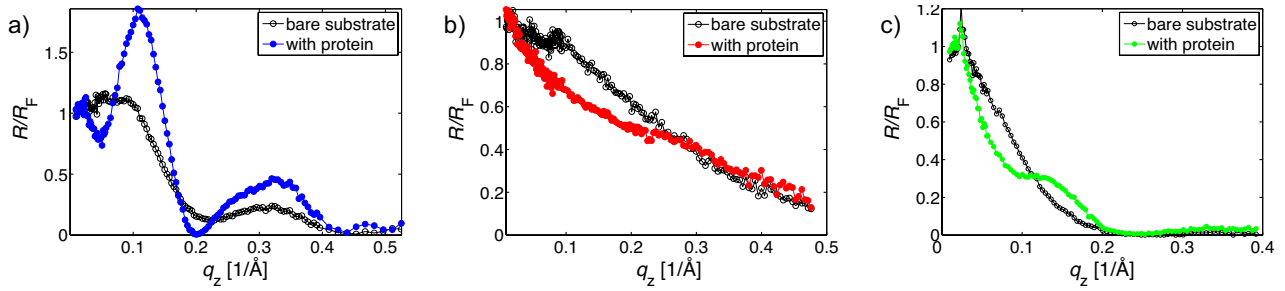
Figure 1: Reflectivity data of the employed substrates in buffer solution before and after injection of HFBII: a) OTS covered silicon substrate, b) silicon wafer with native silicon oxide surface, and c) oxidized UDTS on silicon substrate. The data are normalized to the Fresnel reflectivity R_{F}, *i.e.* here the reflectivity of a smooth silicon/water interface.

were studied on OTS, SiO_2 and oxidized UDTS.

In all experiments, a change in the sample's reflectivity due to the formed protein layer could clearly be identified. Even without a modeling procedure, clear differences in the structure of protein films of different mutants are observable, *i.e.* differences in the protein film arising from changes in the mutual protein interactions were detected using *in situ* XRR. The quantitative changes in the film structures will be determined by modeling these data. Moreover, also the effect of different substrate hydrophobicity and structure can only be seen after the modeling. However, even for HFBII, which is the protein forming the films with the poorest contrast in our study, films can be detected on all three substrates (see figure 1) and the supposed enhancement of the film's 'visibility' when changing from SiO_2 to UDTS as substrate was also found. Therefore, the UDTS substrate seems suitable also for further studies with even less dense protein films.

References

[1] M. Bellion, L. Santen, H. Mantz, H. Hähl, A. Quinn, A. Nagel, C. Gilow, C. Weitenberg, Y. Schmitt and K. Jacobs, *J Phys-Condens Mat*, 2008, **20**, 404226.

[2] H. Hähl, F. Evers, S. Grandthyll, M. Paulus, C. Sternemann, P. Loskill, M. Lessel, A. K. Huesecken, T. Brenner, M. Tolan and K. Jacobs, *Langmuir*, 2012, **28**, 7747–7756.

[3] M. B. Linder, *Curr Opin Colloid Interface Sci*, 2009, **14**, 356–363.

[4] C. Peng, J. Liu, D. Zhao and J. Zhou, *Langmuir*, 2014, **30**, 11401–11.

[5] S. Wasserman, Y. Tao and G. Whitesides, *Langmuir*, 1989, **5**, 1074–1087.

In situ protein insertion into supported lipid bilayers

Hendrik Hähl[1], Isabelle Möller[1], Irena Kiesel[2], Dorinel Verdes[1], and Stefan Seeger[*,1]

[1] *University of Zurich, Institute of Physical Chemistry, Winterthurerstrasse 190, CH-8057 Zurich, Switzerland* and [2] *Fakultät Physik/DELTA, TU Dortmund, D-44221 Dortmund*

[*]email: sseeger@pci.uzh.ch

Introduction

α-synuclein is a small protein abundant in human neuronal brain cells. It has attracted large interest as the appearance of large α-synuclein aggregates is strongly correlated with the onset of Parkinson's disease. Despite many studies focussing on this protein, its precise biological function is still not known, but it is believed that it plays an important role in vesicle dynamics at the synapse. In its natural form in solution the protein is believed to be unfolded; inserted in micelles (and supposedly also in bilayers) it adopts an α-helical form. Many studies suggest that its toxicity stems from a misfolding into a β-sheet conformation and a subsequent fibrillation and aggregation [1]. A fibrillation starting at the outer cell membrane may cause its disruption and lead to cell death [2].

In this study, we focus on the adsorption of α-synuclein monomers to solid supported lipid bilayers. Thereby we aim at the exact position of the protein with respect to the bilayer as well as the change of the bilayer properties due to the adsorption.

Experiments and Results

To study *in situ* the insertion of the proteins into the lipid bilayer, the X-ray reflectivity setup at the BL9 of the synchrotron source DELTA was used [3] operated at a photon energy of 27 keV. As solid support for the bilayers, we used silicon wafers cleaned in piranha solution and stored in ultra pure water until usage. The bilayer was prepared on these substrates directly in the measurement cell following a slightly modified protocol by Richter *et al.* [4] using the fusion of vesicles at the surface. The vesicle solution employed for the bilayer construction comprised the lipids DOPC (1,2-dioleoyl-*sn*-glycero-3-phosphocholine) and DOPS (1,2-dioleoyl-*sn*-glycero-3-phospho-L-serine) in a ratio of 65:35. After completion of the bilayer construction, the solution was exchanged by lipid-free phosphate buffered saline (PBS) with pH adjusted to 7.4. The proteins for this study had been recombinantly produced in *E. coli* and purified in the group of R. Riek at the ETH Zurich. We employed the protein in its wild type (WT) form as well as the modified species E57K, which is known to be a very toxic mutant [5].

After the preparation of the bilayer, reference measurements of the pure bilayer were performed. Protein solution was then injected resulting in a final protein concentration of 10 μM in the cell. After some equilibration time, several reflectivity scans were recorded until no changes could be observed at this time scale. The samples were measured again in time intervals of several hours. Beside the experiments with protein in the solution, a measurement series with the blank bilayer was also performed.

Exemplary, the recorded data for the time series with E57K insertion is given in figure 1a). For the analysis, all data were modeled using the 'effective density' approach [6] with a 6 layer representation of the sample: Additionally to the native SiO_2 layer of the substrate, the lipid bilayer was divided into lipid head and lipid tail groups as well as a layer of decreased electron density dividing the two lipid layers. The resulting electron density profiles (figure 1b) vary slightly for each bilayer but are well in line with literature values.

After protein insertion, the recorded reflectivities show an increased wavelength of the fringes. This shift cannot be explained by an additional layer on top of the bilayer. Instead, changes in the model parameters describing the bilayer itself lead to a very good description of the experimental values. This hints at the fact that the protein inserts into the bilayer. Moreover, the change in the wavelength of the fringes, which was not found for the reference time series with a bilayer without proteins, is explained
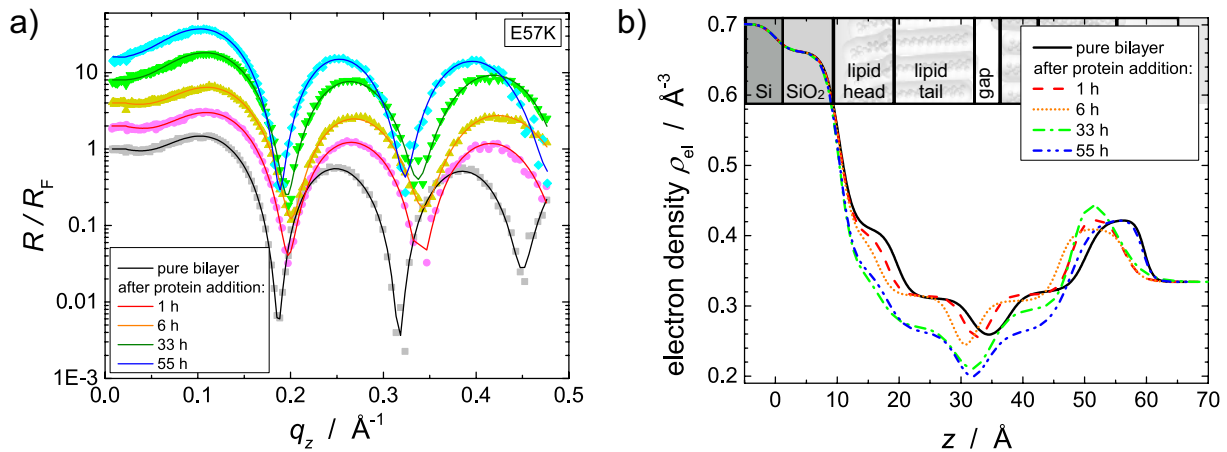
Figure 1: a) Recorded reflectivity data of the supported lipid bilayer before and after the protein injection. Data are normalized to the Fresnel reflectivity R_F of the Si substrate. Subsequent measurements are shifted along the ordinate. b) EDP's as received from the refinement procedure of the data. In the upper part, the layer model used for data modeling is shown.

by an overall decrease of the bilayer thickness of about 7%. This decrease may be interpreted as a flattening of the bilayer upon the insertion of the protein in the head group region. Another remarkable feature in the data of all experiment series is the increase in the amplitude of the fringes with time, which is less pronounced in the case of the blank bilayer. This corresponds to a contrast increase between head and tail groups in the model. A first explanation might be that the bilayer thins out over time. Yet, this will be subject to further analysis.

Conclusion

Using high energy X-ray reflectivity, the insertion of α-synuclein into lipid bilayers was measured. It could be shown that the protein inserts into the bilayer while at the same time flattens it. Moreover, the time series show a decrease in bilayer density, yet no destruction of the bilayer due to the protein monomers.

References

[1] L. Breydo, J. W. Wu and V. N. Uversky, *Biochim Biophys Acta*, 2012, **1822**, 261–85.

[2] N. P. Reynolds, A. Soragni, M. Rabe, D. Verdes, E. Liverani, S. Handschin, R. Riek and S. Seeger, *J Am Chem Soc*, 2011, **133**, 19366–19375.

[3] M. Paulus, R. Fendt, C. Sternemann, C. Gutt, H. Hovel, M. Volmer, M. Tolan and K. Wille, *J Synchrotron Rad*, 2005, **12**, 246–250.

[4] A. Richter, C. Yu, A. Datta, J. Kmetko and P. Dutta, *Phys Rev E*, 2000, **61**, 607–615.

[5] B. Winner, R. Jappelli, S. K. Maji, P. A. Desplats, L. Boyer, S. Aigner, C. Hetzer, T. Loher, M. Vilar, S. Campioni, C. Tzitzilonis, A. Soragni, S. Jessberger, H. Mira, A. Consiglio, E. Pham, E. Masliah, F. H. Gage and R. Riek, *P Natl Acad Sci USA*, 2011, **108**, 4194–9.

[6] M. Tolan, *X-ray scattering from soft-matter thin films*, Springer, Heidelberg, 1999.

In-situ XRR study on photocleavable PS-*hv*-PEO nanoporous thin films

S. Altinpinar[1], P. Schuchart[1,2], W. Ali[1], Pinar Yildiz[1], H. Zhao[3], C. Sternemann[4], M. Paulus[4],
P. Theato[3], M. Tolan[4] and J. S. Gutmann[1,2,5]

[1]Institute for Physical Chemistry, University of Duisburg-Essen, 45141 Essen, Germany
[2]DTNW gGmbH, University of Duisburg-Essen, 47057 Duisburg, Germany
[3]Institute for Technical and Macromolecular Chemistry, University of Hamburg, 20146 Hamburg, Germany
[4]DELTA, University of Dortmund, 44221 Dortmund, Germany
[5]CENIDE, University of Duisburg-Essen, 47057 Duisburg, Germany
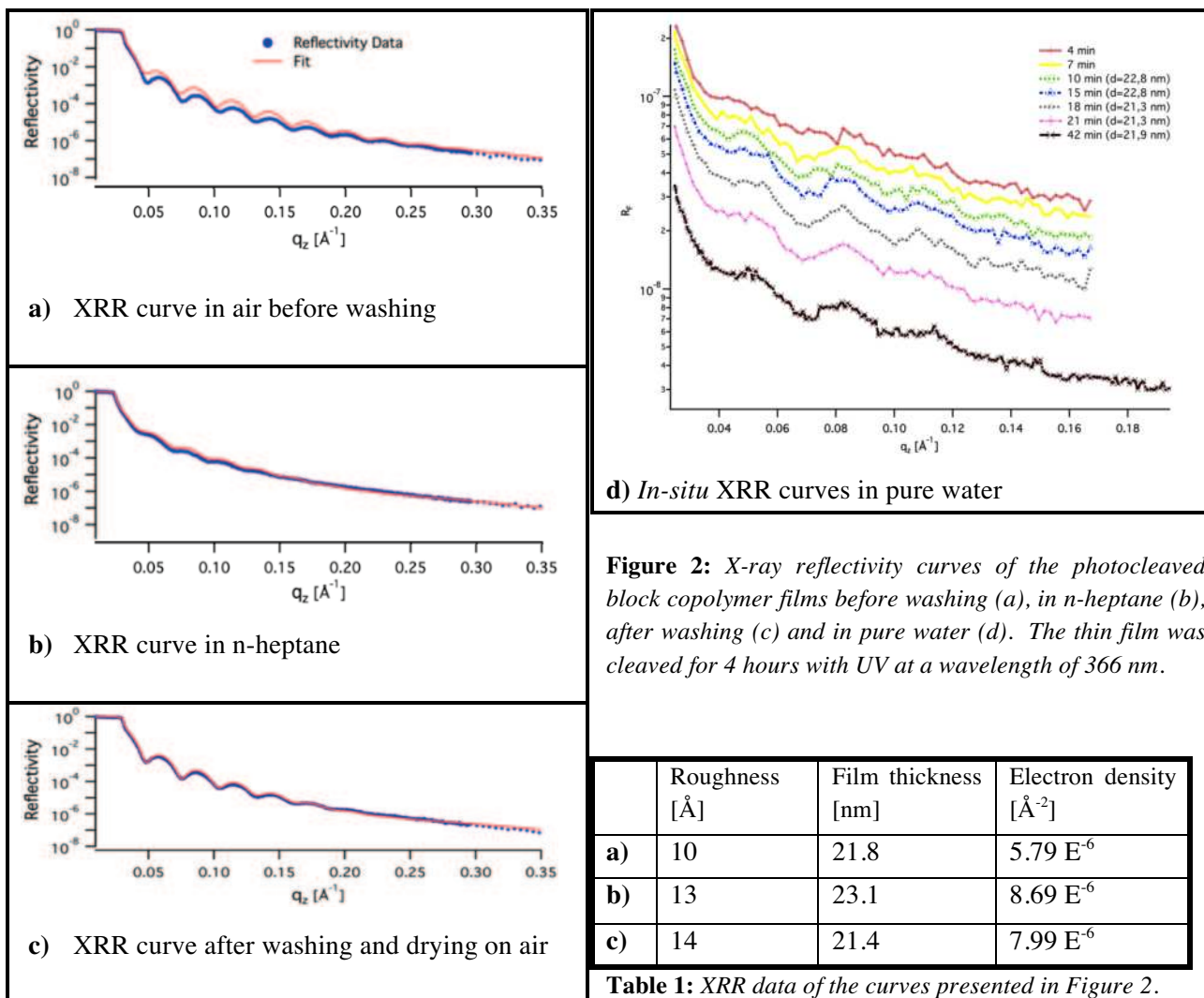
sedakat.altinpinar@gmail.com

The utilization of the bottom up approach to fabricate regular arrays of nanostructures patterning from block copolymer will open the possibility to use this patterning in a system such as a polymeric membrane or a template for nanostructure materials. Thus, exploring the quantum efficiency of photocleavage and the diffusive transport of the cleaved domain out of the system are of strategic importance of meeting these future applications. Upon the UV irradiation, the photocleavable part in a highly ordered PS-b-PEO thin film will be removed out of the system by choosing an appropriate solvent leaving a nanoscopically-patterned. Thereby, it is important to figure out the best washing solvent and the best washing time for the selective degradation of the core material. In favor of this, the in-situ formation of nanoporous during the washing process in ultra pure water was measured using X-Ray Reflectivity (XRR) technique.
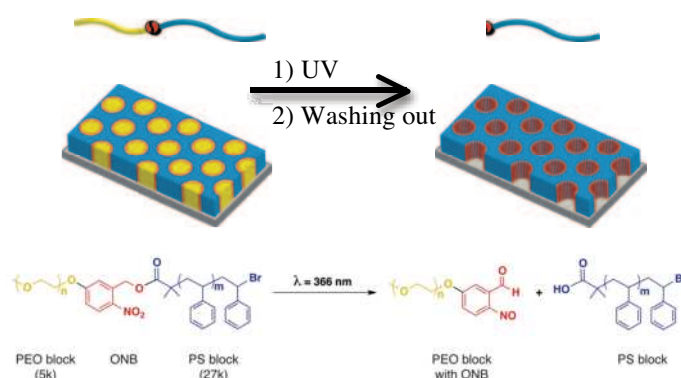
Figure 1: *Schematic representation of the self-assembly of photocleavable block copolymers and the subsequent removal of one domain upon photo cleavage and washing.*

The X-ray reflectivity measurements were investigated at the Bl9 beamline at the synchrotron light source DELTA in Dortmund. By XRR we proposed to study the kinetic of removal during the immersion of a photocleaved sample into pure water solution, by probing the structure perpendicular to the surface. To reach a resolution for short times and for penetrating the liquid area, we used hard x-rays in the energy range of 27 keV (0,4 Å). In order to be able to record the fully kinetics, the sample was first aligned in n-heptane. Afterwards, pure water was added into the sample cell. The scan in a q_z range of 0.01-0.167 was repeated until reaching the time scale, where we expected the process to be completed. X-ray reflectivity studies on air were performed prior to in-situ measurements and as well as after it.

For the analysis, the scans in air before and after washing and also the scan in n-heptane were fitted using

the Parratt algorithm. To distinguish the oscillation in the reflectivity curves, the Fresnel reflectivities for the measurements in pure water were calculated.

a) XRR curve in air before washing

b) XRR curve in n-heptane

c) XRR curve after washing and drying on air

d) *In-situ* XRR curves in pure water

Figure 2: *X-ray reflectivity curves of the photocleaved block copolymer films before washing (a), in n-heptane (b), after washing (c) and in pure water (d). The thin film was cleaved for 4 hours with UV at a wavelength of 366 nm.*

	Roughness [Å]	Film thickness [nm]	Electron density [Å^{-2}]
a)	10	21.8	5.79 E^{-6}
b)	13	23.1	8.69 E^{-6}
c)	14	21.4	7.99 E^{-6}

Table 1: *XRR data of the curves presented in Figure 2.*

Via XRR measurements we studied the film thickness and roughness of highly ordered block copolymer films and the kinetic of PEO block removal at different washing times for ultra pure water solution. From the reflectivity curve (Figure 2a and 2b) we can conclude that the film thickness and as well as the roughness increase after adding n-heptane into the sample cell, although n-heptane is not a good solvent for both PS and PEO. But, after n-heptane is exchanged with ultra pure water in the sample cell, we can observe that the swelling is reversible and the film thickness decrease with increasing washing time, as shown in Figure 2d. Furthermore, on can reason that after 10 minutes washing in water the film becomes smooth and after 15 minutes the roughness increase again. This can be traced back to the removal of the pore material PEO, which goes into solution after 15 minutes washing with ultra pure water. After drying and scanning the sample in air, the distinct change in the roughness can be shown in Figure 2c.

References

1   H. Zhao, W. Gu, E. Sterner, T. P. Russell, E. B. Coughlin and P. Theato, Macromolecules 2011, 44, 6433-6440.

2   M. Paulus, D. Lietz, C. Sternemann, K. Shokuie, F. Evers, M. Tolan, C. Czeslik and R. Winter, J. Synchrotron Rad. 2008, 15, 600–605.

Hard X-ray spectroscopy

X-ray absorption studies of gold-containing complexes

F. Severin[a], C. Helmbrecht[a], D. Lützenkirchen-Hecht[b], R. Wagner[b], W. Frank[a]

[a] Institut für Anorganische Chemie und Strukturchemie II, Heinrich-Heine-Universität Düsseldorf, Universitätsstr. 1, 40225 Düsseldorf, Germany.
[b] Fachbereich C-Physik, Bergische Universität Wuppertal, Gaußstr. 20, 42097 Wuppertal, Germany

The interest in the chemistry of gold has increased considerably in recent decades for several reasons. First of all, it is of fundamental importance to understand and quantify relativistic and correlation effects which are especially important for the chemistry of gold. In addition, several new gold complexes have been synthesized in a great variety of structures and stoichiometries with different ligands (see e.g. [1-7]), and the opportunity to prepare nanosized materials containing gold with interesting catalytic, optical or luminescent properties and potential applications in nanoscale devices has further accelerated the rapid growth of this field. Here we want to elucidate the structure and the electronic structure of different gold complexes from EXAFS and XANES measurements. The reference compounds $NaAuCl_4$, $Au(tht)Cl$ (tht = tetrahydrothiophene = $(CH_2)_4S$), $Au(tht)Cl_3$, $Au(PPh_3)Cl$ (PPh_3 = triphenylphosphine = $P(C_6H_5)_3$), $Au(PPh_3)Cl_3$ and $Au_9(PPh_3)_8(NO_3)_3$ were investigated at the Au L_3 edge (11.919 keV) using synchrotron radiation from DELTA beamline 10 [8]. The absorption spectra were collected in the transmission mode using N_2- and Ar-filled ionization chambers as detectors for the incident and transmitted intensities, and in fluorescence mode, where the excited radiation is detected by a peltier-cooled Si drift-diode and a multichannel analyzer (Amptek, Bedford, USA). Averaged and normalized spectra from the investigated sample are displayed in Fig. 1. As can be seen, the Au^I-species, $Au(tht)Cl$ and $Au(PPh_3)Cl$, in addition to the polynuclear complex $Au_9(PPh_3)_8(NO_3)_3$ generally show only weak white line intensities, while the Au^{III}-compounds $NaAuCl_4$, $Au(tht)Cl_3$ and $Au(PPh_3)Cl_3$ give strong white line features, so that Au^I and Au^{III} can easily be distinguished. Furthermore, the EXAFS of the Au^{III} - compounds has a larger amplitude compared to Au^I.
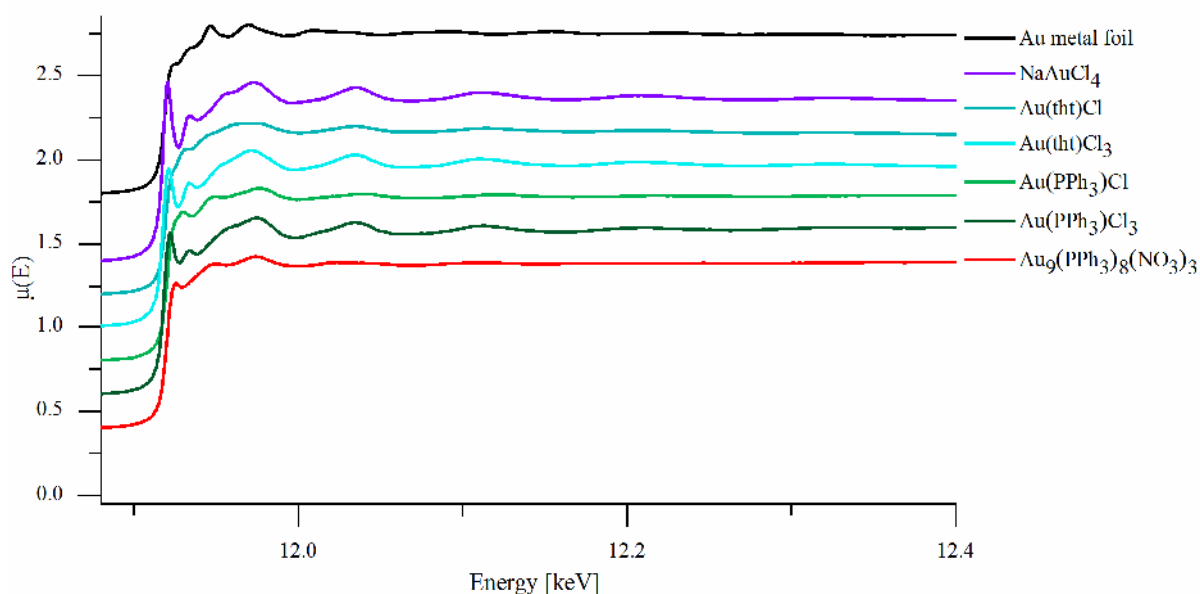
Fig. 1: Transmission mode X–ray absorption spectra of different Au^I, Au^{III} reference compounds and a polynuclear Au cluster as indicated. All spectra are calibrated with respect to the edge of a gold metal foil at 19.919 keV and are shifted vertically for a better comparison.

The EXAFS data processing were performed using the Demeter software package[9], and included a background subtraction, transformation into k-space and fitting of the first coordination shells using phase and amplitude functions calculated by FEFF [10]. More details are given in [11].

Typical fit results obtained for $Au(PPh_3)Cl$ are presented in Fig. 2. As can be seen, the fit with a phosphorus and a chlorine atom in the first shell fit nicely to the experimental data. The obtained interatomic distances are R_{Au-P} = 2.228 Å and R_{Au-S} = 2.287 Å, the deviations to the distances calculated from crystallographic data are about 0.005 Å. Thus, it can be concluded that the applied procedures may give results of similar precision for unknown mononuclear gold compounds.
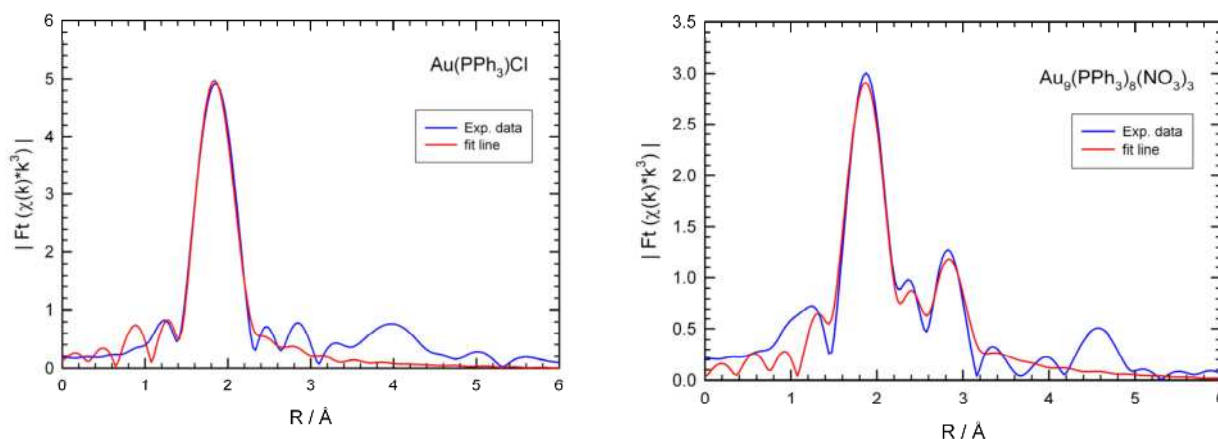
Fig. 2: Magnitude of the Fourier-transform of the k^3-weighted EXAFS function $\chi(k)*k^3$ for $Au(PPh_3)Cl$ (left) and the polynuclear Au_9-cluster $Au_9(PPh_3)_8(NO_3)_3$ (right).

In the case of the polynuclear Au_9-cluster, however, the fitting procedure is much more complex because the first four coordination spheres have to be included to model the radial distribution function, i.e. several different atoms with various interatomic distances contribute to the signal. The experimental data of this compound only provide useful structure information for interatomic distances up to 3 Å. The fit results gave an Au-P coordination in a distance of 2.300 Å, and four Au-Au bonds with 2.47 Å, 2.59 V and 2*2.71 Å. In the future other compounds will be measured in order to estimate the information content of such measurements.

References
[1] H. Schmidbaur, K.C. Dash, Adv. Inorg. Chem. Radiochem. 25 (1982) 239.
[2] A. Laguna, M. Laguna, Coord. Chem. Rev. 193–195 (1999) 837.
[3] R.J. Puddephatt, Coord. Chem. Rev. 216–217 (2001) 313.
[4] A. Vogler, H. Kunkely, Coord. Chem. Rev. 219–221 (2001) 489
[5] F. Mohr, D.J. Eisler, C.P. McArdle, K. Atieh, M.C. Jennings, R.J. Puddephatt, J. Organomet. Chem. 670 (2003) 27
[6] O. Neumann, A. S. Urban, J. Day, P. Nordlander, N. J. Halas, ACS Nano 7 (2013) 42.
[7] S. Haas, R. Fenger, E. Fertitta, K. Rademann, J. Appl. Crystallogr. 46 (2013) 1353.
[8] D. Lützenkirchen-Hecht, R. Wagner, S. Szillat, A.K. Hüsecken, K. Istomin, U. Pietsch, R. Frahm. J. Synchrotron Rad. 21 (2014) 819.
[9] B. Ravel, M. Newville, J. Synchrotron Rad. 12 (2005) 537.
[10] A.L. Ankudinov, A.I. Nevsvizhskii, J.J. Rehr, Phys. Rev. B 67 (2003) 115120.
[11] F. Severin, Bachelor-Thesis, Heinrich-Heine-Universität Düsseldorf (2014).

XANES investigations of ligand-stabilized gold nanoclusters

C. Helmbrecht[a], D. Lützenkirchen-Hecht[b], R. Wagner[b], W. Frank[a]

[a] Institut für Anorganische Chemie und Strukturchemie II, Heinrich-Heine-Universität Düsseldorf, Universitätsstr. 1, 40225 Düsseldorf, Germany.
[b] Fachbereich C-Physik, Bergische Universität Wuppertal, Gaußstr. 20, 42097 Wuppertal, Germany

Gold nanoparticles in a size range from 2 to 100 nm have been well studied and widely applied in the past (see e.g. [1-3]). Significantly smaller gold species with a size close to the Fermi wavelength of the conduction electrons have gained much research interest (see e.g. [4, 5]) because of their intriguing properties, but the structure-property-relationships of gold nanoclusters (AuNC) have still not been fully clarified. In any case, these small gold nanoclusters need protecting capping molecules in order to prevent agglomeration and growth to larger structures. Their synthesis requires an excess of ligands and results in concentrations of the AuNC around 10 ppm. These conditions substantially complicate any investigation of the clusters' structure or electronic properties. In particular nano-sized species smaller than about 3-5 nm can no longer be reliably determined by X-ray diffraction, and thus X-ray absorption spectroscopy (XAS) with its inherent sensitivity towards the atomic short range order structure was applied in past experiments. In the present study, we investigate additional Au^I and Au^{III} reference compounds in order to provide a better understanding of the gold nanoclusters' near edge data.

The reference compounds $NaAuCl_4$, $Au(tht)Cl$, $Au(tht)Cl_3$, $Au(PPh_3)Cl_3$, $Au_9(PPh_3)_8(NO_3)_3$ were investigated with XANES at the Au L_3-edge using synchrotron radiation from DELTA beamline 10. The absorption spectra were collected in the transmission mode using ionization chambers as detectors, and in fluorescence, where the excited radiation is detected by a peltier-cooled Si drift-diode and a multichannel analyzer (Amptek, Bedford, USA). The averaged and normalized spectrum of the AuNC solution is compared to these Au reference compounds with different valences (Fig. 1). In agreement to the literature the received data do not offer a linear shift between edge position and chemical valence as usually observed. Pantelouris et $al.$ noticed a linear shifting of the absorption edge to higher energy with increasing valence at the L_I–edge, but not in the equivalent Au L_{III} XANES spectra [6]. The data have to be deconvoluted because of a superposed peak onto the absorption edge, which can be related to 5d–6s–hybrid orbitals according to Choy et $al.$ [7]. In accordance to the literature a linear relationship between the Au valences of the studied compounds and their edge energies was confirmed executing a detailed curve fitting (Fig. 2). Corresponding to the linear regression of edge energy of the reference compounds, the Au oxidation state for the AuNC could be deduced from the absorption edge at 11.9213 keV as derived from the XANES deconvolution. Accordingly, the AuNC offer an oxidation state of about 0.2.

Fluorescence spectroscopic experiments of the AuNC in the visible range suggest that they mainly consist of five gold atoms. In the light of these results a more detailed comparison of the X–ray absorption spectra of the investigated polynuclear clusters reveals an increase in the Au L_{III} white–line intensity with decreasing cluster size (Fig. 3). Similar results were obtained for gold nanoparticles with sizes of $4.0 < 2.4 < 1.6$ nm by Zhang et $al.$ and cluster sizes of Au_{25}, Au_{38} and Au_{144} by MacDonald and co–workers [8, 9]. They were attributed to d–band vacancies caused by an electron transfer from Au to the ligand. Taking into account the Au_{11} cluster from literature, we found out that the cluster size correlates linearly with the absorption coefficient and the integral of the Pseudo–Voigt function of the examined small polynuclear cluster, respectively (Fig. 3).
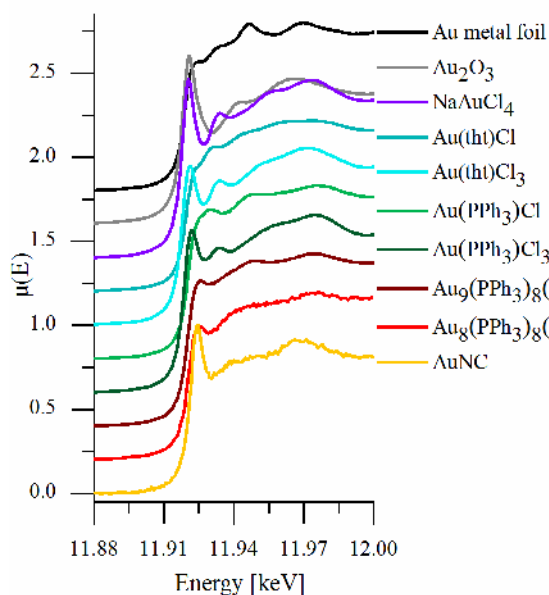
Fig. 1: Fluorescence mode X–ray absorption near edge spectra of gold nanoclusters (AuNC) in comparison to reference spectra obtained from different Au^I, Au^{III} and polynuclear Au clusters. All spectra are calibrated with respect to the Au metal foil at 19.919 keV and are shifted vertically for a better comparison.
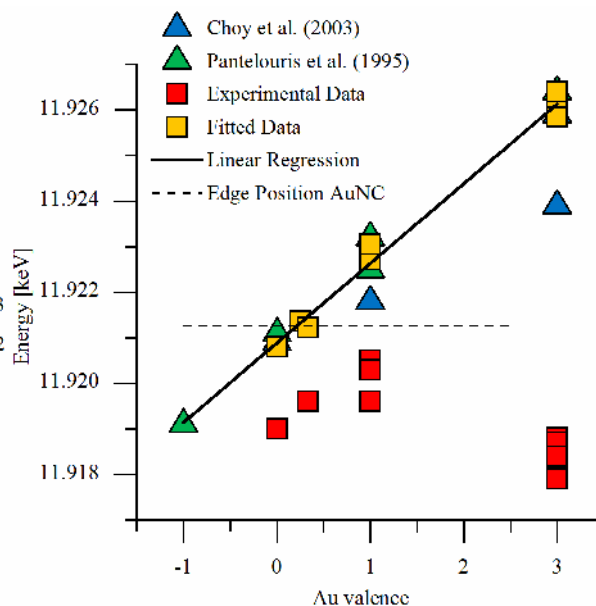
Fig. 2: Experimental and fitted edge positions as a function of the formal Au valence in comparison to the literature. The determination of the Au valence in AuNC can be estimated from the intersection of the determined edge energy for AuNC and the linear regression of the reference data as indicated.
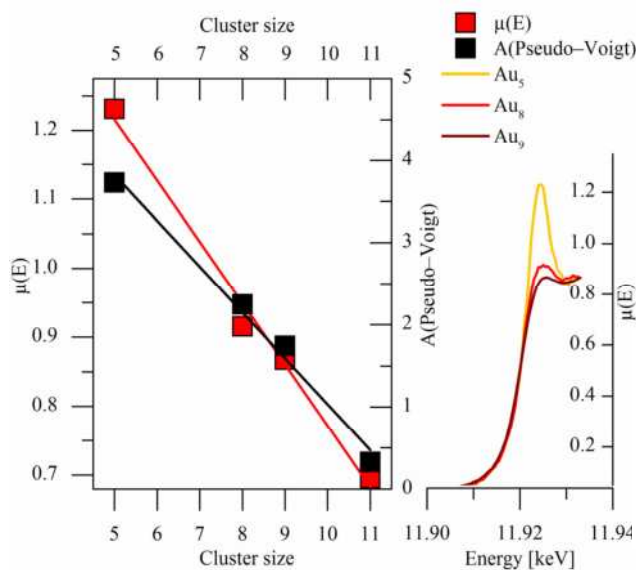
Fig. 3:
Linear relationship between cluster size and absorption coefficient μ and integrated area A of the fitted Pseudo–Voigt–function of investigated polynuclear clusters.

References

[1] G. Schmid, B. Corain. Eur. J. Inorg. Chem. (2003) 3081.

[2] M.-C. Daniel, D. Astruc. Chem. Rev. 104 (2004) 293.

[3] A. Schwartzberg, J. Z. Zhang. J. Phys. Chem. C 112 (2008) 10323.

[4] X. Yang, L. Gan, L. Han, D. Li, J. Wang and E. Wang, Chem. Commun. 49 (2013) 2302.

[5] X. Wen, P. Yu, Y.-R. Toh, X. Ma, S. Huang, J. Tang, Nanoscale 5 (2013) 10251.

[6] A. Pantelouris, G. Kueper, J. Hormes, C. Feldmann, M. Jansen, J. Am. Chem. Soc. 117 (1995) 11749.

[7] J. Choy, Y. Kim, J. Phys. Chem. B 107 (2003) 3348.

[8] P. Zhang, T. Sham, Phys. Rev. Lett. 90 (2003) 245502.

[9] M. A. MacDonald, P. Zhang, H. Qian, R. Jin, J. Phys. Chem. Lett. 1 (2010) 1821.

[10] R. E. Benfield, D. Grandjean, M. Kröll, R. Pugin, T. Sawitowski, G. Schmid, J. Phys. Chem. B 105 (2001) 1961.

XANES/EXAFS studies of barium aluminate (BaAl$_2$O$_4$) doped with Cr

D. Lützenkirchen-Hecht[a], B. Gržeta[b], M. Vrankić[b], R. Wagner[a]

a) Fachbereich C - Physik, Bergische Universität Wuppertal, Gaußstr. 20, 42097 Wuppertal, Germany.
b) Ruđer Bošković Institute, Division of Materials Physics, Bijenička cesta 54, 10000 Zagreb, Croatia.

Barium aluminate (BaAl$_2$O$_4$) is widely used in the field of optical communication and electronics [1]. In particular, BaAl$_2$O$_4$ exhibits good luminescence properties when it is doped/co-doped with rare earth or transition metal cations [2, 3]. Europium doped BaAl$_2$O$_4$ is already used as a luminescent material with emission in the red spectral range. Chromium is another, low cost activator and Cr^{3+}-doped systems are already used in modern technologies, e.g. for the production of solid-state lasers. However, the literature data on optical properties of Cr-doped BaAl$_2$O$_4$ are very rare, while structural data are completely missing. In this context, we have conducted XANES measurements at the absorption edges of the dopant and the host elements in order to elucidate for the first time the mechanism of incorporation of Cr in the BaAl$_2$O$_4$ structure, as well as to understand the origin of the optical/ luminescence properties of Cr-doped barium aluminate. Powder samples of undoped BaAl$_2$O$_4$ and BaAl$_2$O$_4$ doped with 4, 6 and 8 at.% Cr (in relation to Al) were prepared by a hydrothermal method, additionally annealed at 1100 ºC for 4h and characterized by X-ray diffraction at room temperature. X-ray diffraction showed that the undoped sample was phase-pure BaAl$_2$O$_4$ without any impurities, while the doped samples contained a BaAl$_2$O$_4$-type phase (space group $P6_3$) as a dominant phase and small amounts of BaCrO$_4$ as an impurity phase [4]. The Cr K-edge X-ray absorption experiments on doped samples were performed at DELTA beamline 10 [5], making use of the Si(111) channel cut monochromator, ionization chambers for the incident and transmitted intensities, and a silicon drift diode with a multichannel analyzer for the detection of the fluorescence from the samples.

A major problem in X-ray absorption measurements arises from the overlap of the Ba L-edges and the Cr K-edge. More specifically, the energy of the Ba L_1-edge and the Cr K-edge are identical with 5989 eV, so that a simple transmission mode EXAFS/XANES experiment can hardly be analysed. Due to the low concentration of the dopants of some few atomic %, fluorescence mode X-ray absorption spectroscopy is an appropriate tool, however also the fluorescence X-ray emissions substantially overlap as can be seen in Fig. 1(a) with Ba L-lines at about 4460, 4830, 5160 and 5530 eV, and Cr K-lines at 5410 and 5950 eV.
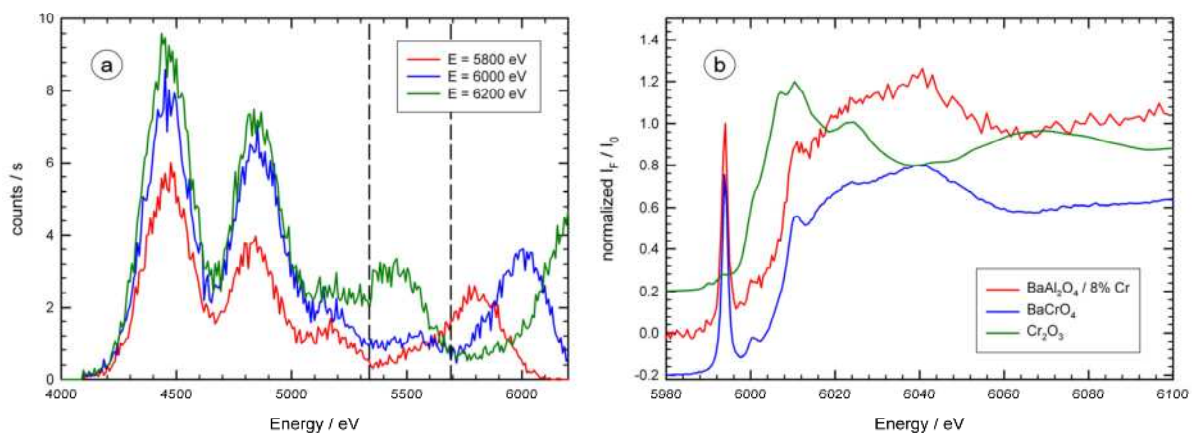
Fig. 1: (a) X-ray fluorescence spectra from BaAl$_2$O$_4$ sample doped with 8 at.% Cr for different excitation energies in the vicinity of the Cr K-edge / Ba L_1-edge. Emissions between ca. 5350 eV and 5700 eV are mainly caused by the Cr-fluorescence. **(b)** Cr K-edge near edge spectrum of BaAl$_2$O$_4$ sample doped with 8 at.% Cr in comparison to K-edge spectra of barium chromate (BaCrO$_4$) and Cr$_2$O$_3$.

Using a region of interest from 5350 to 5700 eV, the influence of Ba on the Cr K-edge spectra could be minimized. Spectra of reasonable quality could be obtained after averaging over 5-8 scans as can be seen in Fig. 1(b), where the near edge spectrum of $BaAl_2O_4$ doped with 8 at.% Cr is compared to those of $BaCrO_4$ and Cr_2O_3 as reference spectra for Cr^{6+} and Cr^{3+}, respectively. As can be already deduced from the raw data, Cr incorporated in the doped samples seems to be in a 6+ state, and the coordination is mainly tetrahedral, as can be anticipated from the intense pre-edge peak at 5993 eV and the edge position at about 6009 eV. This is further supported by a linear combination XANES fit of the edge region, a typical result is presented in Fig. 2.
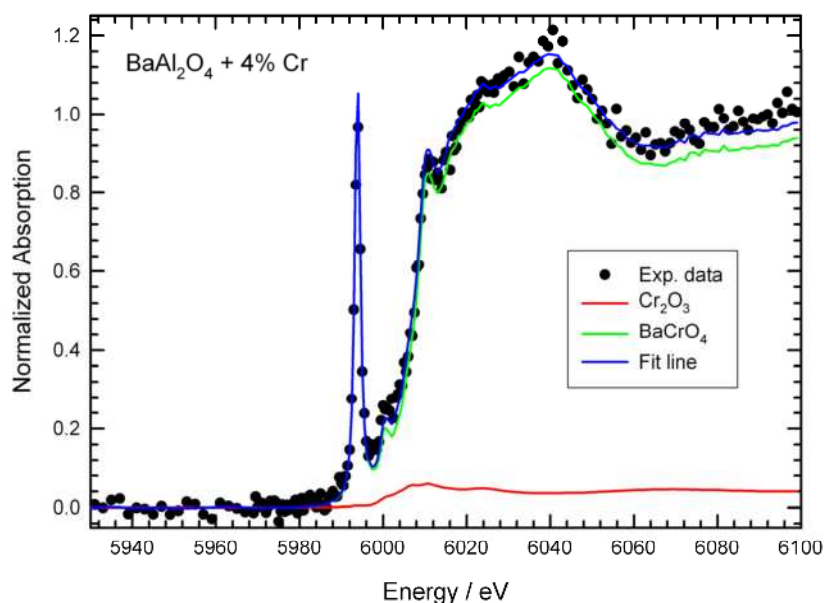
Fig. 2: Linear combination fit of the XANES spectrum from $BaAl_2O_4$ sample doped with 4 at.% Cr with XANES reference spectra from Cr_2O_3 and $BaCrO_4$. The best fit indicates that about 96% of the total Cr content is incorporated as Cr^{6+} in tetrahedral sites of the $BaCrO_4$ phase and only 4 % of the Cr content is incorporated as Cr^{3+} in the $BaAl_2O_4$.

$BaAl_2O_4$ obeys a hexagonal crystal structure, with two structurally inequivalent Ba^{2+}-sites and four different Al^{3+}-sites [6, 7]. While barium atoms are 9-fold coordinated with Ba-O distances in the range from 2.69-3.00 Å, aluminum atoms are 4-fold coordinated with Al-O distances in the range 1.71-1.83 Å. The present results thus suggest that only 4% of the Cr is incorporated in the $BaAl_2O_4$ phase, while the majority of the Cr participates in forming the impurity phase $BaCrO_4$. The refined unit-cell parameters of Cr-doped $BaAl_2O_4$ samples differ from those of pure $BaAl_2O_4$, which indicates that the structure of the material has changed due to the presence of the dopant. Additional EXAFS experiments are required in order to elucidate the short-range order structure around the Cr in more detail, allowing to understand and improve the luminescent properties of the material.

References
[1] C. Kim, I. Kwon, C. Park, Y. Hwang, H. Bae, B. Yu, C. Pyun, G. Hong. J. Alloys Compounds 311 (2000) 33.
[2] K. Fukuda, T. Iwata, T. Orito. J. Solid State Chem. 178 (2005) 3662.
[3] Y. Lin, Z. Zhang, Z. Tang, J. Zhang, Z. Zheng, X. Lu. Mater. Chem. Phys. 70 (2001) 156.
[4] M. Vrankić, PhD-thesis, University of Zagreb, Croatia (2014).
[5] D. Lützenkirchen-Hecht, R. Wagner, S. Szillat, A.K. Hüsecken, K. Istomin, U. Pietsch, R. Frahm. J. Synchrotron Rad. 21 (2014) 819.
[6] W. Hörkner, H.K. Müller-Buschbaum, Z. Anorg. Allg. Chem. 451 (1979) 40.
[7] S.-Y. Huang, R. von der Mühll, J. Ravez, J.P. Chaminade, P. Hagenmüller, M. Couzi, J. Solid State Chem. 109 (1994) 97.

Extended X-ray absorption fine structure (EXAFS) Investigation of aqueous salt solutions under high pressure

K. Julius[1], **C. Sternemann**[1], **M. Paulus**[1], **T. Büning**[1], **K. Esch**[1], **J. Schulze**[1], **P. Degen**[2], **R. Wagner**[3], **and M. Tolan**[1]

[1]Fakultät Physik / Delta, Technische Universität Dortmund, D-44221 Dortmund, Germany
[2]Fakultät Chemie, Technische Universität Dortmund, D-44221 Dortmund, Germany
[3]Fachbereich C Physik, Bergische Universität Wuppertal, Gaußstr. 20, 42097 Wuppertal

The properties of ion hydration structures under high hydrostatic pressure are essential to understand the stabilization or destabilization of proteins under solution. The investigation of the pressure dependent changes of the ionic hydration shell geometry and the structural impact that water (de)stabilizing agents like ions [1] have upon the bulk solvent medium under high hydrostatic pressure can give comprehensive insight to the non linearity in the pressure dependence of the protein-protein interaction potential [2]. We investigate the influence of high hydrostatic pressures up to 5kbar on the first hydration shells and the coordination numbers of the 0.1M salt solutions rubidiumchloride (RbCl) and yttriumchloride (YCl_3). In order to determine the local water network around Rb^+ and Y^{3+} we have used extended X-ray absorption fine structure (EXAFS) analysis. The EXAFS measurement has been performed at DELTA (BL8) in transmission geometry with a high pressure cell in vicinity of the Rb K-edge at 15200eV and the Y K-edge at 17080eV. Due to the use of conventional polycrystalline diamond windows for the high pressure cell numerous Bragg reflections caused glitches in the EXAFS spectra. By measuring spectra at different sample tilt and averaging over all spectra excluding the energy range where the glitches occurred their influence could be minimized. However, under these circumstances the obtainable k-range was limited. The EXAFS spectra at pressures from 50 to 5000bar of 0.1M RbCl solution and from 50 to 4000bar of 0.1M YCl_3 solution are presented in Fig(a-b). The k-weighted Fourier transform of $\chi(k)$ for both samples in r-space are shown in Fig (c-d) for each pressure. Within the limits of the experiment, the spectra show evidence that the first hydration shells around Rb^+ and Y^{3+} are not influenced by the pressure increase up to 5000bar while the macroscopic system shows a compression. The relative ion-oxygen distance (blue) and the relative water-water distance (red) in dependence of the pressure are shown for both salt solutions in Fig (e-f), additionally the relative water-water distance of pure water under pressure is displayed (black). Information about the structure beyond the first hydration shell could not be extracted from the data to this point. Currently, we perform MD-simulations of the 0.1M salt solutions under pressure from 50 to 5000bar to gain further insight on the structures of the first and second hydration shell and to compare to the experimental results. Moreover, we optimized the experimental setup using nanocrystalline diamond windows to avoid glitches due to Bragg reflections. It is expected to obtain a significantly wider k-range with this setup and thus more information about the second hydration shell.

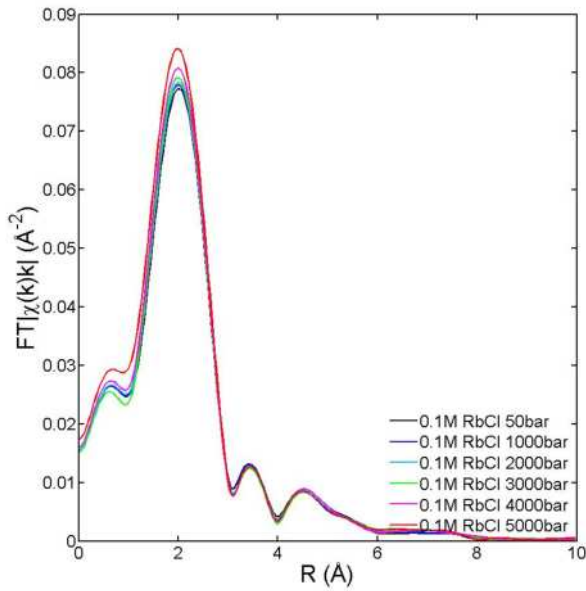## Literatur

[1] Y. Marcus, Ionic radii in aqueous solutions. Chem. Rev. **88**,1475-1498 (1988)

[2] M.A. Schroer, J. Markgraf, D.C.F. Wieland, Ch.J. Sahle, J. Möller, M. Paulus, M. Tolan, and R. Winter, Physical Review Letters **106**, 178102 (2011)
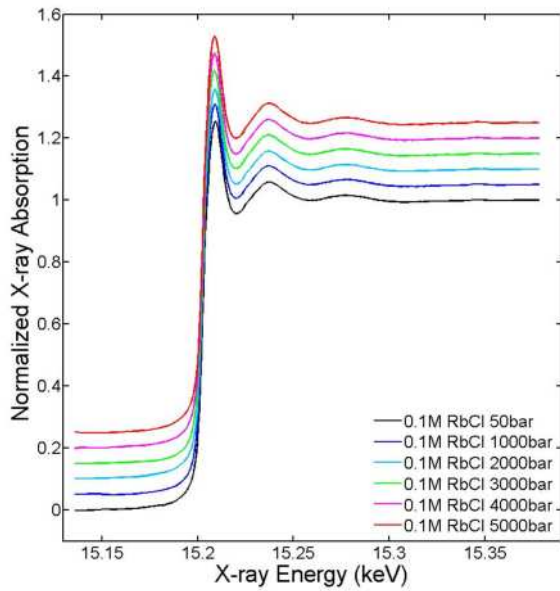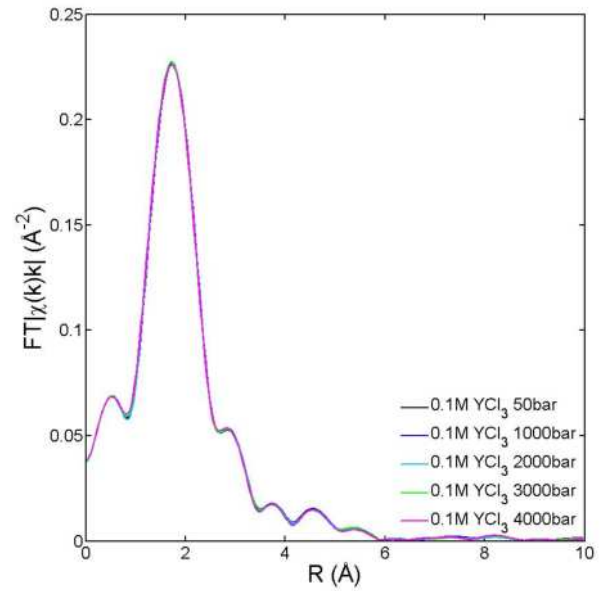
(a) normalized X-ray absorption
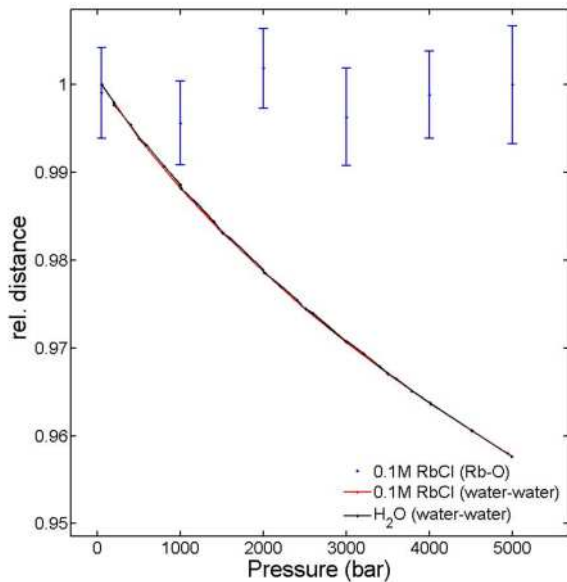of 0.1M RbCl solution
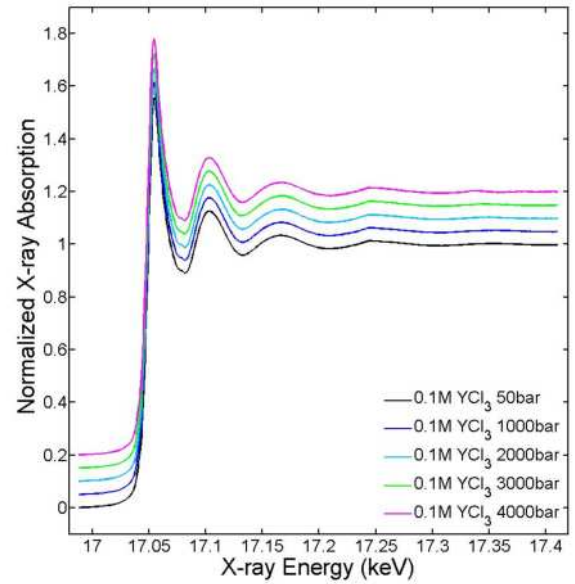
(b) normalized X-ray absorption
of 0.1M YCl$_3$ solution
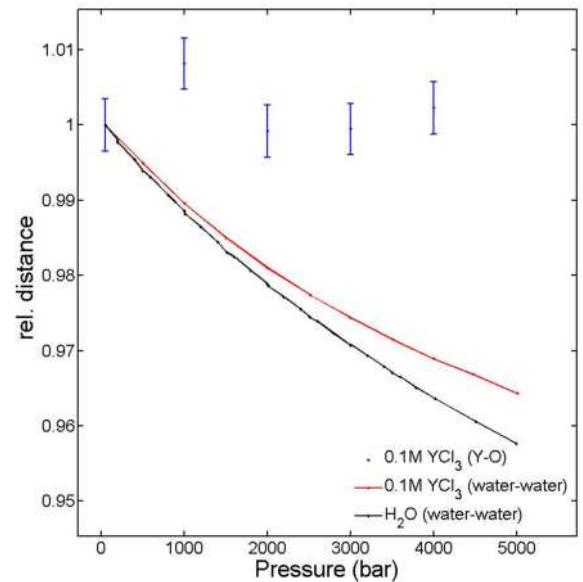
(c) Fourier transform in r-space
FT($\chi(k) \cdot k$) of 0.1M RbCl

(d) Fourier transform in r-space
FT($\chi(k) \cdot k$) of 0.1M YCl$_3$

(e) Compression 1st hydration shell of 0.1M RbCl

(f) Compression 1st hydration shell of 0.1M YCl$_3$

# Ex-situ EXAFS investigations of steel deoxidation processes

D. Lützenkirchen-Hecht[a], D. Wulff[b], R. Wagner[a], U. Holländer[b]

a) Fachbereich C - Physik, Bergische Universität Wuppertal, Gaußstr. 20, 42097 Wuppertal, Germany.
b) Institut für Werkstoffkunde (Materials Science), Leibniz Universität Hannover, An der Universität 2, 30823 Garbsen, Germany.

Many metals are protected against corrosion under ambient conditions by ultrathin oxide/hydroxide films with a thickness of typically some few nm - among those the technologically important transition metals Fe, Ni, Cr and their alloys [1]. The formation of these so called passive layers stabilizes the reactive metal surface against corrosion. Due to the enormous technological importance of passivity, this has led to intensive studies of the structure and chemistry of passive layers and the closely related protective properties. While the passive layers are important for the protection of the metal, their presence may hinder or even prevent fluxless brazing processes, i.e. the oxide layers on steels (Fe-Cr-Ni alloys) need to be removed prior to the brazing in the furnace at temperatures in the range between 900 and 1150 °C typically [2, 3]. However, especially the reactive metals (Cr, Fe) are further oxidized at elevated temperatures by traces of oxygen or water in the protective atmosphere of a brazing furnace (typically nitrogen, argon and/or hydrogen) [4, 5], which is counterproductive in terms of the brazeability.

In a previous study, we have investigated the surfaces of stainless steel (EU alloy grade 1.4301 X5CrNi18-10) after different heat treatments by surface sensitive, reflection mode EXAFS spectroscopy [6]. These ex-situ EXAFS results show that the iron in the steel can only be reduced to a metallic state if monosilane (SiH_4) was used as a reducing additive in the conveyor belt furnace using a temperature of 900 °C and N_2 and/or Ar as carrier gases [6]. Lower temperatures and process atmospheres without silane (e.g. using H_2 instead) always result in strongly oxidized steel surfaces. Here we report on the results obtained at the Cr K-edge after different de-oxidation treatments in a conveyor belt furnace in the temperature range between 600°C and 900°C. The X-ray experiments were performed at beamline BL10 at the DELTA storage ring [7], employing a Si(111) channel-cut monochromator, and N_2- and Ar-filled ionization chambers as detectors for the incident and the reflected intensities.
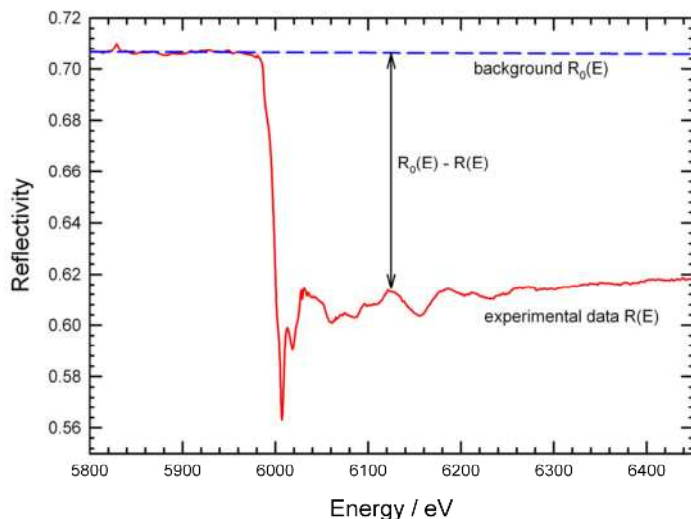
Fig. 1:
Reflection mode EXAFS spectrum of a steel sample at the Cr K-edge for an incidence angle $\Theta = 0.25°$. The sample was treated at 900°C in an Ar + 20 ppm SiH_4-mixture for 25 min. For the data evaluation, the pre-edge background $R_0(E)$ was extrapolated into the post-edge region of the spectrum and subtracted from the data. The difference $R_0(E)-R(E)$ was used as a measure for the absorption.

As can be seen in Fig. 1, reflection mode EXAFS data of reasonable quality may be obtained at BL10, having in mind that the Cr-concentration in the steel material is only about 18 wt.%. For the further data analysis, the difference $R_0(E)-R(E)$ was used as a measure for the absorption, and the extracted data for the different treatments are compared to those of reference compounds in Fig. 2.
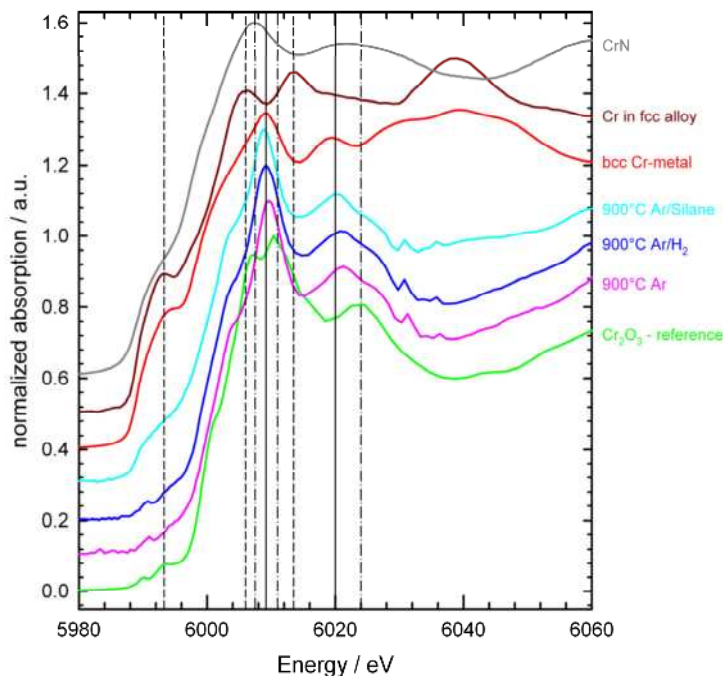
Fig. 2:
Comparison of the Cr K-edge X-ray absorption data of several heat-treated steel samples with those of several Cr reference compounds as indicated. The vertical lines represent characteristic features for metallic body-centered cubic Cr (full lines), face centered cubic Cr (short-dashed), and Cr_2O_3 (dash-dotted) reference compounds.

Only in the spectrum measured for the sample with a silane addition during the thermal treatment, a strong edge feature similar to that of metallic chromium could be detected at about 5993.5 eV. The metallic Cr in this sample seems to be present in a body-centered cubic structure, because the face-centered cubic Cr reveals substantially different XANES features, with a double-peaked structure above the edge at about 6006 and 6013 eV, while the bcc-phase only gives a single dominant peak at about 6009 eV and an absorption minimum at 6013 eV. All other spectra strongly resemble that of Cr_2O_3 especially in the pre-edge region, where only small absorption values can be detected. In addition, the features well above the edge, i.e. a broad absorption maximum at about 6025 eV and a rather low absorption at about 6036 eV agree with Cr_2O_3 as well. For the future, in-situ de-oxidation experiments are planned.

References
[1] H.-H. Strehblow. Passivity of Metals. In: Advances in Electrochemical Sciences and Engineering. R. Alkire, D.M. Kolb (Eds.). Weinheim: Wiley-VCh (2003) 271.
[2] F.-W. Bach, K. Möhwald, U. Holländer, C. Roxlau. SCIB - Self-Cleaning Inert-Gas Brazing - Ein neues Verfahren zum flussmittelfreien Hartlöten korrosionsbeständiger Konstruktionswerkstoffe. 8. Int. Kolloq. Hart- und Hochtemperaturlöten und Diffusionsschweißen, Düsseldorf: DVS-Verlag, DVS-Ber. 243 (2007) 235.
[3] F.-W. Bach, K. Möhwald, U. Holländer. Key Eng. Mat. 438 (2010) 73.
[4] J.-M. Abels, H.-H. Strehblow. Corrosion Science 39 (1997) 115.
[5] E. Clauberg, C. Uebing, H.J. Grabke. Surface Science 433–435 (1999) 617.
[6] D. Lützenkirchen-Hecht, D. Wulff, R. Wagner, R. Frahm, U. Holländer, H.J. Maier. J. Mater. Sci. 49 (2014) 5454.
[7] D. Lützenkirchen-Hecht, R. Wagner, S. Szillat, A. K. Hüsecken, K. Istomin, U. Pietsch, R. Frahm. J. Synchrotron Rad. 21 (2014) 819.

An Exploration of Cobalt Compounds and The Effect of Scan Speed on Data Quality: A Student Project

Jeremy Munsell[1], Ralph Wagner[2], and Dirk Lützenkirchen-Hecht[2]

[1]Department of Computer Science, Engineering, and Physics, University of Michigan-Flint,

303 E. Kearsley Street, Flint, Mi 48507, USA

[2]Fachbereich C-Physik, Bergische Universität Wuppertal,

Gauβstr. 20, 42097 Wuppertal, Germany

E-mail: jeremymu@umflint.edu.

1 Introduction

Cobalt is an intriguing element with many interesting chemical and physical properties. Its resistance to corrosion and stress and the retention of its ferromagnetism at temperatures above $1000°$C make it an attractive material to industry. Reactor made Cobalt-60 is used as a source of gamma radiation for the treatment of cancer. Cobalt's most common oxidation state is +2 or +3. Resultingly, it is often found compounded with halogens, hydroxides, or oxygen.

2 Outline

With the intention of gaining insight into the sensitivity of data quality to the scan parameter of integration time, two EXAFS (Extended X-Ray Absorption Fine Structure) scans were performed on standard Co metal foil, allowing the scan speed to vary between them. Secondarily, absorption spectra of cobalt hydroxide, $Co(OH)_2$, and Cobalt Oxide, Co_3O_4, were collected for the purposes of determining the structure of each compound.

3 Experimental

The scans of the cobalt foil were conducted in the vicinity of the Co K-edge (7.709 keV) over an energy range of about 200 eV pre-edge and 800 eV post-edge. The first scan (Scan 62) initiated at an energy of 7.499 keV with an integration time of 1s and was increased to 2s at an energy of 7.729 keV, to 3s at an energy of 7.831 keV, and finally to 4s at an energy of 8.332 keV. The scan terminated at an energy of 8.729 keV. In the second scan (Scan 64), the integration time was held constant at 0.1s over the same energy range.

The cobalt hydroxide (Scan 65, $Co(OH)_2$) and cobalt oxide (Scan 77, Co_3O_4) samples were prepared by first homogenizing powders of each substance by mortar and pestle. Subsequently, the homogenized powder was affixed to any of several small pieces of scotch tape, then stuck between two larger pieces of tape. EXAFS scans of each substance were conducted over the same approximate energy range as for the foil.

4 Analysis/Conclusions

All spectra were imported into the IFEFFIT program ATHENA, and each was normalized, energy calibrated, and pre-edge background subtracted. The normal scanning procedure (Scan 62) was compared to the quick scanning procedure (Scan 64) by plotting the first derivative

1

spectra $(d\mu/dE)$ together against incident photon energy. The plot showed that the normal scan and the quick scan were quite convergent around the edge energy, which is the first energy maximum on the derivative spectrum, of 7709 eV. At the higher end of the energy domain, where the features of the μ began to flatten out and the signal to noise ratio was decreased, the high frequency noise was quite apparent in the quick scan. However, as frames a) and d) of figure 1 show, the features and quality of μ v.s. E and χ v.s. k were unaffected. Where ultra-high quality data is not required, the quicker scan with integration time of 0.1s is a time efficient alternative to the normal scanning method with reasonably good data quality.
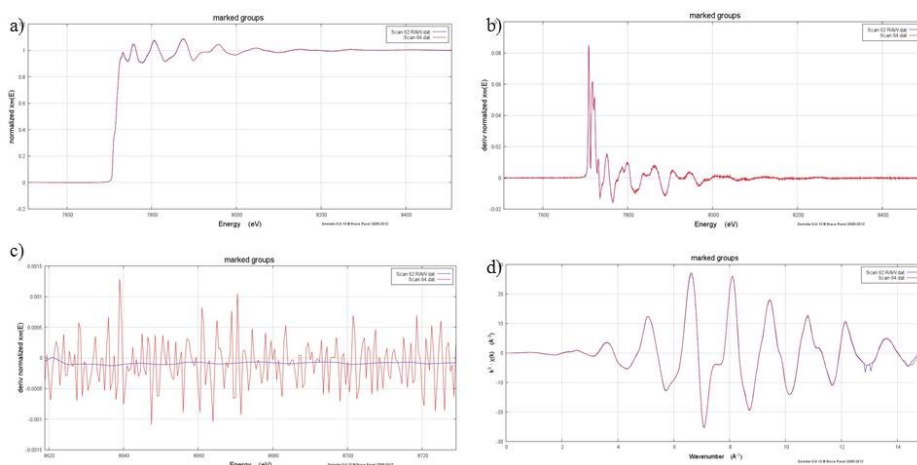

Figure 1: **a)** Plots of μ v.s. E for scans 62 and 64, **b** Plots of derivative spectra $\left(\frac{d\mu}{dE}\right)$ for scans 62 and 64, **c)** plots of derivative spectrum for higher energy scan 62 and 64, and **d)** and χ v.s. k for both scans

Cobalt hydroxide (Scan 65, $Co(OH)_2$) is a polymorphic material existing as either the α polymorph with a *cadmium iodide* structure, or as the β polymorph with a *brucite* structure. The spectra were fit in the IFEFFIT program ARTEMIS, with crystallographic data generated by ATOMS. By fitting the experimentally obtained spectrum with both candidate structures and evaluating the quality of the fit, a good indication of the correct structure was given.

As frame a) of figure 2 shows, the fit of the cobalt hydroxide sample with the *cadmium iodide* structure is hardly compelling. Though the peaks were in the correct energy position, they were much wider than experiment. As Frame a) of figure 3 shows, the fit of the experiment with the *brucite* structural parameters was qualitatively much more convincing. Both peaks were in the right positions in energy space, and seemingly converged with experiment. Table 1 shows the statistical results of the fit, which also seem to indicate that the fit of the experiment with the *brucite* structure was far superior to that of the *cadmium iodide* structure. While the superiority of the fit using the *brucite* structure is by no means conclusive, it is a strong indication that the cobalt hydroxide sample was of the β polymorph.
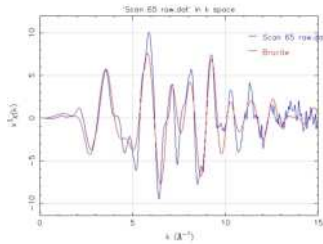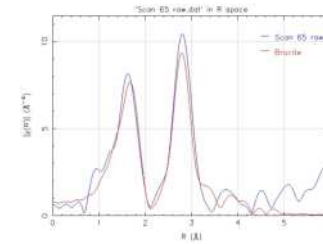
2
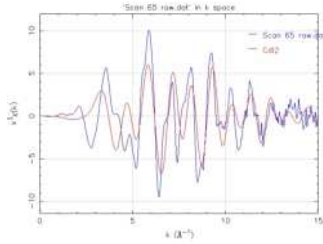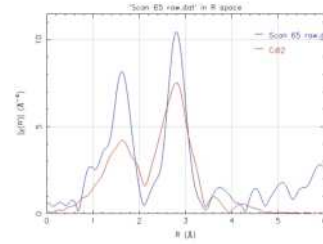
(a) $\chi(k)$ v.s. k plot

(b) FT $\chi(R)$ v.s. R plot

Figure 2: Plots for the fit with the Cadmium Iodide structure

(a) $\chi(k)$ v.s. k plot

(b) FT $\chi(R)$ v.s. R plot

Figure 3: Plots for the fit with the Brucite structure

Table 1: Parameters of the Fit

Unit Cell	N_{idp}	N_{var}	χ^2	$\tilde{\chi}^2$	R
CdI_2	37	4	323826	9760	0.3869
Brucite	37	4	44937	1354	0.05628

The cobalt oxide (Scan 77, Co_3O_4) was suspected to have the normal spinel structure in analogy with *magnetite* (Fe_3O_4). Crystallographic data for magnetite were used, changing the lattice parameters accordingly. The unit cell of cobalt oxide consists of 8 tetrahedrally coordinated Co^{2+} ions, 16 octahedrally coordinated Co^{3+} ions, and 32 O^{2-} ions, making for quite a complicated structure. The fit(s) for the compound used two sets of scattering paths, one with Co^{2+} designated as the absorber, and another with Co^{3+} ions as the absorber. From which, the first coordination shell was fit with Co-O scattering paths.

Table 2: Co-O Scattering Paths Included

Path Degeneracy	Path	Path Length
4	$Co^{2+} \rightarrow O \rightarrow Co^{2+}$	1.816 Å
6	$Co^{3+} \rightarrow O \rightarrow Co^{3+}$	1.983 Å

The R-factor of 0.00668 is a strong indication of the good quality of the fit of the first coordination shell with Co-O scattering. The second shell was fit with Co-Co scattering

Table 3: Co-Co Scattering Paths Included

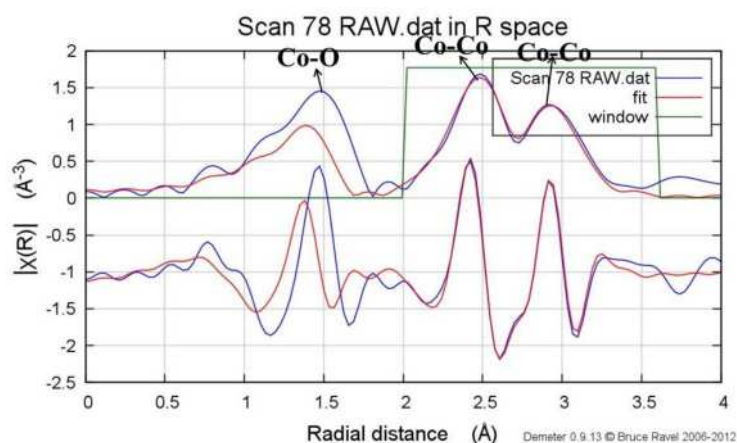| Path Degeneracy	Path	Path Length
12	$Co^{2+} \rightarrow Co^{3+} \rightarrow Co^{2+}$	3.351 Å
6	$Co^{3+} \rightarrow Co^{2+} \rightarrow Co^{3+}$	2.857 Å

3

Figure 4: The results of the fit of both coordination shells of Co_3O_4

The R-Factor of 0.042 is indicative that the fit of the Co-Co peaks are also of reasonably good quality.

The combined fit of both coordination shells using Co-O scattering paths and Co-Co scattering paths is certainly not perfect as qualitatively evidenced by the lack of agreement between experiment and the fit for the Co-O peak. In light of the low R-Factor value of 0.02 this fit can be considered to be acceptable, and strongly suggests that the proposed lattice structure is the correct one.

4

Sulfur K-edge transmission mode XANES measurements of the solar cell absorber material Cu_2ZnSnS_4

Stefan Balk, Justus Just, Ralph Wagner, Dirk Lützenkirchen-Hecht, and Ronald Frahm

Fachbereich C - Physik, Bergische Universität Wuppertal,
Gaußstr. 20, 42097 Wuppertal, Germany.

In recent years the demand for sources of renewable energy have increased rapidly, which includes energy obtained from solar cells. Solar cells can be composed of a variety of different elements, for example silicon or the aforementioned Cu_2ZnSnS_4 (CZTS). While the thick (~300 µm) silicon based cells are widespread and have a rather energy intensive production procedure, thin film solar cells (2 µm) can be a promising alternative. CZTS is a material that can be used as an absorber layer in thin film solar cells. Due to the mix of different elements and the very narrow existence region of single phase CZTS in the phase diagram, secondary phases can very often be exhibited after non-equilibrium processes during production, such as physical vapour deposition [1]. The most prominent of the secondary phases is zinc sulphide, which has a bigger band gap than the CZTS and thus reduces its efficiency as solar-cell material [2]. Due to their influence on the performance, it is of utmost interest to quantify the secondary phases within the material qualitatively and quantitatively.

The method of choice for this quantification is the investigation of the sulfur K-edge X-ray absorption near edge structure. It can yield important element specific information about the central sulfur atom as well as the local crystal structure. Sulfur absorption measurements are especially preferable because the K-edges of the cations (copper, zinc, tin) do not exhibit such a strong dependence on the nature of the secondary phases due to the interaction between sulfur and the cationic species. Furthermore the K-edge of sulfur at 2472 eV lies well within the energy range of the InSb(111) double crystal monochromator of BL8.

Recently an ionization chamber has been installed, connected to the experiment via an ultra thin (50 µm) beryllium port window. This instrumental upgrade now allows samples to be measured in transmission in addition to the already existing fluorescence detection either by a passivated implanted planar silicon (PIPS) diode or an energy dispersive detector utilizing a silicon drift diode with a multichannel analyser.

So far the sample series consisted only of single phase CZTS and ZnS. CZTS thin films have been produced by PVD at the Helmholtz-Zentrum Berlin (HZB). To be able to measure transmission and fluorescence signals simultaneously the samples were scraped off the substrate, ground into a powder and then spread evenly onto a highly transmissive adhesive tape. The ZnS powder has been prepared similarly. Presently new samples are expected to be compared to the already analysed reference materials.

The idea is then to do linear combination fitting of the references to the samples to quantify the amount of the different secondary phases. It has been shown previously, that ZnS is the predominant binary phase with a share of more the 98% [3]. Fig. 1 shows the S K-edge XANES spectra of the two reference samples, the ZnS in red and the CZTS in black. Their XANES differ substantially from each other with CZTS exhibiting a strong pre-edge peak and an edge-shift of about 1.1 eV as a result of the different density of states [3]. The strong peak at about 2482 eV is due to the absorption of the adhesive tape. Previous work have shown that the preferred fitting range is between 2466 eV and 2477 eV. The effect of the combination can be seen exemplary in Fig. 2. Depending on the ratio of ZnS to single phase CZTS, the pre edge peak becomes smaller and the three peaks between 2472 eV and 2477 eV rise and vice versa [3].
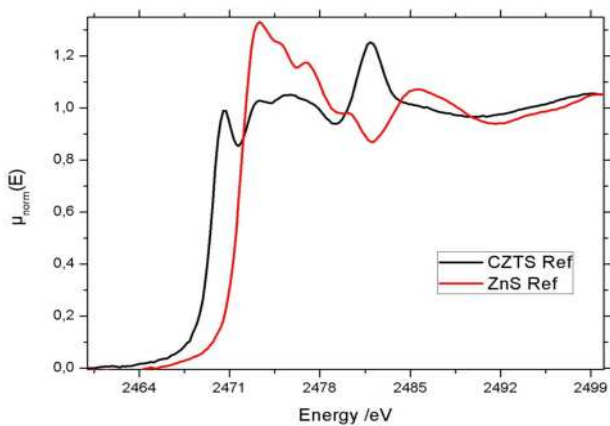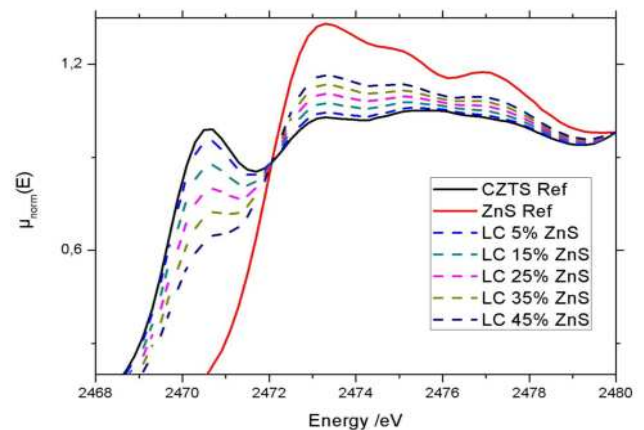

Figure 1: Reference spectra of CZTS and ZnS

Fig. 2: Linear combinations of the two spectra

References

[1]   A. Nagoya, R. Asahi, R. Wahl, G. Kresse: *Defect formation and phase stability of CZTS photovoltaic Material,* Phys. Rev. B **81**, 113202 (2010)

[2]   B. Schubert, B. Marsen, S. Cinque, T. Unold, R. Klenk, S. Schorr, H. Schock: *CZTS thin film solar cells by fast coevaporation,* Prog. Photovoltaics **19**, 93 (2011)

[3]   J. Just, D. Lützenkirchen-Hecht, R. Frahm, S. Schorr, T. Unold: *Determination of secondary Phases in kesterite CZTS thin films by x-ray absorption near edge structure analysis,* Appl. Phys. Lett. **99**, 262105 (2011)

Notes

<u>Notes</u>